UNIVERSITY OF TROMSØ UIT

FACULTY OF SCIENCE AND TECHNOLOGY
DEPARTMENT OF PHYSICS AND TECHNOLOGY

Statistical analysis of fluctuations in the Alcator C-Mod scrape-off layer

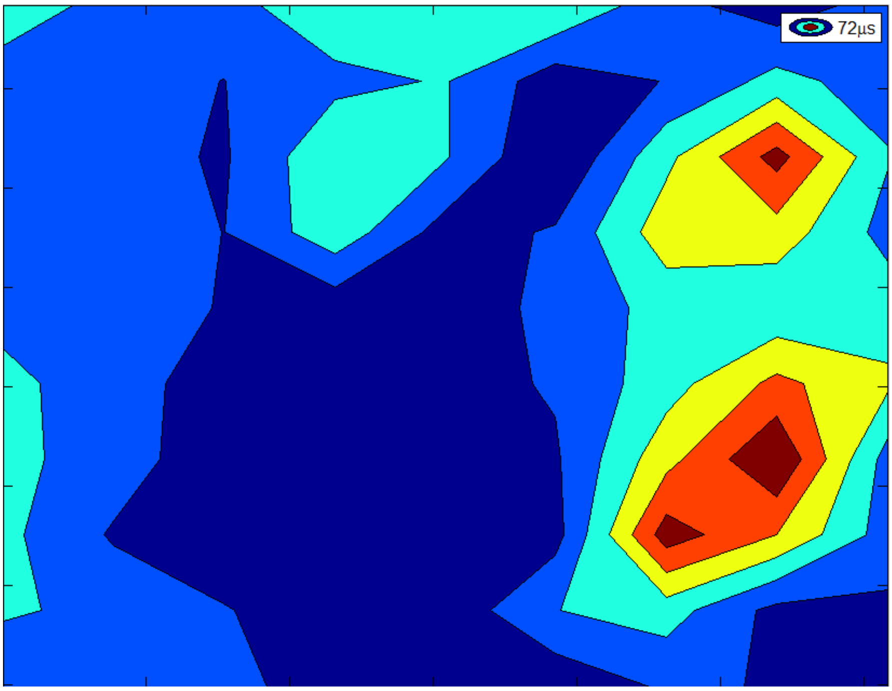

Sindre Markus Fritzner

FYS-3900 Master’s Thesis in Physics

June 2013

Abstract

Experimental data from Alcator C-Mod have been used to analyze large density events occurring at the edge of fusion reactors. The data acquisition methods used are gas puff imaging and Langmuir probes. The data consist of long time series sampled at high frequency, excellent for statistical analysis. Large density events have been analyzed where blobs are found to be consistent with high skewness and kurtosis. The skewness and kurtosis are found to increase with both radius and decreasing line-averaged density. For small kurtosis and skewness the distributions are well fitted by a gamma distribution, while for higher values a distribution suggested by Sattin is the better fit [81]. The conditionally averaged waveforms in the scrape-off layer have a sharp exponential rise with slower exponential decay. The waveform is independent of line-averaged density, major radius and amplitude. In addition the waiting times between events are found to be exponentially distributed, consistent with independent events in a Poisson process. Self-similarity and long range correlations have been analyzed by using the Hurst exponent. The Hurst exponents have been estimated by four methods, power specter, rescaled range, structure functions and wavelets. The Hurst exponents are found to decrease with major radius, where only weak long range correlations are found in the blob dominated area. The average blob velocities are found to be 1-3km/s both in radial and vertical direction, consistent with a mixture of kink and ballooning magnetohydrodynamic instabilities. The blobs have a poloidal size of 1-2cm, independent of radial position and line averaged density. The stochastic model proposed by Garcia is found to be a good fit for signals close to the separatrix, where the blobs are created [28]. The model can not be used to explain long range correlations.

Acknowledgments

First of all I would like to thank my supervisor Odd Erik Garcia. Odd Erik is like a living encyclopedia, whatever the question he has the answer. He has provided me with invaluable insight in programming, statistics, plasma physics and fusion power. His large enthusiasm for the project provided me with priceless motivation. I would also like to thank the Alcator C-mod team at Massachusetts Institute of Technology for providing excellent experimental fusion time series.

I would like to thank my girlfriend for always keeping my mood up and helping me unwind when I came home from school. In addition I would like to thank all my family and friends for always being there for me and supporting me.

Contents

Chapter 1

Introduction

The need for energy has never been greater than today, at the same time the world may face a global warming crisis. Several different renewable energy resources as wind, solar and tidal power exist for generating clean electrical power. These renewble energy resources might not produce enough energy to cover the amount received from coal, oil and gas today. Nuclear power like fission and fusion on the other hand is capable of covering the energy demand. Nuclear power by fission has large safety issues and is therefore not an option in many countries. The motivation for this thesis is nuclear power by fusion. Fusion power is not a new science, it is the method used by stars for generating power and has been used by nature since the start of the universe. Here on earth fusion physicist have been trying to generate fusion power since the 1950s [70]. The future of fusion power lies on the building of the International Thermonuclear Experimental Reactor (ITER). ITER is an international fusion reactor project where the countries involved covers half of the worlds population. Experiments on ITER will hopefully be a first step towards a commercial fusion reactor.

Fusion power provides sustainable energy with no direct release of greenhouse gases. In the ideal case 0.14 tonne deuterium can generate the same amount of electrical energy as 10^6 tonne oil [25]. Deuterium can be extracted from seawater, so in practice there are unlimited resources on earth. So why do we not have unlimited power? Fusion reactions as we know it can only occur at extreme temperaturesf in a confined space. The particles are confined magnetically by the use of strong currents. The magnetic confinement is one of the biggest challenges in fusion research because perpendicular velocity components carry the particles between magnetic field lines and out of the plasma. Experiments in fusion research have shown that the boundary regions are largely dominated by high amplitude bursts transporting particles and heat away from the core where the fusion reactions take place. Several analytical solutions to the burst formation and propagations have been done in earlier studies [17, 19, 30–32, 47, 48], and will be repeated in a later section. The classical plasma physics describe the transport of particles across the magnetic field by diffusion, this is done in many textbooks such as Chen [15]. Close to the wall this is not the case. Here the transport is dominated by propagating convective structures known as blobs [18, 65].

Statistical analysis will be done on time series collected close to the outer walls in a fusion device. The analysis will focus on the propagating structures to see how they behave statistically. This will be analyzed by distributions and persistence. One of the key properties of this thesis is the persistence, since a persistent signal can be described by self-organized criticality [5]. This is a theory where the fluctuations builds up towards a critical state where large events may occur. The signals will be assumed to be described as fractional Gaussian noises as explained by Mandelbrot and Van Ness 1968 [58]. From this assumption it is possible to calculate the long range correlations with the rescaled range analysis as first done by Hurst in 1951 [2]. In 1969 Mandelbrot and Wallis published a series of three papers where they did computer simulations with the rescaled range analysis on fractional data [59]. Later much work have been done with the rescaled range analysis both theoretically and experimentally. A more thorough investigation of the rescaled range analysis was done by Anis and Lloyd in 1976 [2]. The rescaled range analysis has been used in a wide range of sciences spanning from stock exchange to climate [69, 77]. Now a variety of methods are used to find long range correlations, one of the most versatile methods is the wavelet method [23], other methods can be found in Rea [72].

In the late 90's long range correlation analysis were introduced in plasma fusion on the large amplitude events close to the wall to see if these may be described by self-organized criticality. One of the first pioneers in long range correlation calculations in fusion tokamaks was Carreras [12–14]. He found evidence of long range correlations on short time series. This work will do an extensive investigation of long range correlations on long time series acquired from the Alcator C-Mod tokamak located at the plasma science and fusion center, Massachusetts Institute of Technology (MIT). The data consist of measurements taken both with Langmuir probes [34, 52] and gas puff imaging [16, 34, 60]. In addition a stochastic model explaining blob dominated signal will be analyzed and compared with experimental measurements [28].

1.1 Motivation

A large part of the particle and heat transport across the magnetic field lines are caused by large density plasma blobs. These blobs cause increased interaction between material walls and plasma leading to loss of heat, erosion of material walls and decreased plasma confinement [17]. For further devices, such as ITER, it is important to understand these blobs since they control the particle and heat flux out of the plasma. In this work the statistical and physical mechanisms of high density blobs will be studied. In recent years much research have been done on describing these blobs, but the experimental measurements have been short and the results inconclusive. To verify statistical properties such as distributions and long range correlations very long time series are needed.

Recently a stochastic model has been proposed as a possibly explanation for the blob dominated density signals [28]. This model has started a new era for understanding the statistical mechanisms behind the blobs. Thus it is important to match this model with experimental measurements.

The goal of this thesis is to analyze experimental measurements from Alcator C-mod both with Langmuir probes and GPI measurements. The results will elucidate how the statistical properties of the measurements change as a function of spatial position, line-averaged density and blob properties. The statistical analysis can be used to clarify the underlying mechanisms of turbulence and instabilities causing the blobs. This can help set the parameters for future experiments and devices.

1.2 Structure of thesis

This thesis is divided into two parts. The first part will describe the theoretical background. The mathematical description for blobs will be reviewed together with an introduction to fusion power and reactor design. In addition all the statistical methods will be explained and tested on computer generated signals.

In the second part of the thesis the results will be described and discussed. There are three main topics here, gas puff imaging measurements, probe measurements and results of the Stochastic model. The gas puff imaging data will be analyzed with focus on long range correlations. The probe measurements and stochastic model will mostly be used for verification of the results found for the gas puff imaging. At the end of the thesis an appendix is found containing commonly used abbreviations, derivations and matlab code.

Part I

Theoretical background

Chapter 2

Plasma fusion

This chapter will elaborate some general knowledge about fusion and the main problems involved. The main properties of confinement will be reviewed and important terms will be introduced for later references. In the last part of the chapter the setup of the Alcator C-Mod tokamak will be presented together with two data acquisition methods, gas puff imaging and Langmuir probe. The first part of this chapter will follow the book of Freidberg closely [25].

2.1 Nuclear power

There are two main branches of nuclear power, fission and fusion. Fission is a physical reaction where one heavy atom is divided into two lighter atoms. Fusion is the opposite reaction where two light atoms is fused into one heavier atom. In a fusion reaction the resulting particle has a smaller mass than the mass of the sum of the reactants. Following Newtons famous energy equation $E = mc^2$ energy must be released in a fusion reaction [70]. The amount of energy released has to do with the average binding energy, more information can be found in Freidberg [25]. In a fission reaction the opposite result is seen where the resulting particle is heavier than the reactants, therefore the heavy particle must be split up into smaller particles to generate energy. The breakpoint is due to the average binding energy which has a maximum at iron. Particles lighter than iron can be used in fusion and particles heavier than iron can be used in fission [25].

2.2 Thermonuclear fusion

In order for fusion to occur the particles need to overcome the long range coulomb force keeping the particles apart. The coulomb force acts as to repel particles of equal charge. To breach the coulomb barrier the particles need high kinetic energy achieved by extreme temperatures, a topic of much research [25]. In figure 2.1 the reaction rates for three fusion reactions are plotted as a function of temperature. See that the figure shows a reaction rate with a sharp increase up to about a billion kelvin. Which is the order of temperature needed to keep the plasma burning [25].

2.2.1 Lawson criterium

In an ideal situation the temperature/pressure needed to keep a plasma burning is defined by the Lawson criterium. The Lawson criterium can be derived from a 0-D power balance containing the heat gain and loss in the reactor. In a fusion reactor the heat gain is that of the reactions. Note that not all energetic particles can be used to heat the plasma. Neutral particles are not confined by the magnetic field, thus they will travel out of the plasma. In a fusion reactor heat is in the ideal case lost by radiation, the most significant is the Bremsstrahlung radiation. Bremsstrahlung radiation is caused by acceleration of particles gained from Coulomb collisions. A last term governing the 0-D heat balance in a fusion reactor is the heat flux due to plasma effects, such as turbulence and collisions [25].

2.3 Fusion reactions

In this section the three main fusion research reactions are presented. Present research focus on the reaction which occurs at the lowest temperatures, while in the future it might be possible to use a more sustainable and non radioactive reaction. The temperature dependence of the reaction rate was given in figure 2.1. The following and more information about fusion reactions can be found in Freidberg [25].

Deuterium-Helium reaction

This reaction consists of fusion between a deuterium (H^2) and a helium-3 (He^3) nucleus. The powers represent the number of nucleons in the core. The reaction is given by,

$$\mathrm{H}^2 + \mathrm{He}^3 \rightarrow \mathrm{He}^4 + \mathrm{H}^1 + 18.3\,\mathrm{MeV}. \tag{2.1}$$

This reaction has a high energy output 3.66 MeV per nucleon, and all the resulting particles are charged particles, thus easily controlled. Present fusion research does not use this kind of reaction because He^3 is not natural on earth and high temperatures is required, see figure 2.1.

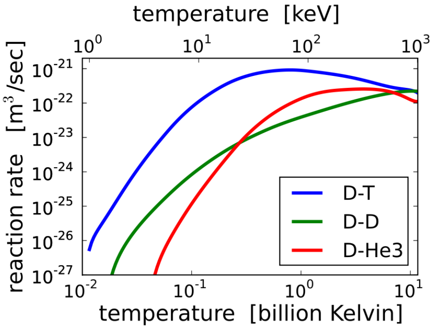

Figure 2.1 – This figure describes the reaction rate as a function of temperature for three fusion reactions. Can see that the D-T reaction rate is larger for lower temperatures than the other reactions which makes it favorable. The figure is made by Dstrozzi [20], similar figures can be found in most fusion textbooks i.e. Freidberg [25]. In the figure D stands for deuterium, T tritium and He is helium.

Deuterium - Deuterium reaction

The deuterium - deuterium (D-D) reaction can result in two processes with approximately equal probability of occurring,

$$\begin{aligned} \mathrm{H}^2 + \mathrm{H}^2 &\rightarrow \mathrm{He}^3 + n + 3.27\,\mathrm{MeV} \\ \mathrm{H}^2 + \mathrm{H}^2 &\rightarrow \mathrm{H}^3 + H^1 + 4.03\,\mathrm{MeV} \end{aligned} \tag{2.2}$$

These reactions create less energy than the last reaction with only 0.82 and 1.01 MeV per nucleon. It is believed that this method are the far future of fusion due to the great availability of deuterium, 33 milligrams per liter seawater. Today the high temperatures needed to initiate the D-D reaction makes it unfavorable for energy generation. The Alcator C-Mod which is a pure research device use D-D reactions.

Deuterium - Tritium reaction

The deuterium - tritium (H^3) reaction (D-T) is the reaction where most research is done. The reaction is favorable due to high reaction rate at lower temperatures, see figure 2.1. ITER will be using this type of reaction. The reaction can be written as,

$$\mathrm{H}^2 + \mathrm{H}^3 \rightarrow \mathrm{He}^4 + \mathrm{n} + 17.6\,\mathrm{MeV}. \tag{2.3}$$

The reaction results in an He^4 particle which is a charged particle and will stay in the plasma, the energy from this particle (3.5 MeV) will be used to heat the plasma. The neutron will not be trapped and will travel out of the plasma, the energy (14.1 MeV) can be extracted and used for generating electrical energy.

The main problem with D-T reaction is tritium. Firstly tritium is radioactive with a half life of 12.26 years, in addition, tritium is not found naturally on earth. Lithium can be used to breed tritium in the fusion device. This is done by a lithium blanket around plasma, the reactions are,

$$\begin{aligned} \mathrm{Li}^6 + n &\rightarrow \mathrm{He}^4 + \mathrm{H}^3 + 4.8\,\mathrm{MeV}, \\ \mathrm{Li}^7 + n &\rightarrow \mathrm{He}^4 + \mathrm{H}^3 + \mathrm{n} - 2.5\,\mathrm{MeV}. \end{aligned} \tag{2.4}$$

In a fusion device it is the first reaction which dominates, this is fortunate because this reaction also release energy. Both reactions use neutrons which is produced by the fusion reaction in the first place. Note that not all neutrons generated by the fusion reaction can be used to generate tritium, some are lost and some moves too fast or too slow. Thus much research is being done on accelerating/deaccelerating neutrons in addition to external neutron sources [25].

2.4 Magnetic confinement

The problem with confining plasma is the material walls. A solid surface interacting with a plasma is always an escape route for the particles. Charged particles will interact with the solid walls and stick to them. After a while the particles will recombine at the walls and be released into the plasma again as neutrals, this is called plasma recycling. When the fast and hot particles collide with the material walls erosion occur introducing impurities in the plasma [86].

The particle-wall interaction can be minimized by magnetic confinement. The principle behind magnetic confinement can be visualized in the single particle picture. On a single particle the effective force is the Lorentz force, the equation of motion can be written as [15],

$$m\frac{d\mathbf{u}}{dt} = q\left(\mathbf{E} + \mathbf{u} \times \mathbf{B}\right). \tag{2.5}$$

Where m is the particle mass, q is the elementary charge, u is velocity, E is the electric field and B is the magnetic field. For simplicity stationary electric and magnetic fields are assumed, the electric field is located in the x-z direction and the magnetic field along z. The acceleration of the particles is written as,

$$\begin{aligned} \frac{du_x}{dt} &= \frac{q}{m}\left(E_x + u_y B\right), \\ \frac{du_y}{dt} &= \frac{q}{m} u_x B, \\ u_x'' &= -\left(\frac{qB}{m}\right)^2 u_x, \\ u_y'' &= -\left(\frac{qB}{m}\right)^2 \left(\frac{E_x}{B} + u_y\right). \end{aligned} \tag{2.6}$$

In the equation above the subscripts mean along x and y. If $E = 0$ the equation describes a simple harmonic oscillator with cyclotron frequency,

$$\omega_c = \frac{|q|B}{m}. \tag{2.7}$$

Equation 2.6 has the following solutions,

$$\begin{aligned} u_x &= u_\perp \exp i\omega_c t, \\ u_y &= \pm i u_\perp \exp i\omega_c t - \frac{E_x}{B}, \\ x - x_0 &= -i\frac{u_\perp}{\omega_c} \exp i\omega_c t, \\ y - y_0 &= \pm \frac{u_\perp}{\omega_c} \exp i\omega_c t - \frac{E_x}{B} t. \end{aligned} \tag{2.8}$$

Where $u_\perp$ is an integration constant, and $\perp$ means perpendicular to the magnetic field. From the equations above a particle with finite and stationary E and B will gyrate around the magnetic field lines with frequency ω_c and radius,

$$r_L = \frac{u_\perp}{\omega_c}, \tag{2.9}$$

where r_L is called the Larmour radius. The particle's gyro center will drift in the $\mathbf{E} \times \mathbf{B}$ direction,

$$\mathbf{u}_E = \frac{\mathbf{E} \times \mathbf{B}}{B^2}. \tag{2.10}$$

This is called the electric drift. Thus an increased magnetic field leads to decreased Larmor radius and decreased electric drift. A picture of the physical situation is given in figure 2.2. In the upper figure there is no magnetic field and the particles move freely. In the lower figure a magnetic field has been inserted and the particles stick to the magnetic field.

A cylinder geometry as in figure 2.2 create a large plasma sink at the endings. A common way to solve this is by bending the cylinder into a torus (donut shape). When electric current coils are wrapped around the torus to create a toroidal (long way around) magnetic field the device is called a

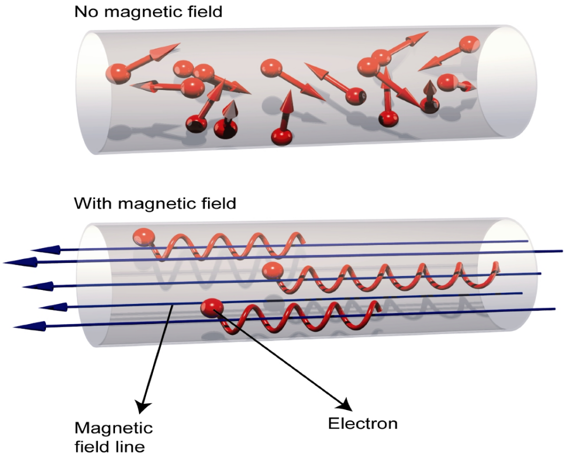

Figure 2.2 – The figure shows the effect of a magnetic field . When a magnetic field is added the particles gyrate around the field lines and stick to them. The figure is found in [44].

tokamak, see figure 2.3. The curved magnetic field will be nonuniform as a function of the radius R from the center, this results in two additional velocities,

$$\begin{aligned} \mathbf{u}_{\nabla B} &= \pm\frac{1}{2}u_{\perp}r_L\mathbf{b}\times\nabla\text{ln}\mathbf{B}, \\ \mathbf{u}_R &= \pm\frac{u_{\perp}^2}{\omega_c}\nabla\times\mathbf{b}. \end{aligned} \tag{2.11}$$

In the equation above $\mathbf{b}$ is the unit vector along the magnetic field $\mathbf{b} = \mathbf{B}/B$. The drift $\mathbf{u}_{\nabla B}$ is called the gradient B drift, caused by variations in gyro radius due to variations in the magnetic field. The drift $\mathbf{u}_R$ is called the curvature drift, caused by a curved magnetic field. An important thing to notice about the drifts above is that both is charge dependent. The ions and electrons move in opposite directions, resulting in charge separation. A charge separation leads to electric field generation which again leads to an electric drift. To counter the effect of charge separation a rotational transform can be used. This is done by introducing a current inside the plasma which generates a magnetic field in the poloidal (short way around) direction. The total magnetic field will spiral around the torus, see figure 2.3. Due to the spiraling shape of the magnetic field the drifts due to the curvature and gradient drifts will be canceled out over one poloidal circuit. The last drift which is important for the single particle picture is the drift

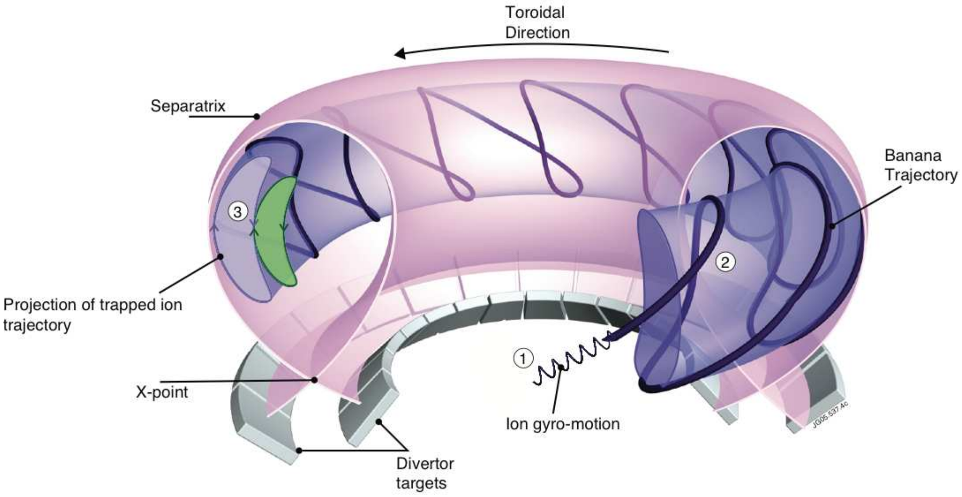

Figure 2.3 – In this figure an overview of a tokamak is given. The figure shows how the particles gyrate around the magnetic field lines in a tokamak with a spiraling magnetic field. The figure also shows how the magnetic field lines are extended out of the main plasma and onto divertor targets. The figure can be found in Pitts [70].

due to a time varying electric field,

$$\mathbf{u}_p = \pm \frac{1}{\omega_c B} \frac{d\mathbf{E}}{dt}. \tag{2.12}$$

The drift $\mathbf{u}_p$ is called the polarization drift.

2.5 Mechanical confinement

In addition to magnetic confinement mechanical devices can be used to keep the plasma away from the walls, see Stangeby [86]. One method is by the use of limiters. A limiter is a thin mechanical structure used to limit the plasma area. It can be inserted either in the toroidal or poloidal direction to short circuit the magnetic field lines outside the main plasma. This creates an area of open magnetic field lines, where the field lines hit the limiter. The limiter is very thin, for a limiter in the poloidal direction particle interaction in toroidal direction is neglectable. When particles hit the limiter the particles are immediately removed from the main plasma, thus the limiter acts as a localizer for the plasma/solid interaction [86].

Another mechanical reduction method is the use of divertor targets [86]. The open magnetic field lines can be extended out of the main plasma by introducing a new current as done in figure 2.3. This current leads to a magnetic field shaped like an eight number where the particles can follow the field lines onto divertor targets located outside the main plasma. This makes it easier to control the excess particles and contamination [86]. Experiments by Umansky, La Bombard and Lipschultz on Alcator C-Mod have shown that a large part of the particles entering the area of open field lines do not reach the divertor targets [52, 55, 91]. Instead they are transported radially outwards. This radial particle transport will be analyzed later.

2.6 Scrape-off layer

The scrape-off layer (SOL) is a term used for the area just outside the closed magnetic field lines. The area in between closed and open field lines are called the separatrix. This thesis will be concerned with high density events seen in the SOL [17]. The reason this area is called the scrape-off layer is that when a particle reach this area, the particle is outside the closed field lines and will be scraped away from the main plasma, either by a divertor target or a limiter. Since the particles are not confined in the SOL the plasma parameters change drastically [64].

2.7 Plasma blobs

Discoveries have shown that even with magnetic and mechanical confinement the plasma loss to the walls is still very large. This high loss is believed to be related to fast moving high density plasma blobs [52, 55, 91]. The plasma blobs are defined as plasma structures much denser than the background plasma aligned with the magnetic field, see figure 2.4. The top figure shows how the plasma blobs are located perpendicular to the magnetic field. Perpendicular to the magnetic field the blobs are circular dots traveling in the radial direction. The bottom figure shows how the blobs are aligned with the magnetic field. The blobs are extended along the magnetic field and is sometimes called filaments. In tokamaks blobs are believed to be generated by a mixture of kink and ballooning magnetohydrodynamics (MHD) instabilities at the separatrix [17, 93]. The MHD model is a single fluid model used to describe macroscopic equilibrium of fusion plasmas [25]. Ballooning is pressure driven instability (perpendicular current driven) and kink is parallel current driven instability. The blobs are transported by an electric drift due to a local charge separation caused by the instability. The instabilities and blob drifts will be discussed more thoroughly in the next chapter. Plasma blobs are not just a phenomena in tokamaks, blobs appear in all toroidal plasma confinement experiments. Blobs carry particles, heat and momentum from the edge region into the SOL, this leads to increased interaction with the SOL, impacting the core plasma confinement [17]. On

Parameter	Value
Major Radius	0.67m
Minor Radius	0.21m
Toroidal Field	2.6 - 8.1 T
Plasma Current	0.4 - 2 MA
Ion Cyclotron Heating	6 MW
Electron density	$10^{19} - 10^{21} m^{-3}$
Core Electron Temp	$\leq$ 9keV
Pulse Length	1-3s

Table 2.1 – In this table the specifics of the Alcator C-Mod tokamak is given. The table is found in Czigler [16].

the positive side blobs can be used to transport the fusion reaction products away from the main plasma [70].

2.8 Alcator C-Mod

The experimental data which will be used is taken from the Alcator C-Mod tokamak located at the Plasma Science and Fusion Center, Massachusetts Institute of Technology (MIT). The Alcator C-Mod has a high magnetic field which makes it possible to reach high levels of plasma temperature and particle density. The specifics of the Alcator C-Mod is given in table 2.1, for more information see Czigler [16]. Alcator C-Mod uses deuterium fuel, thereby avoiding radioactive tritium. The heating in Alcator C-Mod is mostly ohmically, but also ion cyclotron resonance frequency waves and lower-hybrid microwave heating is used [16]. A poloidal cross section of the Alcator C-Mod is given in figure 2.5. In this figure the circular lines in the middle is the closed field lines. The thicker line is the separatrix and on the other side of the separatrix the open field lines can be seen.

2.9 Data acquisition

The data acquisition techniques which will be used are gas puff imaging (GPI) at the outboard mid-plane and Langmuir probe at the upper outboard mid-plane, see figure 2.5. GPI diagnostic consists of injecting neutral Helium gas into the plasma from a nozzle. When the ionized particles collide with the neutral particles they are excited, emitting light. The measurements can then be taken by an optical device measuring the HeI line (587.6 nm) [16, 34, 60]. The measured quantity by the GPI is emissivity ϵ,

$$\epsilon \propto n_0 n_e \Gamma(n_e, T_e). \tag{2.13}$$

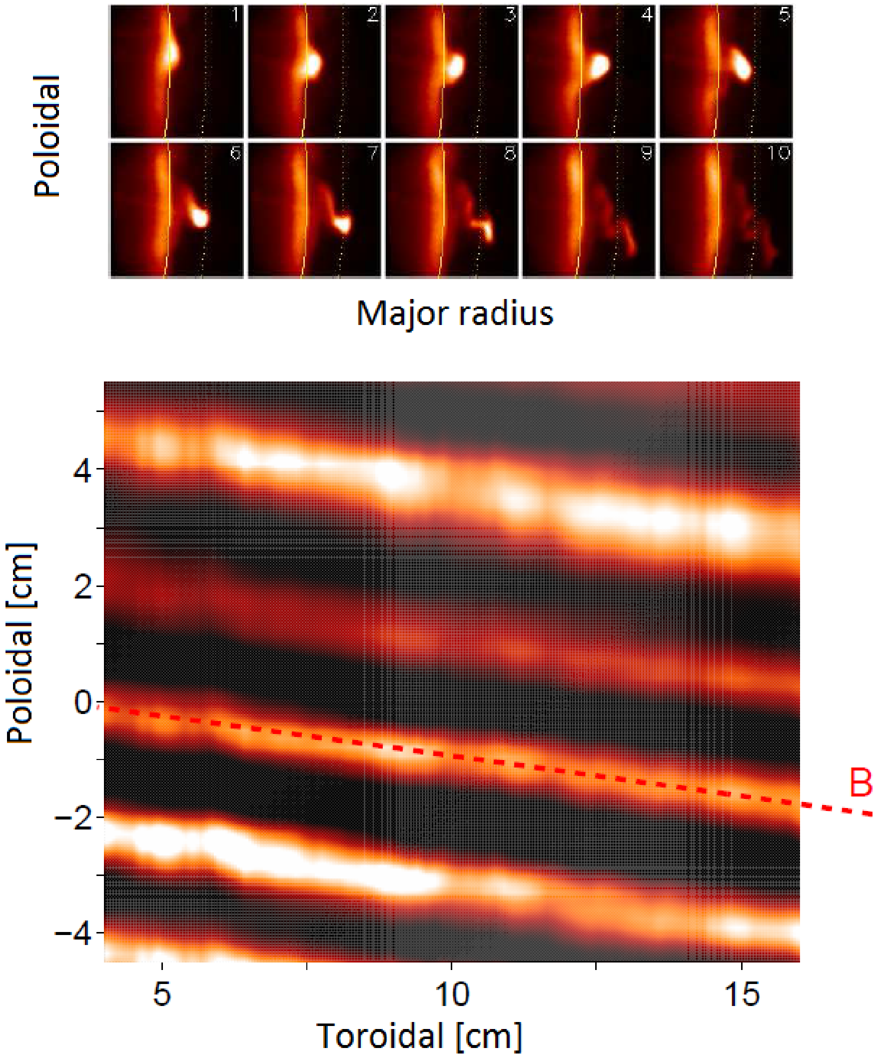

Figure 2.4 – The two figures above show how the plasma blobs are located in space. The top figure shows a plasma blob transported radially outwards, the pictures are taken $8\,\mu s$ apart. The image is taken from the national spherical torus experiment (NSTX) device at Princeton Plasma Physics Laboratory [61]. The bottom figure shows the extension of the plasma blobs along the magnetic field lines. The image is taken from the Alcator C-Mod. The picture is given in Grulke [42].

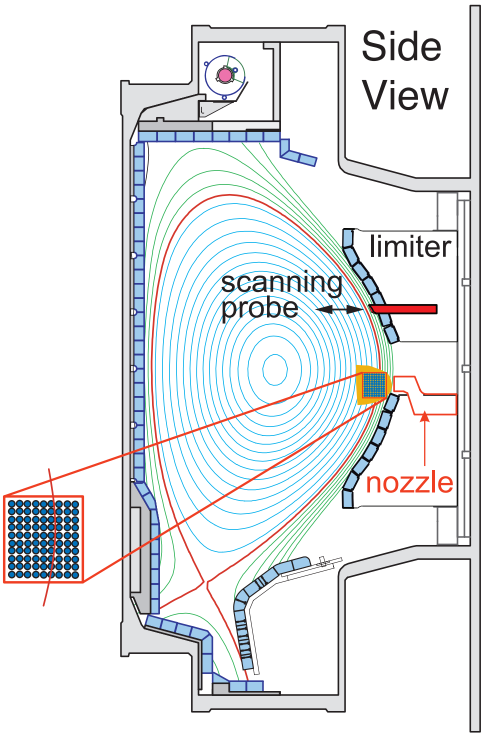

Figure 2.5 – The figure shows a poloidal cross section of the Alcator C-Mod tokamak, [16]. From the figure one can see that the Alcator C-Mod has both limiter and divertor target configurations for reducing plasma/wall interactions. The data acquisition is done on the low field side with both Langmuir probe and a 9x10 grid of GPI data. The GPI nozzle is located at the outboard midplane while the probe is located at the upper outboard midplane. The figure can be found in Garcia [34].

Where n_0 is the neutral atoms, n_e is the electron density, T_e is the electron temperature and Γ is the excitation rate coefficient. The fluctuations of the GPI signals are assumed to be able to approximate the density fluctuations [34]. The GPI data are from the FY2010 run campaign on Alcator C-Mod, a more thorough documentation of the data is given in LaBombard [54]. The data consist of a 9×10 array of data points covering an area $Z = -4.51 - -1.08\,\text{cm}$, $R = 88.00 - 91.08 cm$, sampled with frequency 2 MHz. The radial direction covers four measurements in the SOL, $R = 91.08 - 89.925\,\text{cm}$, one measurement at the separatrix, $R = 89.54\,\text{cm}$ and four measurements in the edge region, $R = 89.155 - 88\,\text{cm}$. Each GPI measured signal has a length of 0.25s. The data acquired is collected at four different line-averaged densities $n_e/n_G = 0.15 - 0.30$, measured by a Langmuir probe in the horizontal direction [34]. The fraction n_e/n_G is the Greenwald fraction where n_e is the electron density. The Greenwald density n_G is defined as,

$$n_G = \frac{I_p}{\pi a^2}, \tag{2.14}$$

where I_p is the plasma current [MA] and a is the plasma minor radius [m], n_G has units of $10^{20} m^{-3}$ [40]. For the GPI data $n_G = 5.26 \times 10^{20} m^{-3}$. One disadvantage with GPI measurements is that it is highly dependent on the temperature. Close to the wall the plasma is relatively cold resulting in low emissivity measures. Far into the plasma the neutral gas becomes ionized, resulting in lower emissions.

Data sampled by Langmuir probes will also be used. The probe collects data in four channels, see figure 2.6. The channels measure ion saturation current ($I_{sat} \propto nT^{1/2}$) and floating potential, with a sampling frequency of 5 MHz. The ion saturation current is measured by using a probe head with a negative potential. The negative potential repels electrons and attracts ions, creating a sheath region, sheath region will be explained in the next section. Thus the current measured by the probe is the ion current, or ion saturation current because it is saturated by ions. The floating potential is the potential needed for equal ion and electron flux towards the probe, $I_{tot} = 0$. The probe data is mostly taken in the far SOL because the probe can not withstand the high temperatures close to the separatrix. Measurements acquired by probes are usually much longer than GPI measurements, because GPI is limited by the duration of the gas puff. The probe data duration varies from $0.3 - 0.8\,\text{s}$. More information about the Langmuir probe can be found in [34, 52]. The measurements sessions used here are 1120210 and 1111208. The session series 1120210 is a measure of only ion saturation current at different line averaged densities ranging from $n_e/n_G = 0.45 - 1.43$. The other physical parameters for that session are $B = 5.4\,\text{T}$, $I_p = 0.8\,\text{MA}$, $R = 0.893\text{m}$ and $\rho = 0.0832\,\text{cm}$, ρ is distance from separatrix mapped to midplane. The session 1111208 has used all probe channels, but for half of

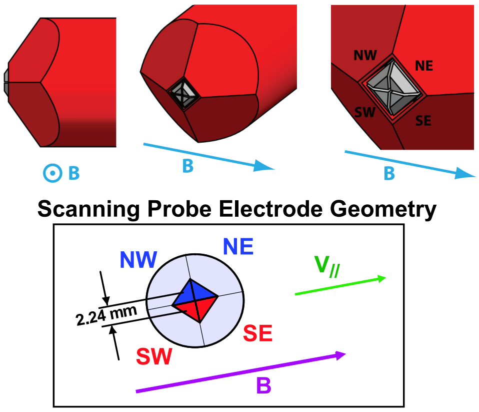

Figure 2.6 – The figure shows the probe head. The probe has four channels measuring ion saturation current and floating potential in the direction perpendicular to the magnetic field. The figure is found in Smick et al. [85]

the data two of the probe heads are damaged. The data is taken for several radii, line averaged densities and plasma currents. $I_p = 0.55\,\text{MA}, 0.8\,\text{MA}$, $B = 5.4\,\text{T}$, $R = 0.860 - 0.870\,\text{m}$, $\rho = 0.109 - 0.116\,\text{cm}$ and $n_e/n_G = 0.59 - 1.57$. Due to different location for the probe and the nozzle R can not be compared between the measurements.

Chapter 3

Physical mechanisms

In this chapter the physical mechanisms behind high density plasma blobs will be analyzed. The chapter will start out with describing the equations governing a plasma in local thermodynamic equilibrium. From these equations a current continuity equation will be derived. By assuming sheath connection and zero vorticity a two dimensional analytical solution will be found as a solution for the blob propagation mechanism.

3.1 Local thermodynamic equilibrium

To simplify the equations of motion a local thermodynamic equilibrium (LTE) is assumed where the heat flux and viscosity are zero [37]. LTE represents a set of closed equations governing the plasma dynamics. In the LTE approximation the velocities follow a Maxwellian distribution function defined as [33],

$$\begin{aligned} f_{\mathbf{u}}(u_{\parallel}) &= \frac{1}{\sqrt{2\pi}C_s}\exp\left(-\frac{1}{2}\frac{u_{\parallel}}{C_s^2}\right), \\ f_{\mathbf{u}}(u_{\perp}) &= \frac{1}{(\sqrt{2\pi}C_s)^2}\exp\left(-\frac{1}{2}\frac{u_{\perp}}{C_s^2}\right). \end{aligned} \tag{3.1}$$

In the equation the subscripts mean parallel and perpendicular to the magnetic field, u is the velocity, and C_s is the isothermal sound speed,

$$C_s = \left(\frac{T}{m}\right)^{1/2}. \tag{3.2}$$

In the equation above T [J] is the temperature and m is the mass. By neglecting the collisional effects the particle continuity and momentum equation in the LTE approximation can be written as,

$$\frac{\partial n}{\partial t} + \nabla \cdot (n\mathbf{u}) = 0, \tag{3.3}$$

$$mn\,\frac{d}{dt}\mathbf{u} = -\nabla p + qn(\mathbf{E} + \mathbf{u}\times\mathbf{B}), \tag{3.4}$$

In the equation above n is the particle density, p is the pressure, q is the elementary charge, $\mathbf{E}$ is the electric field and $\mathbf{B}$ is the magnetic field. The derivative d/dt is the convective derivative, representing a coordinate system traveling with the particle,

$$\frac{d}{dt} = \left(\frac{\partial}{\partial t} + \mathbf{u}\cdot\nabla\right). \tag{3.5}$$

The first equation above (3.3) is the continuity equation and the second (3.4) is the momentum equation. The relevant forces acting on the fluid are the Lorentz force and a pressure gradient force.

3.2 Fluid drifts perpendicular to the magnetic field

The drifts perpendicular to the magnetic field can be found by a cross product between the equation of motion and the magnetic field [15]. For simplicity the velocity will be split up into one component parallel to the magnetic field $\mathbf{u}_{||}$ and one perpendicular component $\mathbf{u}_\perp$,

$$\begin{aligned}\mathbf{B}\times(mn\frac{d}{dt}\mathbf{u}_\perp) =& qn(\mathbf{B}\times\mathbf{E}) + qn\mathbf{B}\times(\mathbf{u}\times\mathbf{B}) - \mathbf{B}\times\nabla p,\\ Bmn\left(\mathbf{b}\times\frac{d}{dt}\mathbf{u}_\perp\right) =& Bqn(\mathbf{b}\times\mathbf{E}) + qnB^2\mathbf{u}_\perp + B\nabla p\times\mathbf{b},\end{aligned} \tag{3.6}$$

where $\mathbf{b} = \mathbf{B}/B$ is the unit vector along $\mathbf{B}$. The perpendicular velocity can be written as a sum of three velocities,

$$\mathbf{u}_\perp = \underbrace{\frac{1}{B}(\mathbf{E}\times\mathbf{b})}_{1} + \underbrace{\frac{1}{qnB}(\mathbf{b}\times\nabla p)}_{2} + \underbrace{\frac{m}{qB}(\mathbf{b}\times\frac{d}{dt}u_{s\perp})}_{3}. \tag{3.7}$$

1. The first drift in equation (3.7) is the $\mathbf{E}\times\mathbf{B}$ drift also called electric drift. The drift is independent of mass and charge of the particles.

2. The second term is the diamagnetic drift. The diamagnetic drift is called a "fictions drift" because it does not appear for guiding center motions [15]. This drift will be analyzed further in the next section.

3. For a magnetized plasma the velocity can to the lowest order be approximated by the electric drift [37]. Thus the third drift can to the lowest order be written as,

$$\frac{m}{qB}\left(\mathbf{b}\times\frac{d}{dt}\mathbf{u}_\perp\right) = \frac{m}{qB}\left[\mathbf{b}\times\frac{d}{dt}\left(\frac{1}{B}(\mathbf{E}\times\mathbf{b})\right)\right] = \frac{m}{qB^2}\frac{d}{dt}\mathbf{E}. \tag{3.8}$$

   The magnetic field is assumed to have only small variations. Hence the third velocity is just the polarization drift introduced previously.

3.2.1 Relation between particle and fluid drifts

In the fluid picture there is an extra drift not seen in the single particle picture, the diamagnetic drift. In addition the drift due to curvature and gradient of the magnetic field is not seen in the fluid description. This is only on the surface, in the following it will be shown that the diamagnetic drift contains both the grad B and curvature drifts. The grad B and curvature drift was introduced in the previous section, see equation (2.11),

$$\mathbf{u}_B = \frac{mu_\perp^2}{2qB}\mathbf{b}\times\nabla\ln B + \frac{mu_\parallel^2}{qB}\nabla\times\mathbf{b}. \tag{3.9}$$

Equations for temperature can be derived from the Maxwellian distribution functions (3.1),

$$T = \left\langle \frac{1}{2}mu_\perp^2 \right\rangle = \left\langle mu_\parallel^2 \right\rangle. \tag{3.10}$$

The half in front of the perpendicular component comes from the fact that the perpendicular component covers two dimensions. With these equations the average of the velocity can be written as,

$$\langle \mathbf{u}_B \rangle = \frac{T}{qB}\mathbf{b}\times\nabla\ln B + \frac{T}{qB}\nabla\times\mathbf{b}. \tag{3.11}$$

The current due to the curvature and grad B drift can be found by [87],

$$\mathbf{J}_B = \sum_{s=i,e} q_s n_s \langle \mathbf{u}_B \rangle_s = \frac{P}{B}\left(\mathbf{b}\times\nabla\ln B + \nabla\times\mathbf{b}\right), \tag{3.12}$$

where $P = p_e + pi = n_i T_i + n_e T_e$ is the total pressure. In the equation above simple SOL is assumed where there is only one singly charged ion species. When matter is inserted in a magnetic field the matter becomes magnetized. This will create a bound current called the magnetization current [33],

$$\begin{aligned}
\mathbf{J}_M &= \nabla\times\mathbf{M} \\
&= \sum \nabla\times\left(n\langle\mu\rangle\right) \\
&= \nabla\times\sum\left(-n\frac{m}{2B}\left\langle u_\perp^2\right\rangle\mathbf{b}\right) \\
&= \nabla\times\left(-\frac{P}{B}\mathbf{b}\right) \\
&= -\frac{P}{B}\left(\nabla\times\mathbf{b}\right) + \frac{1}{B}\mathbf{b}\times\nabla P - \frac{P}{B}\mathbf{b}\times\ln B.
\end{aligned} \tag{3.13}$$

In the equation above μ is the magnetic moment defined as,

$$\mu = -\frac{mu_\perp^2}{2B}\mathbf{b}. \tag{3.14}$$

It can now be seen that,

$$\mathbf{J}_B + \mathbf{J}_M = \frac{1}{B}\mathbf{b} \times \nabla P = \mathbf{J}_d. \tag{3.15}$$

In a uniform magnetic field the diamagnetic current describes diamagnetism, while for non-uniform magnetized plasma it additonally describe the grad-B and curvature drifts. The divergence of the diamagnetic current can now be found from straight forward calculation,

$$\begin{aligned}\nabla \cdot \mathbf{J}_d &= \nabla \cdot (\mathbf{J}_B) + \nabla \cdot (\mathbf{J}_M) \\ &= \nabla \cdot (\mathbf{J}_B) + \nabla \cdot (\nabla \times \mathbf{M}) \\ &= \nabla \cdot (\mathbf{J}_B) \\ &= \left(\frac{1}{B}\nabla \times \mathbf{b} + \frac{1}{B}\mathbf{b} \times \nabla \ln B\right) \cdot \nabla P.\end{aligned} \tag{3.16}$$

Where in the last step the plasma is assumed to be weakly magnetized. This relation will be used in the next section.

3.3 Simplified blob model

The physical mechanism for radial motion of the blob-like structures is illustrated in figure 3.1 [30]. Consider a blob with particle density larger than the background density. A radial force F will cause a charge separation in the vertical direction, caused by the $\mathbf{F} \times \mathbf{B}$ drift. The charge separation will lead to an electric field from positive to negative charge. A radial electric drift will be generated by the charge separation. For a tokamak the forces leading to charge separation are the curvature and grad B force. The blob itself is believed to be created by the MHD instabilities kink and ballooning mode [93]. The instability mechanism is given in figure 3.2. In the figure the sinusoidal curve is a constant density perturbation $\tilde{n}$ on the background density n_0. The gradient and curvature drift leads to a force transporting ions downwards in the figure and electrons upwards. Since the background density is increasing to the left there are more ions coming down to point A than electrons from below. Thus a positive charge will build up at point A. At point C the roles are changed, here a negative charge will build up. Electric drifts will be produced, increasing the perturbation [15]. Propagating blobs will be generated to achieve equilibrium.

3.3.1 Mathematical model

Derivations of mathematic blob models have been done in previous studies [17,19,30–32,47,48], the derivations done in this section follow those papers closely. A simple model for describing blob propagation can be derived from

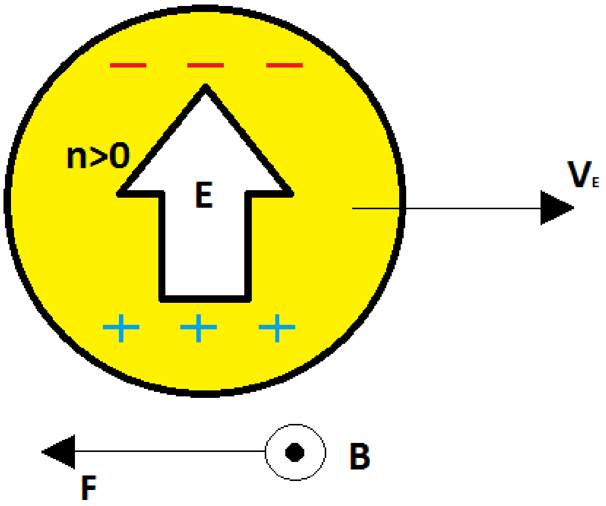

Figure 3.1 – The figure describes the mechanisms for radial blob transport. A charge dependent force perpendicular to the magnetic field generates a charge separation in the blob. From the charge separation an electric field is created which results in a drift in the $\mathbf{E} \times \mathbf{B}$ direction.

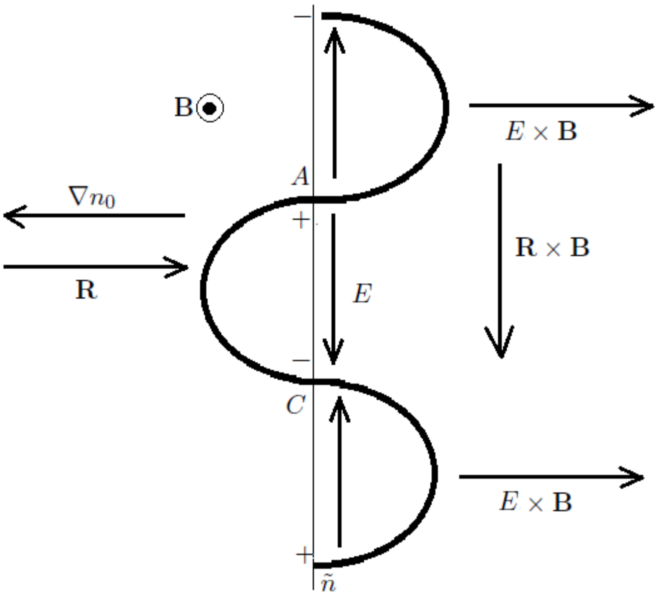

Figure 3.2 – In this figure a density perturbation cause charge separation from the curvature and grad B drifts. The charge separation leads to an $E \times B$ drift which will increase the perturbation and generate plasma blobs.

the current continuity equation for a quasi neutral plasma ($n_i \approx n_e = n$) [30],

$$\nabla \cdot \mathbf{J} = \nabla \cdot \mathbf{j}_{\perp} + \nabla \cdot \mathbf{j}_{\|} = 0. \tag{3.17}$$

The perpendicular current can be found by using the perpendicular drift equation in the previous section. For cold ions ($T_i = 0$) and massless electrons ($m_e = 0$) the perpendicular ion and electron velocity is,

$$\begin{aligned} \mathbf{u}_{i\perp} &= \mathbf{u}_E + \mathbf{u}_{pi} \\ \mathbf{u}_{e\perp} &= \mathbf{u}_E + \mathbf{u}_{de} \end{aligned} \tag{3.18}$$

Where $\mathbf{u}_E$ is the electric drift, $\mathbf{u}_{pi}$ is the polarization drift and $\mathbf{u}_{de}$ is the diamagnetic drift. The perpendicular current can then be written as,

$$\begin{aligned} \mathbf{J}_{\perp} &= ne\left(\mathbf{u}_i - \mathbf{u}_e\right) \\ &= ne\left(\mathbf{u}_E + \mathbf{u}_{pi} - \mathbf{u}_E - \mathbf{u}_{de}\right) \\ &= \frac{nM}{B}\left(\mathbf{b} \times \frac{d}{dt}\mathbf{u}_E\right) + \frac{nm}{B}\left(\mathbf{b} \times \nabla p\right). \end{aligned} \tag{3.19}$$

The divergence of the polarization drift can be found by considering a quasi static state, weak variations in the magnetic field and thin layer approximation [26],

$$\begin{aligned} \nabla \cdot \mathbf{J}_p &= \nabla \cdot \left(\frac{nM}{B}\mathbf{b} \times \left(\frac{\partial}{\partial t} + \mathbf{u}_E \cdot \nabla\right)\mathbf{u}_E\right) \\ &\approx -\frac{nM}{B^2}\left(\frac{\partial}{\partial t} + \mathbf{u}_E \cdot \nabla\right)\nabla_{\perp}^2 \phi. \end{aligned} \tag{3.20}$$

Where ϕ is the electrostatic potential $\mathbf{E} = -\nabla\phi$. The toroidal magnetic field in a tokamak can be found by Ampere's law,

$$\begin{aligned} \oint_C d\mathbf{l} \cdot \mathbf{B} &= \mu_0 I, \\ \mathbf{B}_{\phi} 2\pi R &= \mu_0 I, \\ \mathbf{B}_{\phi}(R) &= \frac{\mu_0 I}{2\pi R} = \frac{B_0 R_0}{R}. \end{aligned} \tag{3.21}$$

In the equation above B_0 is the magnetic field at the major radius R_0 and I is the total current. In the next step a slab will be considered where a local Cartesian coordinate system is used. The z-axis along $\mathbf{B}$, the radial direction along the x-axis and y is the vertical direction. The toroidal magnetic field is assumed to be much larger than the poloidal. The divergence of the diamagnetic current was given in the previous section, see equation (3.16). The electrostatic limit will be assumed [30], the magnitude of the curvature and grad B drifts are equal,

$$\begin{aligned}\nabla \cdot \mathbf{J}_d &= \frac{1}{B}\left(\nabla \times \mathbf{b} + \mathbf{b} \times \nabla \ln B\right) \cdot \nabla p \\ &= \frac{2}{B}\mathbf{b} \times \nabla \ln B \cdot \nabla p \\ &= -\frac{2}{BR}\frac{\partial p}{\partial y}.\end{aligned} \tag{3.22}$$

The full current continuity equation (3.17) can now be written as,

$$\nabla \cdot \mathbf{J} = -\frac{nM}{B^2}\left(\frac{\partial}{\partial t} + \mathbf{u}_E \cdot \nabla\right)\nabla_\perp^2 \phi - \frac{2}{BR}\frac{\partial p}{\partial y} + \nabla \cdot \mathbf{J}_\parallel = 0. \tag{3.23}$$

In order to solve this equation the parallel currents must be determined. Two such limits will be discussed. The first limit is the inertial limit where the plasma is so resistive that the parallel currents can be neglected. Thus the blob is solely driven by the perpendicular current, this is called the ballooning mode. The other limit assumes weak resistive plasma where the parallel currents can be represented by its boundary values. The last case gives an exact analytical two dimensional blob model.

Inertial limit

In the inertial limit the divergence of the parallel current is neglected, the plasma is very resistive [47]. This means high momentum loss from collisions. Collisions lead to large radial particle transport, the particles does not reach the divertor targets. In this limit the blobs are driven by the pressure gradient, consistent with the ballooning instability. A tokamak configurations is favorable where the curvature is concave, high field side, and unfavorable where the curvature is convex, low field side, see figure 3.3. Consider now an instability mechanism as in figure 3.2. At the favorable side the curvature will be negative such that the resulting electric drift will reduce the instability. At the unfavorable side, the instability will be as in figure 3.2. This is consistent with experiments on Alcator C-mod where it has been seen that fluctuations on low field side is ten times larger than fluctuations at high field side [53, 90].

In the inertial limit the current continuity equation can be written as,

$$\left(\frac{\partial}{\partial t} + \mathbf{u}_E \cdot \nabla\right)\nabla_\perp^2 \phi + \frac{2}{MnR}\frac{\partial p}{\partial y} = 0. \tag{3.24}$$

The particle density can be split up into a constant background density N plus a fluctuating density η of order 1 with amplitude Δn,

$$n = N + \Delta n \eta(y, t). \tag{3.25}$$

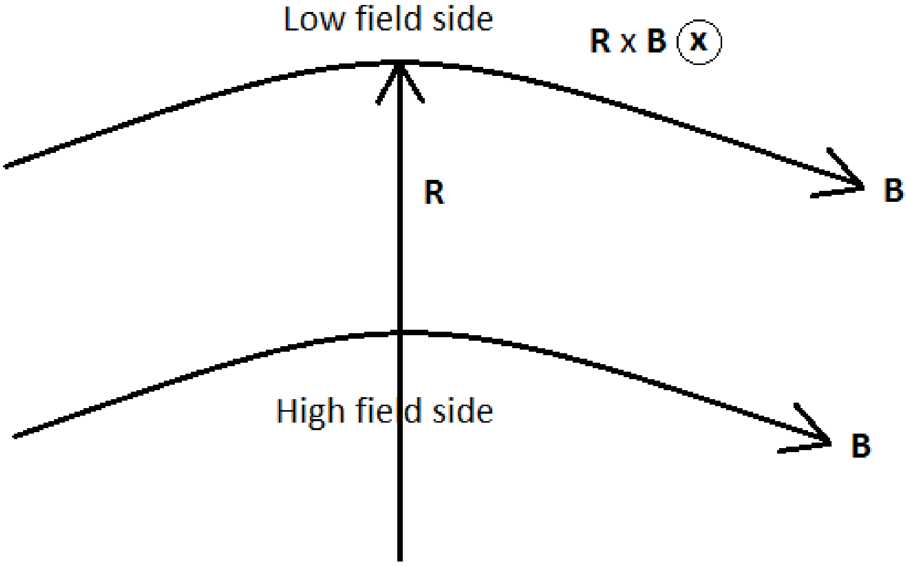

Figure 3.3 – This figure shows a tokamak configuration as seen from above. In the figure is is shown where the torus is favorable (high field side) and unfavorable (low field side.

With the use of the equation above and isothermal temperature the last term on the right hand side of equation (3.24) can be written as,

$$\frac{2}{\rho R}\frac{\partial p}{\partial y} = \frac{2T}{MR}\frac{\Delta n}{n}\frac{\partial \eta}{\partial y} \tag{3.26}$$

If the fluctuating part are assumed to be much smaller than the background $\Delta\, n/N \ll 1$ equation (3.24) can be written as,

$$\left(\frac{\partial}{\partial t} + \mathbf{u}_E \cdot \nabla\right)\nabla_\perp^2 \phi + \frac{2T}{MR}\frac{\Delta n}{N}\frac{\partial \eta}{\partial y} = 0. \tag{3.27}$$

The dimensionless form of the current continuity equation can be found by using $t' = t/\tau$, $y' = y/l$, $x' = x/l$, $\mathbf{u}'_E = \tau \mathbf{u}_E/l$ and $\phi' = \tau\phi/(Bl^2)$, this gives the following equation,

$$\left(\frac{1}{\tau}\frac{\partial}{\partial t'} + \frac{l}{l\tau}\mathbf{u'}_E \cdot \nabla'\right)\frac{1}{\tau}\nabla'^2_\perp\frac{\phi'}{B} + \frac{2T}{MRl}\frac{\Delta n}{N}\frac{\partial \eta}{\partial y'} = 0. \tag{3.28}$$

To reduce the model equations to a form with no parameters the non-dimensional time scale can be chosen as,

$$\tau = \left(\frac{MRl}{2T}\frac{N}{\Delta n}\right)^{1/2}. \tag{3.29}$$

The non dimensional equation (3.28) then reduce to,

$$\left(\frac{\partial}{\partial t'} + \mathbf{u}'_E \cdot \nabla'\right) \nabla'^2_\perp \frac{\phi'}{B} + \frac{\partial \eta}{\partial y'} = 0. \tag{3.30}$$

The ideal velocity scale is found by dividing the length scale by the time scale,

$$V = \frac{l}{\left(\frac{MRl}{2T}\frac{N}{\Delta n}\right)^{1/2}} = \left(\frac{2Tl}{MR}\frac{\Delta n}{N}\right)^{1/2} = C_s\left(2\frac{l}{R}\frac{\Delta n}{N}\right)^{1/2}. \tag{3.31}$$

From the equation above the blob velocity in the inertial regime increases with the square root of the blob size, decreases with increasing major radius and increases with $(\Delta n/N)^{1/2}$. The last relation has been investigated more thoroughly in Kube and Garcia [50], in experiments this value is not necessarily small.

The transit times can be estimated by assuming, $\Delta_{SOL} = 25$mm, $l = 1.5$cm, $R = 0.9$m, $L_{\|} = 12$m and $\Delta n/N \approx 1$,

$$\begin{aligned} \tau_\perp &= \frac{\Delta_{SOL}}{V} = \frac{1}{C_s}0.0137m, \\ \tau_{\|} &= \frac{L_{\|}}{C_s} = \frac{1}{C_s}12m. \end{aligned} \tag{3.32}$$

In the equation above $L_{\|}$ is the half length between divertors and the parallel velocity is C_s [86]. Thus in this limit the plasma loss rate along the magnetic field is negligible compared to the perpendicular loss, as was assumed when neglecting the perpendicular current.

Sheath connected limit

In the sheath connected limit the plasma is weakly resistive. Particles flow freely along the magnetic field without collisions. Slow radial velocities generate connection between the divertor targets. The resulting parallel current can be represented by the boundary conditions at the sheath edge. The sheath region is the region close to the divertor targets where quasi neutrality is no longer fulfilled, $n_i > n_e$. The reason for this charge imbalance is that immediately after ionization the fast moving electrons are transported towards the solid surfaces. Thus a negative potential builds up on the solid surface. This will generate an ambipolar electric field which will accelerate the ions and slow down the electrons, creating ambipolar outflow $\mathbf{u}_e = \mathbf{u}_i$. Within a short distance called the Debye length, the ions will shield out the potential from the electrons. The shielding is not perfect, a small electric

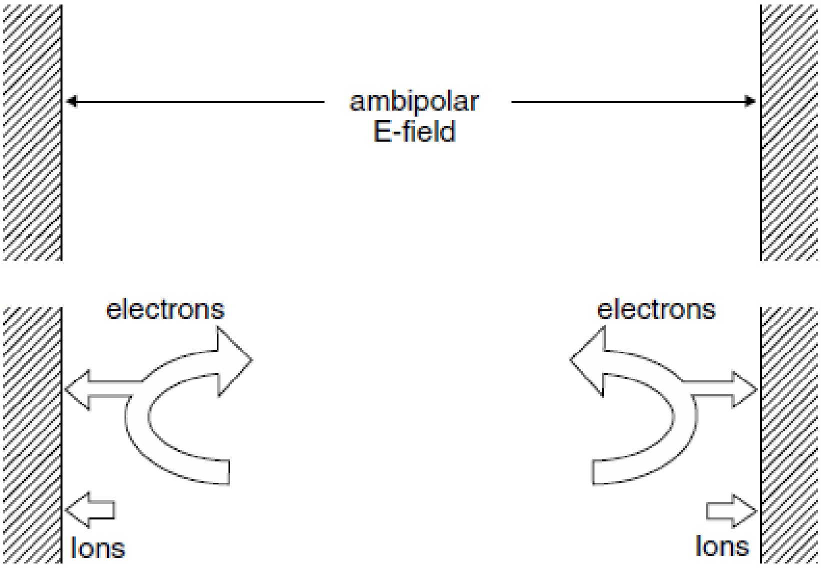

Figure 3.4 – In the figure above it is shown how the ambipolar electric field works. The electrons with too small kinetic energy is repelled resulting in equal loss of electrons and ions. The figure is found in Stangeby [86].

field will penetrate generating a pre-sheath electric field. This pre-sheath electric field will also be ambipolar acting as a repulsive force for the electrons and an attractive force for the ions, see figure 3.4. In order for the electrons to reach the solid walls they have to have a velocity large enough to overcome the potential energy barrier, see appendix. For simplicity the ions is as before assumed cold and the electrons are assumed to be Boltzmann distributed [86]. The Boltzmann distribution rise due to force balance between the pressure gradient pushing the electrons towards the solid surface and the repulsive force due to the potential barrier,

$$n_e = n_0 \exp\left(-e(\phi - \phi_0)/T_e\right). \tag{3.33}$$

Where n_0 and ϕ_0 is the value of the density and potential at the sheath edge. The velocity the particles must have to overcome the sheath potential barrier is defined by the Bohm criterium, derived in the appendix,

$$u_0 \geq C_s. \tag{3.34}$$

In the equation above u_0 is the sheath velocity and C_s is the isothermal sound speed. In an isothermal plasma the velocity can not exceed the isothermal sound speed [86], thus,

$$u_0 = C_s. \tag{3.35}$$

The parallel current at the sheath edge can then be written as,

$$\begin{aligned}\mathbf{J}_{\parallel 0} &= \sum_{s=i,e} q_s n_s u_s \\ &= e n_0 C_s \left[1 - \exp\left(e\left(\phi - \phi_0\right)/T\right)\right] \\ &= e^2 n_0 C_s \left(\phi - \phi_0\right)/T + \vartheta\left(\phi - \phi_0\right)^2\end{aligned} \tag{3.36}$$

A 2-dimensional model for the blob propagation can be found by integrating the current continuity equation (3.17) along the magnetic field. The perpendicular current is assumed to be constant along the magnetic field,

$$\int_{-L_\parallel}^{L_\parallel} \nabla \cdot \mathbf{J} dl = 2L_\parallel \nabla \cdot \mathbf{J}_\perp + 2\mathbf{J}_{\parallel 0} = 0. \tag{3.37}$$

Thus the full current continuity equation can be written as,

$$\frac{nM}{B^2}\left(\frac{\partial}{\partial t} + \mathbf{u}_E \cdot \nabla\right)\nabla_\perp^2 \phi + \frac{2}{BR}\frac{\partial n}{\partial y} = \frac{e^2 n_0 C_s}{L_\parallel}\left(\phi - \phi_0\right)/T. \tag{3.38}$$

An analytical solution is found when the vorticity is zero,

$$\nabla_\perp^2 \phi = 0. \tag{3.39}$$

By neglecting collisions the equation of particle continuity can to the lowest order be written as,

$$\frac{dn}{dt} = \frac{\partial n}{\partial t} + \mathbf{u}_E \cdot \nabla n = \frac{\partial n}{\partial t} + \frac{1}{B}\mathbf{b} \times \nabla\phi \cdot \nabla n = 0. \tag{3.40}$$

The potential can be found from equation (3.38) and inserted into equation (3.40) to find an equation for the density. The potential can be written as,

$$\phi = \phi_0 + \frac{2C_s M L_\parallel T}{RBne^2}\frac{\partial n}{\partial y} = \phi_0 + \frac{2BL_\parallel T}{Rn} C_s \rho_s \frac{\partial n}{\partial y} \tag{3.41}$$

Where $\rho_s = C_s/\omega_{ci}$ is the hybrid thermal gyro radius. Now assuming that $\mathbf{B}$ is along the z-axis the electric drift can be rewritten as,

$$\mathbf{u}_E = \frac{1}{B}\mathbf{b} \times \nabla\phi = 2C_s\rho_s^2\frac{L_\parallel}{R}\left(-\frac{\partial}{\partial y}\left(\frac{1}{n}\frac{\partial n}{\partial y}\right)\hat{\mathbf{x}} + \frac{\partial}{\partial x}\left(\frac{1}{n}\frac{\partial n}{\partial y}\right)\hat{\mathbf{y}}\right). \tag{3.42}$$

This equation can be inserted into the particle continuity equation to yield,

$$\frac{\partial n}{\partial t} + 2C_s\rho_s^2\frac{L_\parallel}{R}\left\{\frac{\partial}{\partial y}\left[n\frac{\partial}{\partial x}\left(\frac{1}{n}\frac{\partial n}{\partial y}\right)\right] - \frac{\partial}{\partial x}\left[n\frac{\partial}{\partial y}\left(\frac{1}{n}\frac{\partial n}{\partial y}\right)\right]\right\} = 0. \tag{3.43}$$

The equation above can be solved by separation of variables assuming that the density can be written as,

$$n(x, y, t) = A(x, t)B(y). \tag{3.44}$$

Inserting this into equation (3.43) gives,

$$\frac{\partial n}{\partial t} = B(y)\frac{\partial}{\partial t}A(x,t), \tag{3.45}$$

$$\begin{aligned}\frac{\partial}{\partial y}\left[n\frac{\partial}{\partial x}\left(\frac{1}{n}\frac{\partial n}{\partial y}\right)\right] &= A(x,t)\frac{\partial}{\partial x}\frac{\partial^2}{\partial y^2}b(y) = 0,\\ \frac{\partial}{\partial x}\left[n\frac{\partial}{\partial y}\left(\frac{1}{n}\frac{\partial n}{\partial y}\right)\right] &= B(y)\frac{\partial}{\partial x}A(x,t)\frac{\partial^2}{\partial y^2}\ln(A(x,t)).\end{aligned} \tag{3.46}$$

From the equations above the continuity equation (3.43) can be simplified,

$$\frac{dn}{dt} = \frac{\partial}{\partial t}A(x,t) - 2C_s\rho_s^2\frac{L_\parallel}{R}\frac{\partial}{\partial x}A(x,t)\frac{\partial^2}{\partial^2 y}\ln[B(y)] = 0. \tag{3.47}$$

This gives,

$$\frac{R}{2L_\parallel C_s\rho_s^2}\frac{A_t}{A_x} = (\ln B)_{yy} = -\frac{1}{\ell^2}, \tag{3.48}$$

where the subscripts $A_t, A_x, (\ln B)_{yy}$ means derivative with respect to t, x and double derivative in y. Since each side is dependent on different variables both sides equals a constant -$1/\ell^2$ [21]. The reason for choosing the constant equal to $1/\ell^2$ will become clear later. The y dependent part of (3.48) can be written as,

$$\frac{\partial^2\ln(B)}{\partial^2 y} = -\frac{1}{\ell^2}, \tag{3.49}$$

which has an exponential solution of the form,

$$B \propto \exp[-\frac{1}{2}(y/\ell)^2]. \tag{3.50}$$

l can now be interpreted as the poloidal scale length, since y is in the poloidal direction for the slab geometry used here. The second equation can be written as,

$$\frac{R}{2L_\parallel C_s\rho_s^2}A_t = -\frac{1}{\ell^2}A_x. \tag{3.51}$$

The solution of this equation can be written as,

$$A(x,t) = f(x - V_b t). \tag{3.52}$$

In the equation above f is an arbitrary function and V_b is the velocity of blob propagation given by,

$$\frac{V_b}{C_s} = 2\left(\frac{\rho_s}{\ell}\right)^2\frac{L_\parallel}{R}. \tag{3.53}$$

Equation (3.52) has the the form of an object traveling along x with speed V_b. The equation for V_b shows that the speed is dependent on $1/\ell^2$, so the speed decreases with increasing blob size squared. The total equation for the density can be written as,

$$n(x, y, t) = f(x - V_b t)\exp[-1/2(y/\ell)^2], \tag{3.54}$$

with potential,

$$\phi = \phi_0 - y\frac{2BL_{\|}TC_s\rho_s}{R\ell^2}. \tag{3.55}$$

The equations (3.53, 3.54, 3.55) is an exact analytical solution to equation (3.38) for a plasma without vorticity located in vacuum ($y \gg 1 \to n = 0$). The main problem with this simple solution is that the plasma is assumed collisionless thus the blobs are localized throughout the whole poloidal direction, not consistent with ballooning [30]. When the driving mechanism is dominated by parallel current as is done here it is called the kink mode, more information about the kink mode can be found in Freidberg [25]. The transit times can be calculated by assuming, $T_e = 30\,\mathrm{eV}$, $B = 4\,\mathrm{T}$, $\Delta_{SOL} = 25\,\mathrm{mm}$, $l = 1.5\,\mathrm{cm}$ and $R = 0.9\,\mathrm{m}$,

$$\begin{aligned} \tau_\perp &= \frac{\Delta_{SOL}}{V_b} = \frac{1}{C_s}1.1m, \\ \tau_\| &= \frac{1}{C_s}12m. \end{aligned} \tag{3.56}$$

Thus it takes 10 times longer time to reach the divertor target than it takes to reach the wall. A more thorough investigation of the blob velocity is done on numerical simulation by Kube and Garcia [49–51].

Chapter 4

Statistical methods

In this chapter the statistical methods will be introduced and explained. The chapter will mostly focus on long range correlation and how they can be estimated. At the end of the chapter the methods will be tested on computer generated data.

4.1 Probability density function (PDF)

A probability density function $f_X(x)$ is a continuous function used to describe the probability of a random variable, X, to lie within a certain region [75],

$$P[x < X \leq x + dx] = f_X(x)dx. \tag{4.1}$$

In the equation above P is the probability. Thus the probability for a random variable to lie between a and b can be found by integrating equation 4.1 from a to b. Another variant is the cumulative probability distribution function which describe the probability of a random variable to be less than or equal a given value x,

$$P(X \leq x) = \int_{-\infty}^{x} f_X(x)dx. \tag{4.2}$$

Later the complementary version of the equation above will be used, that is the probability for X to be greater than x. From the probability density function the moments can be found by [87],

$$\begin{aligned}
E[x] = \mu &= \int_{-\infty}^{\infty} x f(x)dx, \\
E[(x-\mu)^2] = \sigma^2 &= \int_{-\infty}^{\infty} (x-\mu)^2 f(x)dx, \\
E[(x-\mu)^3] = S\sigma^{3/2} &= \int_{-\infty}^{\infty} (x-\mu)^3 f(x)dx, \\
E[(x-\mu)^4] = K\sigma^2 &= \int_{-\infty}^{\infty} (x-\mu)^4 f(x)dx.
\end{aligned} \tag{4.3}$$

The number of moments in the equation above could go on to infinity, but it is the first four which are most important. The first moment in the equation above is the mean value, which says something about where in space/time the density function is centered. The three consecutive equations are subtracted by the mean value and are therefore called central moments. The second central moment is the variance, it measures the spread of the density function. The third central moment is the unnormalized skewness. Skewness (S) is a measure of asymmetry in the PDF related to the mean value. For a symmetric distribution such as a Gaussian $S = 0$, $S > 0$ represents a shift to the right, $S < 0$ to the left. The fourth order central moments is called kurtosis, a Gaussian distribution has a kurtosis of 3. Kurtosis describes the sharpness of the peak [75].

For experimental data the PDF is estimated with the use of histograms. A histogram is created by sorting the measurements into bins of equal width. Dividing the histogram by the sum of all collected measurements gives the probability for a random measurement to be in any given bin. Thus this is not a true PDF where the distribution integrates to 1, but a probability mass function, which is the discreet case. The probability in the discrete case can be written as,

$$P(X = x) = f_X(x). \tag{4.4}$$

For a probability mass function the sum over the probabilities is equal to 1.

4.1.1 Estimation of moments

The moments introduced above can be estimated by [45, 87],

$$\begin{aligned} \hat{\mu}_x &= \frac{1}{N}\sum_{i=1}^{N} x(i), \\ \hat{\sigma}_x^2 &= \frac{1}{N-1}\sum_{i=1}^{N} (x(i) - \hat{\mu}_x)^2, \\ \hat{S} &= \frac{1}{\hat{\sigma}_x^3 N}\sum_{i=1}^{N} [x(i) - \hat{\mu}_x]^3, \\ \hat{K} &= \frac{1}{\hat{\sigma}_x^4 N}\sum_{i=1}^{N} [x(i) - \hat{\mu}_x]^4. \end{aligned} \tag{4.5}$$

In the equation above $\hat{S}$ and $\hat{K}$ are the biased sample skewness and kurtosis respectively. In this thesis the time series are so long that the bias becomes insignificant, see Joanes and Gill for more information [45].

Another useful method for analyzing events in a signal is the time derivative skewness estimated by [79],

$$\hat{A} = \frac{1}{\hat{\sigma}^3(x_t)N} \sum_{i=1}^{N} [x_t(i) - \hat{\mu}(x_t)]^3. \tag{4.6}$$

This is just the skewness of the time derivative of the signal where,

$$x_t = \frac{dx}{dt}. \tag{4.7}$$

The method describes the time asymmetry in a signal. When A is larger than zero the signal spends more time raising than decaying and vice versa.

4.2 Hurst Exponent

As stated earlier the Hurst exponent is a measure of the long range temporal correlations. The Hurst exponent was first introduced by the British scientist Harold Edwin Hurst while demonstrating long term memory of water discharge times in the Nile river [2]. For a stationary signal the exponent take values between 0 and 1, where a value larger than 1/2 suggests persistence in the data, less than 1/2 indicate anti-persistence and $H = 1/2$ is uncorrelated random data [57]. As mentioned a wide variety of methods can be used to estimate the Hurst exponent. A handful will be used and compared here.

The concept of long range correlations can be visualized with the use of a one step persistent one dimensional random walk. This means a random walk where the next step is dependent on the previous step and the step is either up or down. Persistency means that if the last step was up the probability of going up again will be larger than the probability for going down. When the probability for going up is equal to that of going down the motion is a regular random walk. An increase of persistence is expected to lead to larger motions and therefore also greater dispersion. Therefore the dispersion can be seen as a measure of the long range correlations, where a higher dispersion results in stronger long range correlations. In figure 4.1 a hundred realizations of persistent random walks with $\Delta x = \Delta t = 1$ is plotted for five different persistence probabilities, p. In the figure ϵ represents a normalized standard deviation. When increasing the probability one can see that the spread increases.

In this thesis the Hurst exponent will be estimated from measurements done on the plasma fusion tokamak Alcator C-Mod. In the last decade a lot of research has been done on Hurst exponent estimation in plasma fusion [14, 38, 79, 92].

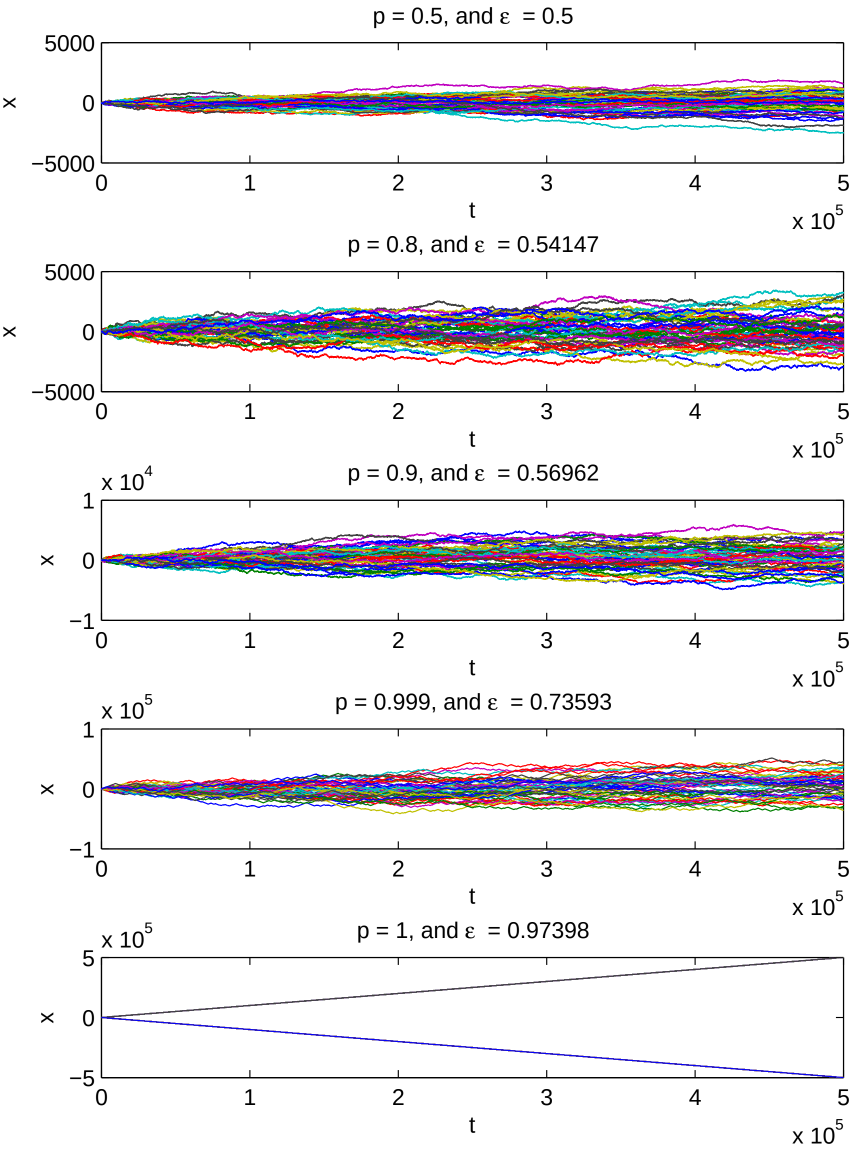

Figure 4.1 – In these figures a hundred realizations of persistent random walks with five different probabilities P is plotted. See that the dispersion increases for increasing probability.

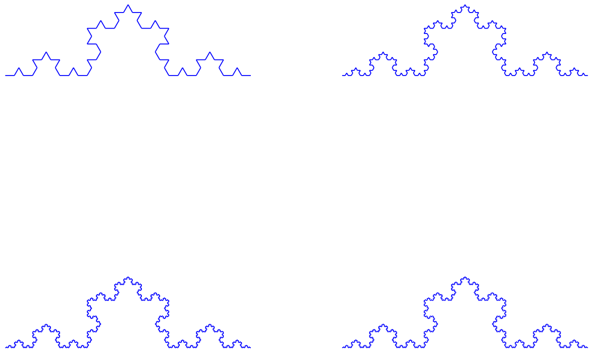

Figure 4.2 – The Koch curve at four different iterations. See that the shape is similar for all iterations. The code used is made by Salman Durrani [22].

4.3 Self-similar process

The definition of a self similar process $X(t)$ is that the distribution is independent of time series length [78]. In other words, the signal has the same statistical properties for every subset of the signal. A useful way to write the self-similar condition, for reasons that will become obvious later, is the H-self similar process given by,

- H-self similar: $X(at) \overset{d}{=} a^H X(t),\ \forall a > 0$.

In the statement above $\overset{d}{=}$ means equal in distribution, H and a are constants. The concept of self similarity can be visualized by a Koch curve. The Koch curve is made by adding a smaller triangular shape in the middle of each straight line for each iteration. Thus a zoom in the figure represents one less iteration. The Koch curve has the same shape at different scales, the curve is plotted for four subsequent iterations in figure 4.2. The curve is an infinite fractal which is continuous everywhere, but not differentiable. Another example of a self similar process from the real world are coastlines. A coastline is also a fractal with infinite length depending on the resolution of the measurements [69].

4.4 Fractional Brownian motion

A fractional Brownian motion (fBm), $X(t)$, is a H-self similar, non-stationary motion with stationary increments [38, 58]. The fBms are also called biased random walks because their behavior is that of a random walk but with a persistent probability.

- Stationary increments: $X(t_0 + t) - X(t_0) \overset{d}{=} X(t) - X(0),\ \forall t_0$.

Stationary increments means that the joint distribution function of the increments is only dependent of the time between increments. The statistics for a fBm is a Gaussian self similar process where H, the self similarity parameter, is the Hurst exponent. The mean value of a fBm is zero [71],

$$E[X(t)] = 0,\ \forall t. \tag{4.8}$$

The covariance for a zero mean signal can be written as,

$$E\left[\{X(t) - E[X(t)]\}\{X(s) - E[X(s)]\}\right] = E[X(t)X(s)]. \tag{4.9}$$

By using the stationary increments condition above and assuming, $X(0) = 0$, the product above can be written as,

$$\begin{aligned} X(t)X(s) &= \frac{1}{2}\left[X(t)^2 + X(s)^2 - \{X(t) - X(s)\}^2\right] \\ &\overset{d}{=} -\frac{1}{2}\left[X(t)^2 + X(s)^2 - X(t-s)^2\right]. \end{aligned} \tag{4.10}$$

The mean value of the equation above is found by the self similarity condition with $a = 1/t$ [71],

$$\begin{aligned} X(at) &\overset{d}{=} a^H X(t), \\ X(1) &\overset{d}{=} \left(\frac{1}{t}\right)^H X(t), \\ t^H X(1) &\overset{d}{=} X(t), \\ t^{nH} X(1)^n &\overset{d}{=} X(t)^n. \end{aligned} \tag{4.11}$$

Since $X(1)$ has the same value for the fBm as for the increment process, σ^2 $= E[X(1)^2]$ is the variance of the increments. The increment process will be explained further in the next section. The correlation can be written as,

$$E[X(t)X(s)] = \frac{1}{2}\sigma^2\left(t^{2H} + s^{2H} - |t-s|^{2H}\right). \tag{4.12}$$

The autocorrelation above follows a power law with exponent $2H$, where $H = 0.5$ is a special case called Brownian motion. Brownian motions is defined as a random walk with white Gaussian noise as increments [57]. The persistence of a fBm becomes clear when looking at fBms for different Hurst exponents as given in figure 4.3. An increased Hurst exponent leads to a smooth signal with slow variations and high global maximas. It is this property the rescaled range analysis, introduced later, attempts to quantify.

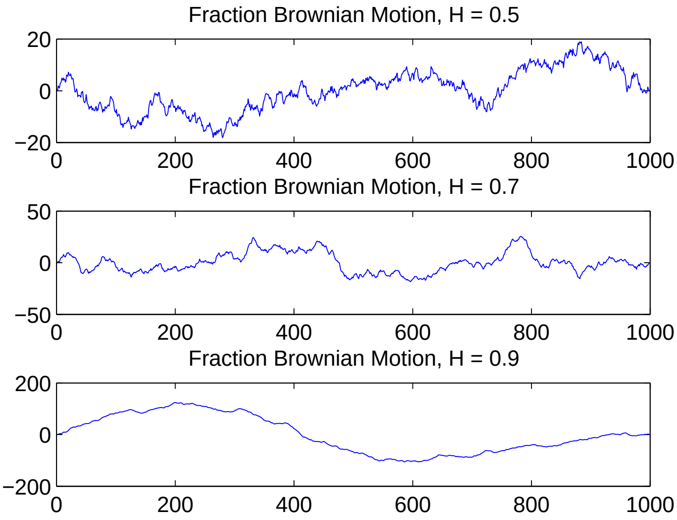

Figure 4.3 – Examples of realizations of fBms at different Hurst exponent. The signals has $\Delta t = \Delta x = 1$. For low Hurst exponent the fBm varies fast with small dispersion. When the Hurst exponent increases the dispersion increases and the variations gets longer and slower.

4.5 Fractional Gaussian noise

Long range temporal correlations have been found in many real world processes. These processes spans a wide variety of sciences from water levels in hydrology to the stock exchange market in economics [69]. Recently it has been put a lot of effort in finding the long range correlations for fluctuation measurements in fusion devices. Especially in relation to turbulence in the edge region of plasmas [10, 12–14, 38, 73, 80, 84, 95]. The theory behind long range correlations comes from analysis based on fractional Gaussian noise (fGn) data. fGns are stationary processes where the cumulative joint distribution function is independent of a time shift t_0 [78],

- Stationary process: $Y(t_0 + t) \overset{d}{=} Y(t),\ \forall t_0$.

A fGn, Y, is defined as the increments of a fBm, X, defined in the previous section,

$$X(k) = \sum_{i=1}^{k} Y(i). \tag{4.13}$$

Assuming continuous signals a fGn can be written as the derivative of a fBm,

$$Y(t) = \frac{dX(t)}{dt}. \tag{4.14}$$

With the use of this relationship the correlation function for a fGn can be found by the double derivative of the correlation for a fBm [71],

$$\begin{aligned}
\rho(t,s) &= E[Y(t)Y(s)] \\
&= \frac{d^2}{dtds}E[X(t)X(s)] \\
&= \frac{d^2}{dtds}\frac{1}{2}\sigma^2\left(t^{2H}+s^{2H}-|t-s|^{2H}\right) \\
&= -\frac{1}{2}\frac{d^2}{dtds}\sigma^2\left(|t-s|^{2H}\right) \\
&= H(2H-1)\sigma^2|t-s|^{2H-2},\ t\neq s
\end{aligned} \tag{4.15}$$

Since a fGn is stationary the equation above can further be reduced to,

$$\rho(t,s)=\rho(\tau)=E[Y(0)Y(\tau)]=H(2H-1)\sigma^2|\tau|^{2H-2},\ \tau\neq 0. \tag{4.16}$$

For $s = t$ it was found in the last section that,

$$\rho(0)=\sigma^2. \tag{4.17}$$

It can be seen that when H is larger than 0.5 the integral of the autocorrelation function diverges, which proves the long range correlation ability. For $H = 0.5$ the integral is σ^2, thus no long range correlations. The last case where $H < 0.5$ exhibit long range correlations [71]. In figure 4.4 realizations of fGns are plotted for different Hurst exponents. Can see that as the Hurst exponent increases the signal tend to fluctuate less randomly.

4.6 Correlation

Correlation function is a statistical method used widely in signal processing for describing the difference and similarities in signals. Correlation can be done on one signal between time steps or between two signals [87].

4.6.1 Cross-Correlation

The cross correlation function is defined as [87],

$$C(s,t)=\frac{E[(X(t)-\mu_X)(Y(s)-\mu_Y)]}{\sigma_X\sigma_Y}. \tag{4.18}$$

where E represents the expectation, σ and μ are respectively the standard deviation and mean value. Dividing by the standard deviation normalizes the function resulting in a maximum value of one. If X and Y are assumed

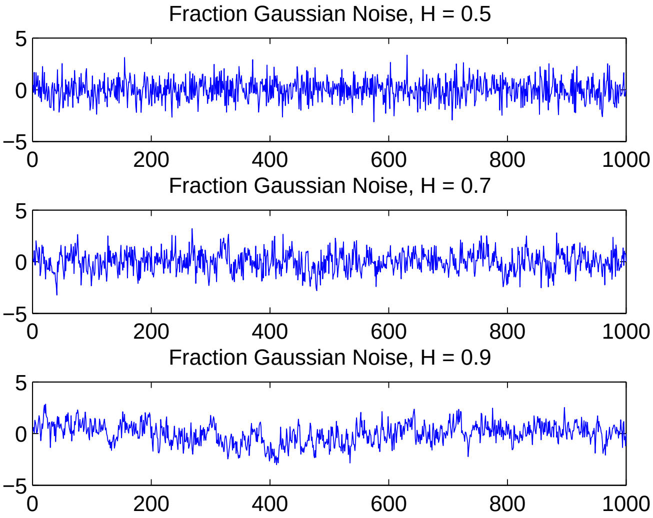

Figure 4.4 – Example of realizations for fGns at different values of the Hurst exponent. In the figure the persistence increases as the Hurst exponent increases.

to be jointly second order stationary, the cross correlation can be written as a function of $\tau = s - t$ [87],

$$C(\tau) = \frac{E[(X(t) - \mu_X)(Y(t+\tau) - \mu_Y)]}{\sigma_X \sigma_Y}. \tag{4.19}$$

Thus the cross correlation is a measure of the similarities between two signals at different time lags. The equation above can be estimated by,

$$\hat{C}(\tau) = \frac{1}{N\hat{\sigma}_X\hat{\sigma}_Y} \sum_{t=1}^{N-\tau} [X(t) - \hat{\mu}_X][Y(t+\tau) - \hat{\mu}_Y] \tag{4.20}$$

Where N is the sample size and $\hat{\mu}$, $\hat{\sigma}$ are respectively the sample mean and sample standard deviation, defined in equation (4.5). Estimated correlation time used later is defined as the time lag of maximum correlation between the two signals. Note that the equation above is a biased estimator for the correlation. The reason for using this version is that for unknown σ and μ the unbiased estimator, where $1/N$ is substituted by $1/(N-\tau)$, is also biased. It has been shown that for many stationary processes the estimator used here has a smaller mean squared error [68].

4.6.2 Autocorrelation Function

The autocorrelation function is defined as the cross-correlation of a signal with itself. By assuming second order stationary signal the autocorrelation can be written as [87],

$$R(\tau) = \frac{E[(X(t) - \mu)(X(t + \tau) - \mu)]}{\sigma^2}. \tag{4.21}$$

The autocorrelation describe the similarities in a signal at different time steps. In equation 4.16 it was found that the autocorrelation for a fGn follows an exponential law [77],

$$\begin{aligned} &\rho(\tau) = E[X(t)X(t + \tau)] \propto \tau^{-\gamma}, \ \tau > 0 \\ &\gamma = 2 - 2H. \end{aligned} \tag{4.22}$$

The Hurst exponent calculated from the autocorrelation is usually not as accurate as the other methods, but a heavy tail in the autocorrelation function usually indicate long range correlations. Estimation of the autocorrelation is similar to the method used for the cross correlation in equation (4.20),

$$\hat{R}(\tau) = \frac{1}{N\hat{\sigma}_X^2} \sum_{t=1}^{N-\tau} [X(t) - \hat{\mu}][X(t + \tau) - \hat{\mu}], \tag{4.23}$$

where $\hat{\mu}$ and $\hat{\sigma}$ are given by equation (4.5).

4.6.3 Pearson correlation coefficient

To get the degree of correlation between two signals it is common to use the Pearson correlation coefficient given by ,

$$r_p = \frac{E[(X - \mu_X)(Y - \mu_Y)]}{\sigma_X \sigma_Y}. \tag{4.24}$$

A value of r = 1 represents fully linear correlation, -1 is fully linear anti-correlation, 0 is no correlation. For a sample the Pearson correlation coefficient can be estimated by [74],

$$\hat{r}_p = \frac{1}{N} \frac{\sum_{t=1}^{N} (X(t) - \hat{\mu}_X)(Y(t) - \hat{\mu}_Y)}{\hat{\sigma}_X \hat{\sigma}_Y}. \tag{4.25}$$

The equation above is just the cross correlation for $\tau = 0$. A limitation when using the Pearson correlation coefficient is that it only detects linear correlations. If the data has a clear non-linear geometric trend the Pearson formula will not recognize it.

4.7 Power Spectral Density

The power spectral density describes average power as a function of frequency. It can be calculated by taking the Fourier transform of the autocorrelation from a second order stationary signal [87]. The Fourier transform can be written in a discrete and a continuous form respectively,

$$
\begin{aligned}
S_{XX}(\omega) &= \sum_{m=-\infty}^{+\infty} R_{XX}(m) exp(-j\omega m) \\
S_{XX}(f) &= \int_{-\infty}^{+\infty} R_{XX}(\tau) exp(-jf\tau) dt.
\end{aligned}
\tag{4.26}
$$

In the equation above ω and f is the frequency, R_{XX} is the autocorrelation and S_{XX} is the power spectral density. In this thesis the power spectral density will be estimated by Barlett's procedure, which is a special case of the periodogram [87]. The periodogram is the Fourier transform of the estimated autocorrelation given by,

$$
\hat{S}_{XX}(\omega) = \sum_{m=-\infty}^{+\infty} \hat{R}_{XX}(m) \exp(-j\omega m). \tag{4.27}
$$

It can be shown that the variance properties of the periodogram equation (4.27) is as large as the power specter itself [87]. Barlett invented a method where the signal is split up into K windows, without overlap between windows. The periodogram is calculated for each window and averaged. Thus the variance of the final power specter will decrease as one over K.

The relationship between power specter and Hurst exponent for a fGn can be found by the continuous Fourier transform of the autocorrelation function in equation (4.16) [71],

$$
\begin{aligned}
S(f) &= \int_{-\infty}^{\infty} \rho(t) \exp(-2\pi i f t) dt \\
&= 2H(2H-1)E[X(1)^2] \int_{-\infty}^{\infty} t^{2H-2} \exp(-2\pi i f t) dt \\
&= 2H(2H-1)E[X(1)^2] \int_{-\infty}^{\infty} \left(\frac{\epsilon}{f}\right)^{2H-2} \exp(-2\pi i \epsilon) \frac{d\epsilon}{f} \\
&= 2H(2H-1)E[X(1)^2] \int_{-\infty}^{\infty} \epsilon^{2H-2} \exp(-2\pi i \epsilon) d\epsilon f^{1-2H} \\
&= 2H(2H-1)E[X(1)^2] C f^{1-2H} \\
&\propto f^{1-2H}
\end{aligned}
\tag{4.28}
$$

Where a variable change $\epsilon = ft$ has been used and C is the integral,

$$
C = \int_{-\infty}^{\infty} \epsilon^{2H-2} \exp(-2\pi i \epsilon) d\epsilon. \tag{4.29}
$$

Thus the power spectral density follows a power law for a fGn. A more common way of expressing the power specter is [57],

$$S(f) \propto f^{-\beta}. \tag{4.30}$$

Where $\beta = 2H - 1$ for a fGn and $\beta = 2H + 1$ for a fBm. Since the Hurst exponent varies between $0 < H < 1$ a value of $-1 < \beta < 1$ represents a fGn while a fBm has β values $1 < \beta < 3$. Therefore the slope of the power specter can be used to verify whether the signal is a fBm or fGn.

4.8 Rescaled Range

The long range correlations in a signal can be found by looking at the variability in a signal, or more formally the range. This concept becomes clear when looking at realizations of fBms for different Hurst exponents as presented in figure 4.3. The method of rescaled range consists of finding the range R between maximum and minimum in a subset of a cumulated noise. Dividing the subsets by their standard deviation removes the influence of heavy tails if the process does not have Gaussian amplitude distribution. The idea behind rescaled range is that a persistent cumulated signal will have large peaks and low valleys, since a positive value has a larger probability for following a positive value and vice versa. The method for calculating the rescaled range is given below [57],

$$\begin{aligned}
Y(n) &= X(n) - \langle X \rangle, n = 1, 2, ..., N \\
Z(n) &= \sum_{i=1}^{n} Y(i), n = 1, 2, ..., N \\
R(n) &= \max(Z(1), Z(2), ..., Z(n)) - \min(Z(1), Z(2), ..., Z(n)), n = 1, 2, ..., N \\
RR(n) &= \frac{R(n)}{S(n)}.
\end{aligned} \tag{4.31}$$

In the equation above $S(n)$ is the standard deviation for the series of n points, and $\langle X \rangle$ is the mean value of the fGn X. In addition to using the method above it is common to take the average over all the subsets with length n in the signal. In 1951 Harold E. Hurst gave an empirical relation where the total rescaled range could be written as a power law. The relation has since then been proven both mathematically [2] and found experimentally [59]. The exponent was named the Hurst exponent. For a fGn the power law relation can be written as,

$$RR(n) = Cn^{H}. \tag{4.32}$$

According to the equation above the Hurst exponent can be found by straight line regression in a logarithmic plot of RR versus the subset size n.

4.9 Structure functions

The q-th order structure function S_q of a signal, X, can be defined as [95],

$$S_q(t,s) = \langle |X(t) - X(s)|^q \rangle . \tag{4.33}$$

For a fBm the equation above can be reduced to,

$$\begin{aligned} S_q(t,s) &= \langle |X(t) - X(s)|^q \rangle , \\ &= \langle |X(t-s)|^q \rangle , \\ &= \langle |X(\tau)|^q \rangle , \\ &= \left\langle |\tau^{qH}||X(1)|^q \right\rangle , \\ &= \langle |X(1)|^q \rangle \, |\tau|^{qH}, \\ &= \langle |X(1)|^q \rangle \, |\tau|^{\zeta(q)}, \\ &= S_q(\tau), \\ &\propto |\tau|^{\zeta(q)}. \end{aligned} \tag{4.34}$$

From the equation above the structure functions follow a power law for all q's. The power law exponent can be calculated for different values of q and the Hurst exponent can be found from a linear fit of $\zeta(q)$ versus q. The sample structure functions can be estimated by [78],

$$\hat{S}_q(k) = \frac{1}{N-k} \sum_{i=1}^{N-k} |X(i+k) - X(i)|^q. \tag{4.35}$$

For a stationary signal such as a fGn, the equation above will return a constant value for all k's. Therefore the structure function analysis must be used on a non stationary signal such as an fBm or cumulated fGn, β values between 1 and 3. For a more thorough investigation of the structure function analysis used on plasma turbulence data see Yu [95].

4.10 Wavelet analysis

A widely used method for analyzing time series is the wavelet analysis introduced by Grossman and Morlet [41]. The wavelet method can be used on both non-periodic and non-stationary signals. The method describes how the frequencies vary with timescale. A thorough introduction to the wavelet analysis can be found in Farge [23]. The wavelet analysis is a convolution between a mother wavelet with a specific width and the signal itself. This can be seen as a filter,

$$W(t,a) = \frac{1}{a^{1/2}} \int_{-\infty}^{\infty} g\left(\frac{t'-t}{a}\right) f(t')dt', \tag{4.36}$$

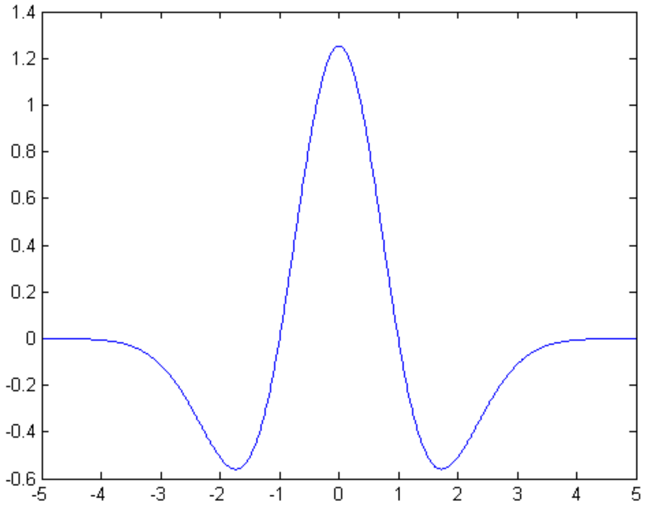

Figure 4.5 – The figure above describes the waveform of the Mexican hat wavelet.

The equation above returns a new transformed waveform W at time scale a. In the equation above g is the mother wavelet with a width proportional to the scaling constant a, f is the signal. The variance of the wavelet coefficients follow a power law similar to that of the power specter (4.30), [57, 88],

$$\begin{aligned} \text{fBm: } & \sigma_W^2 \propto a^{2H+1} \\ \text{fGn: } & \sigma_W^2 \propto a^{2H-1} \end{aligned} \tag{4.37}$$

The wavelet analysis can also be used to calculate at which timescales the signal is self-similar. Wavelet coefficients scales similar to the signal at different temporal scales. Thus self similarity can be verified by similar PDF of wavelet coefficients at different time scales [4, 10].

4.10.1 Mexican hat

The mother wavelet which will be used here is the Mexican hat. The Mexican hat is the negative of the second derivative of the Gaussian distribution function [57],

$$g(t) = \left(\frac{1}{2\pi}\right)^{1/2} (1 - t^2) e^{-(1/2)t^2}, \tag{4.38}$$

The Mexican hat waveform is pictured in figure 4.5.

4.11 Conditional window averaging

Conditional window averaging (CWA) is based on local maxima sampling. The method makes it possible to separate events in a signal and analyze them separately. Every time a threshold condition is met in the signal the local waveform is sampled, all such waveforms in a signal is averaged to give a conditionally averaged waveform [96, 97],

$$\Phi_C(\tau) = \langle \Phi(t)|C \rangle . \tag{4.39}$$

In the equation above Φ_C is the conditionally averaged waveform, Φ is the signal and C is the condition. In this thesis the condition will be an amplitude value as a function of the standard deviation. By doing the CWA information about the amplitude of events, duration of events and time between events can be sampled simultaneously. This new information can then be used to characterize the statistics of the events. Two different methods will be used to calculate the CWA. The first method does not allow overlap by removing every waveform after it has been collected, this is the one which will be used in statistically independent events. The other method collects all events, even overlapping ones, thus the result may include dependencies. It should be mentioned that even though the last method allows overlap every event is not sampled. Overlapping events overlapping above the threshold will still be one event. Thus the two methods will in most cases return very similar results for waiting time and amplitude distributions.

4.11.1 Conditional variance

A way to analyze the reproducibility of a waveform is the conditional variance method used in Øynes et al [96, 97]. Conditional variance is calculated by,

$$V_{con}(t) = \frac{\left\langle (\Phi(t) - \Phi_C(\tau))^2 | C \right\rangle}{\langle (\Phi(t)|C)^2 \rangle}, \tag{4.40}$$

The conditional variance V_{con} takes on values between 0 and 1, where 1 represents no reproducibility and 0 represents high degree of reproducibility. It is common to present the reproducibility as $r = 1 - V_{con}$. A high degree of reproducibility means that similar waveforms are found throughout the signal.

4.11.2 Duration, waiting time and quiet time

When sampling the conditional waveforms, information about waiting time, burst duration and quiet times are sampled simultaneously. The waiting time is defined as the time between two subsequent bursts, while quiet time is the time under the threshold between to subsequent burst. The burst duration is defined as the time of a single burst above the threshold. The

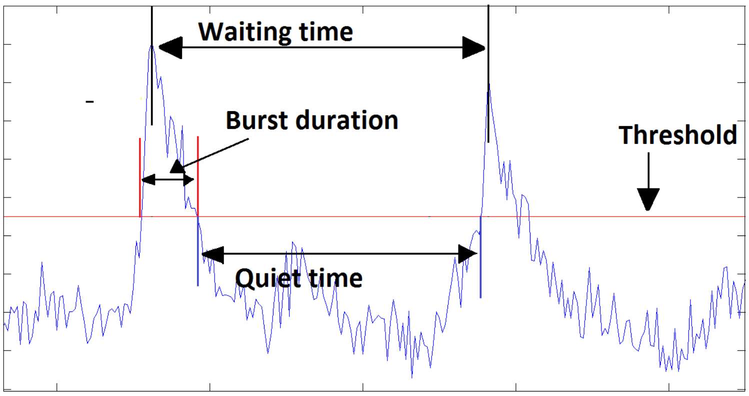

Figure 4.6 – The figure shows a signal with two high amplitude events. The horizontal line is the threshold. The time an event is over the threshold is called the burst duration. The time between events under the thresholds is called quiet time. The time between to local maximas over the threshold is called waiting time.

times are visualized in figure 4.6. For the data analyzed in this thesis the burst duration are usually much smaller than the waiting time, thus quiet times and waiting times are approximately equal. The duration by this method is highly dependent on the amplitude. Therefore the average burst duration will be found by the conditionally averaged waveform instead.

4.12 Self-organized criticality

Self-organized criticality (SOC) is a method first explained by the danish scientist Bak [5]. In this theory Bak tries to explain the theory behind the random motions of a sand pile with the use of SOC. The theory begins with considering a sand pile where you add grains of sand, if a column of grains reach a critical amount, a dispersion will occur where one grain is given to each neighbor. Such a dispersion could lead to other dispersions and also larger avalanches. The way this system sets it self up in a critical state is why it is called self-organized. So why is this important in plasma fusion? Researchers has come up with theories which show that the turbulent eddies in the edge region of a fusion device can be seen as a SOC system [73, 80]. The system builds itself up towards a critical state where high density blob are the sandpile avalanches. To see if a system can be classified as a SOC process the system must exhibit long range correlations. Note that not all long range correlated systems are SOC processes.

Theory	PSD	RS	SF	Wav
0.50	0.50	0.53	0.50	0.50
0.60	0.61	0.62	0.60	0.61
0.70	0.72	0.71	0.68	0.70
0.80	0.82	0.81	0.80	0.81
0.90	0.91	0.91	0.88	0.94

Table 4.1 – In this table the Hurst exponent calculated with the different methods is compared to a theoretical value given in the left column.

	PSD	RS	SF	Wav
μ	0.72	0.71	0.69	0.70
σ	0.003	0.01	0.02	0.004

Table 4.2 – In this table the mean Hurst exponent and the standard deviation is calculated by the various methods for 50 runs with H = 0.7.

4.13 Comparison of statistical methods

In this section the statistical methods introduced in the previous sections will be compared on computer generated fGns. In addition the robustness of the methods regarding trends and amplitude magnification will be analyzed. The fGns are generated by the matlab code made by Stilian Stoev [89].

4.13.1 Analysis of fGn

In this first section the methods will be used on a signal without modifications with a given Hurst exponent, examples of fGn signals was given previously, see figure 4.4. The overall results for different Hurst exponents is given in table 4.1. Note that all methods estimate a Hurst exponent close to the theoretical value. The individual methods for a theoretical $H = 0.7$ is given in figure 4.7. In the figure the fit range for each method seems to be consistent. The bias and error of each method has been tested by 50 computer generated fGns with $H = 0.7$. The mean value and standard deviation of H is given in table 4.2. From the table it is clear that the best estimator is the wavelet analysis, the other methods might have a slight bias. In addition the error is a lot larger for the rescaled range and structure function analysis.

4.13.2 Trends

The data from Alcator C-Mod used later have some trends which needs to be removed before the signal can be analyzed. In this section a fGn with H = 0.7 will be added to a sinusoid and a linear function to see the effect of trends in the signal. In figure 4.8 a fGn with a linear trend is plotted, the trend

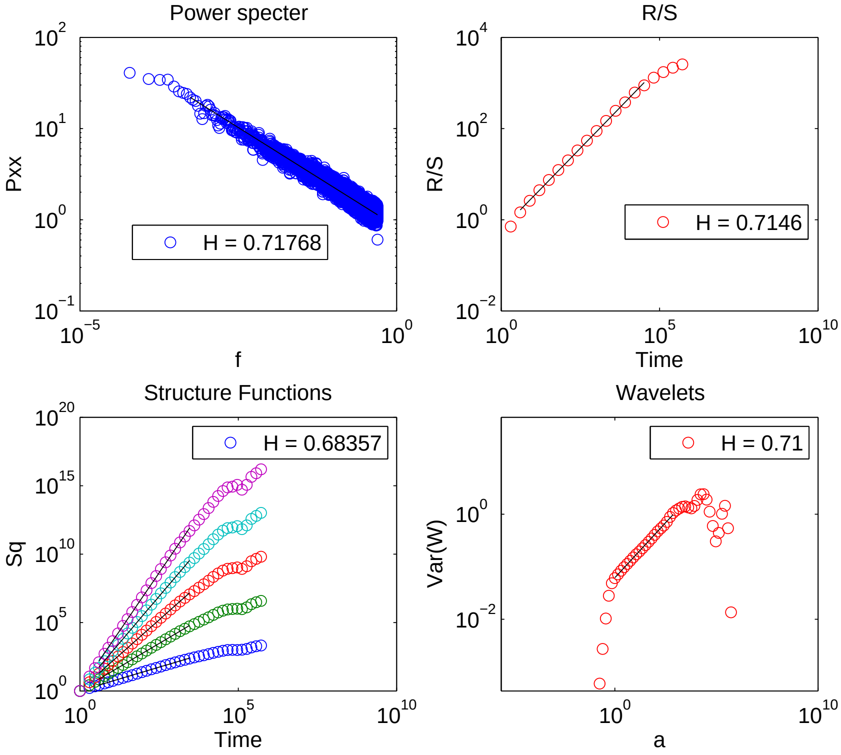

Figure 4.7 – In these figures the different methods for calculating the long range correlations is used and visualized. The data used has a theoretical $H = 0.7$. Upper left: The power specter. Upper right: The rescaled range. Lower left: The structure functions for q=1:5. Lower right: Variance of wavelet coefficient.

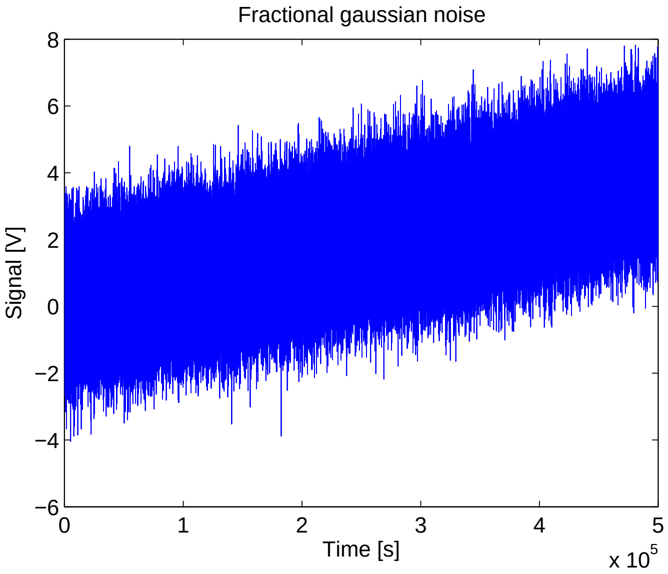

Figure 4.8 – Realization of a fGn with linear trend, $H = 0.7$. Both signals have the same standard deviation.

and the fGn has equal standard deviation. In table 4.3 the Hurst exponents calculated with various methods for a fGn with linear trend and theoretical value H = 0.7 is given. See that only the structure function method fails for a linear trend. The other methods only change shape for the highest time scales which are not used for fitting. The next step to analyze is a sinusoidal trend as pictured in figure 4.9, the trend and the fGn has equal standard deviation. From the table 4.4 it is seen that trends only effects structure function analysis. The period used for this trend is the length of the signal, thus the other methods slightly change shape for the largest time scales. It has been shown that a period within the fitting range changes the Hurst exponent for all methods. In addition an increased standard deviation of the trend effects the Hurst exponent. Thus one should remove large fast moving trends. In figure 4.10 the Hurst exponent estimated by structure function analysis is plotted as a function of the standard deviation of the trend σ_t divided by the standard deviation of the signal σ_s. In the figure it is clear that the structure function analysis is very sensitive when it comes to trends, a trend with $\sigma_t/\sigma_s = 0.1$ makes it impossible to recover the true Hurst exponent. Interesting to see that the evolution of H is the same for both linear and sinusoidal trends.

4.13.3 Amplitude variations

The experimental data collected from Alcator C-Mod shows some amplified parts compared to the overall signal. In this section a generated fGn with an

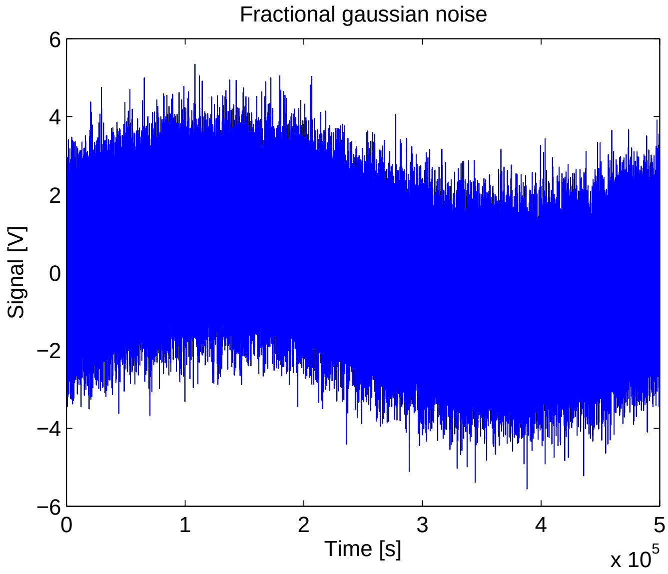

Figure 4.9 – Realization of a fGn with Hurst exponent 0.7 and a sinusoidal trend. The two signals have equal standard deviation, and the sinusoidal trend has a period equal to the length of the fGn

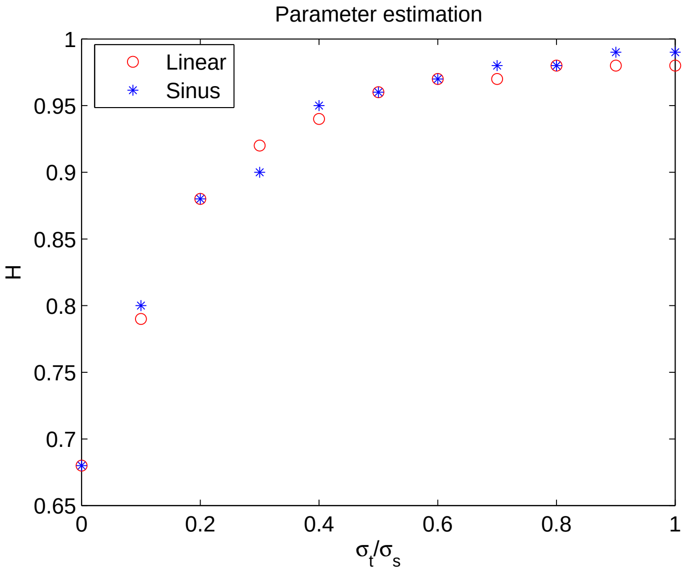

Figure 4.10 – In the figure the Hurst exponent for a signal with trend linear and sinusoidal trend is plotted as a function of the standard deviation of the trend divided by the standard deviation of the signal.

Theory	PSD	RS	SF	Wav
0.70	0.72	0.72	0.98	0.71

Table 4.3 – In this table the Hurst exponent calculated for a fGn with a linear trend is listed. Both signals have the same standard deviation.

Theory	PSD	RS	SF	Wav
0.70	0.72	0.71	0.96	0.71

Table 4.4 – In this table the Hurst exponent calculated for a fGn with a sinusoidal trend is listed. The fGn has a theoretical value 0.70 and both signals have the same standard deviation. The period of the sinusoidal trend is equal to the signal length of the fGn.

increased amplitude part is used, see figure 4.11. Fortunately it is seen from table 4.5 that having a magnified part does not effect the results. This is fortunate because to decide which part is magnified is usually more difficult than removing a trend in the signal. This is also as expected since the RR analysis is averaged over all subsets in the signal.

Theory	PSD	RS	SF	Wav
0.70	0.72	0.72	0.70	0.71

Table 4.5 – In this table the Hurst exponent calculated for a fGn with magnified part is listed. See that the amplification does not have any noteworthy effect.

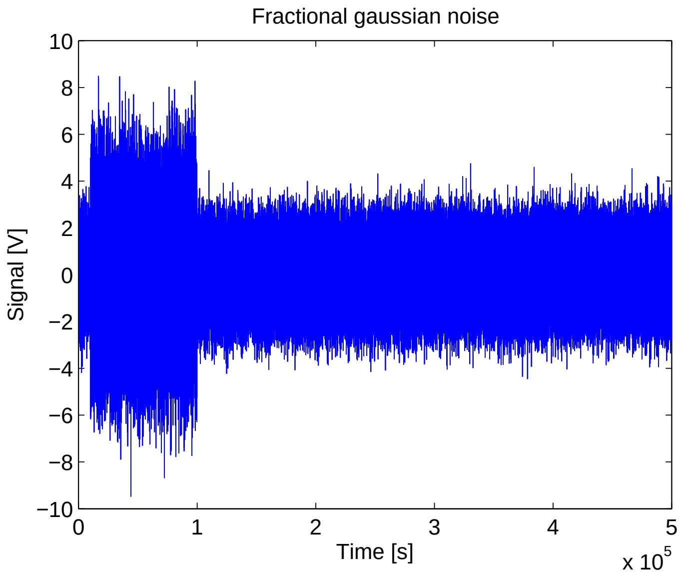

Figure 4.11 – Realization of a fGn with Hurst exponent 0.7 and a part with increased amplitude.

Chapter 5

Stochastic Model

In this chapter a stochastic model describing the high density events in the SOL will be proposed. The model follows Garcia [28] closely, but with a slightly modified waveform. The model is based on experimental measurements which will be verified later.

5.1 Plasma Fluctuations Model

Recent experiments have shown that particle density measured in the SOL of tokamak plasmas can be seen as a random sequence of burst events [29]. It is then reasonable to assume that the signal can be written as a superposition of the individual burst events,

$$\Phi(t) = \sum_{k} A_k \psi(t - t_k). \tag{5.1}$$

Where A_k is the amplitude of the k-th burst, ψ is the burst waveform and t_k is time of event k. The waveform consist of a exponential rise and an exponential decay. This particular waveform is common in blob dominated plasma regions [8, 29]. In this thesis Alcator C-Mod measurements in the SOL will prove to exhibit the same type of waveform, see figure 6.24. The waveform can be written as,

$$\psi(t) = \begin{cases} \exp\left(\frac{t}{\tau_r}\right) t < 0 \\ \exp\left(-\frac{t}{\tau_d}\right) t > 0 \end{cases} \tag{5.2}$$

The number of events K during time t is assumed to be a Poisson process with distribution [75],

$$P(K) = \exp\left(-\frac{t}{\tau_w}\right)\left(\frac{t}{\tau_w}\right)^K \frac{1}{K!}. \tag{5.3}$$

In the equation above τ_w is the average waiting time. The waiting times in a Poisson process are exponentially distributed with mean value τ_w, the relation is derived in the appendix, see also Ross [75],

$$f_\mathcal{T}(x) = \frac{1}{\tau_w} \exp\left(-\frac{x}{\tau_w}\right), \tau > 0. \tag{5.4}$$

In the equation above the waiting times are defined by $\tau = t_{n+1} - t_n$. The amplitudes A are assumed to be exponentially distributed,

$$f_A(x) = \frac{1}{\langle A \rangle} \exp\left(-\frac{x}{\langle A \rangle}\right), x > 0. \tag{5.5}$$

In the equation above $\langle A \rangle$ is the mean value of A. The signal in equation (5.1) is then a sum over exponential distributed random variables times a constant waveform. The sum over n independent exponential random variables follow a gamma distribution, a proof is given in the appendix [75],

$$f_\Phi(x) = \frac{1}{\theta^k} \frac{1}{\Gamma(k)} x^{k-1} \exp(-x/\theta). \tag{5.6}$$

Where Γ is the gamma function,

$$\Gamma(\alpha) = \int_0^\infty t^{\alpha-1} e^{-t} dt. \tag{5.7}$$

The parameters k and θ are respectively called the shape and scale parameter defined as,

$$\theta = \frac{\left\langle (\Phi - \langle \Phi \rangle)^2 \right\rangle}{\langle \Phi \rangle}, \quad k = \frac{\langle \Phi \rangle^2}{\left\langle (\Phi - \langle \Phi \rangle)^2 \right\rangle}. \tag{5.8}$$

The moments of the shot noise model is calculated in the appendix and follows Pecseli [66],

$$\begin{aligned}
\left\langle \Phi^1(t) \right\rangle &= \langle A \rangle^1 \gamma, \\
\left\langle \Phi^2(t) \right\rangle &= \langle A \rangle^2 \left(\gamma + \gamma^2\right), \\
\left\langle \Phi^3(t) \right\rangle &= \langle A \rangle^3 \left(2\gamma + 3\gamma^2 + \gamma^3\right), \\
\left\langle \Phi^4(t) \right\rangle &= \langle A \rangle^4 \left(6\gamma + 11\gamma^2 + 6\gamma^3 + \gamma^4\right).
\end{aligned} \tag{5.9}$$

Where γ is given by,

$$\gamma = \frac{\tau_r + \tau_d}{\tau_w}. \tag{5.10}$$

In the equation above $\tau_r + \tau_d$ is the time before the waveform has decreased by e^{-1}, this can be seen as the duration. The shape and scale parameter governing the gamma distributed shot noise process can be written as,

$$\begin{aligned} \theta &= \frac{\left\langle (\Phi - \langle \Phi \rangle)^2 \right\rangle}{\langle \Phi \rangle} = \frac{\langle A \rangle^2 \gamma}{\langle A \rangle \gamma} = \langle A \rangle , \\ k &= \frac{\langle \Phi \rangle^2}{\left\langle (\Phi - \langle \Phi \rangle)^2 \right\rangle} = \frac{\langle A \rangle^2 \gamma^2}{\langle A \rangle^2 \gamma} = \gamma. \end{aligned} \tag{5.11}$$

From the moments above the normalized standard deviation, skewness and kurtosis of the shot noise model can be found by,

$$\begin{aligned} C &= \frac{\langle (\Phi - \langle \Phi \rangle)^2 \rangle^{1/2}}{\langle \Phi \rangle} = \frac{\langle A \rangle \gamma^{1/2}}{\langle A \rangle \gamma} = \gamma^{-1/2}, \\ S &= \frac{\langle (\Phi - \langle \Phi \rangle)^3 \rangle}{\langle (\Phi - \langle \Phi \rangle)^2 \rangle^{3/2}} = \frac{2 \langle A \rangle^3 \gamma}{\langle A \rangle^3 \gamma^{3/2}} = 2\gamma^{-1/2}, \\ K &= \frac{\langle (\Phi - \langle \Phi \rangle)^4 \rangle}{\langle (\Phi - \langle \Phi \rangle)^2 \rangle^2} = \frac{\langle A \rangle^4 (3\gamma^2 + 6\gamma)}{\langle 4 \rangle^4 \gamma^2} = 3 + 6\gamma^{-1}. \end{aligned} \tag{5.12}$$

The equations above can be used to find relations between the different moments,

$$\begin{aligned} K &= 3 + \frac{3}{2} S^2, \\ K &= 3 + 6C^2, \\ S &= 2C. \end{aligned} \tag{5.13}$$

Between skewness and kurtosis there exists a parabolic relation as seen before in [6,83]. The model also predicts a parabolic relation between kurtosis and variance, and a linear relation between skewness and variance. These relations can be used on experimental data to verify the model.

Part II

Results

Chapter 6

GPI measurements

In this chapter the results of the GPI measurements will be presented. The chapter will start out with a presentation of the signals and their statistical properties. At the end of the chapter the long range correlations will be analyzed together with blob properties such as speed and size. In the first part the analysis will focus on changes with major radius, changes with vertical position will be done towards the end of the chapter. The signals consist of 90 pixels collected at four different line-averaged densities, see table 6.1. The data analyzed is collected at $I_p = 0.8\,\mathrm{MA}$, $B = 4.0\,\mathrm{T}$ and if not stated otherwise $Z = -2.99\,\mathrm{cm}$, where $Z = 0$ represents the midplane. For more information about the data and the data acquisition see the theory part. To increase the length of the data time series, signals with equal line-averaged densities will be combined, providing a signal length of $0.5\,\mathrm{s}$. All signals have been detrended to remove non-stationarity in the measurements. In addition most of the analysis will be done on standardized signals,

$$X_{stand} = \frac{X - \mu_X}{\sigma_X} \tag{6.1}$$

A standardized signal has mean zero and standard deviation one.

Shot no.	n_e/n_G
1100803005	0.15
1100803006	0.15
1100803008	0.20
1100803009	0.20
1100803011	0.25
1100803012	0.25
1100803020	0.30

Table 6.1 – In this table the line-averaged density for each shot used is listed.

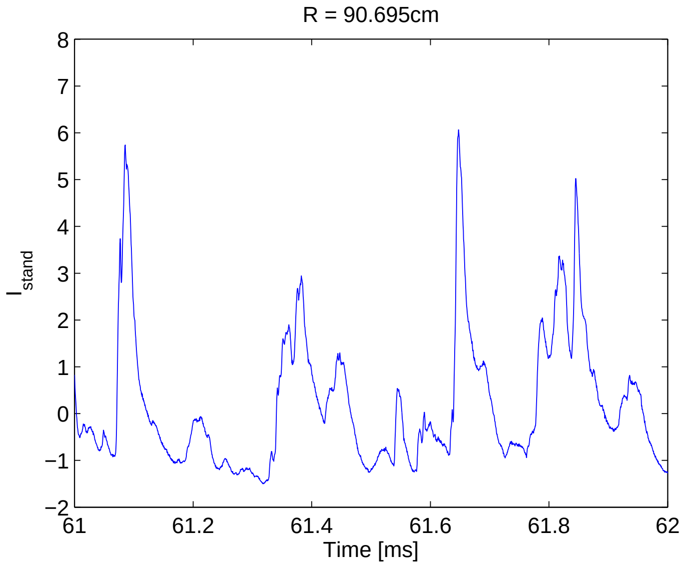

Figure 6.1 – In this figure 1 ms of a signal located in the SOL with $R = 90.70\,\text{cm}$, $Z = -2.99\,\text{cm}$ and $n_e/n_G = 0.25$ is plotted as a function of time.

6.1 GPI measurements, Raw time series

In this section the measured signals will be presented. In the radial direction the GPI data have 9 measurements, 4 in the scrape-off layer (SOL), $R = 89.93 - 91.08\,\text{cm}$, one at the separatrix, $R = 89.54\,\text{cm}$, and 4 measurements in the edge region, $R = 89.16 - 88\,\text{cm}$. In figures 6.1, 6.2 and 6.3 1 ms of the measured signals are plotted for three different radial positions. The signals used are standardized with $n_e/n_G = 0.25$ and located at Z = -2.99 cm. In order to emphasize the difference between the signals, the same range is used for the axis. The first figure, figure 6.1, shows a measurement from the SOL, $R = 90.70\,\text{cm}$. The signal seems to be composed of bursts with a characteristic waveform. The waveform has a sharp rise and a trailing wake as usually measured in the SOL of magnetically confined plasmas [28, 39, 76]. The second figure 6.2 is from a signal measured at the separatrix, $R = 89.54\,\text{cm}$. The relative fluctuations at the separatrix seems to be smaller than in the SOL. No clear universal waveform can be seen from the figure. The last figure 6.3 is from a signal measured in the edge region, $R = 88.77\,\text{cm}$. In the edge region the relative fluctuations are of the same order as at the separatrix and no clear waveform can be seen here either.

In figure 6.4 the full standardized signals have been plotted. In the figure the separatrix (blue) and edge (black) measurements have been shifted by respectively 10 and 20 [V]. In the SOL the signal has a burst-like shape with only positive amplitude peaks. In the edge region and at the separa-

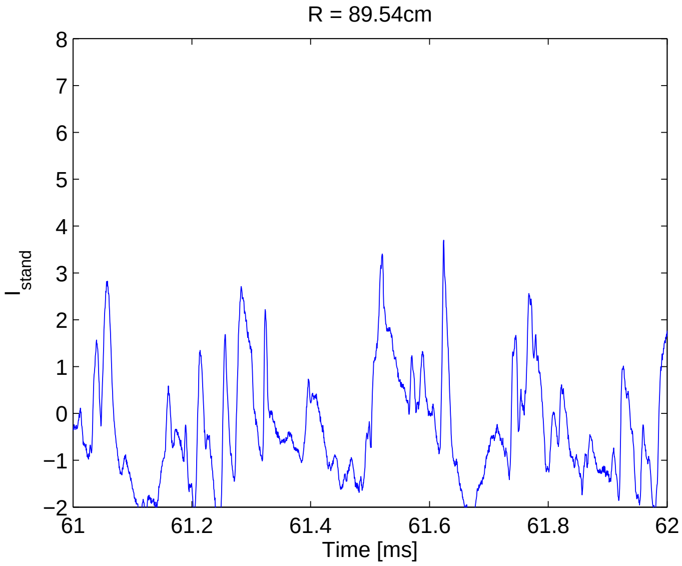

Figure 6.2 – In this figure 1 ms of a signal located at the separatrix with $R = 89.54\,\mathrm{cm}$, $Z = -2.99\,\mathrm{cm}$ and $n_e/n_G = 0.25$ is plotted as a function of time.

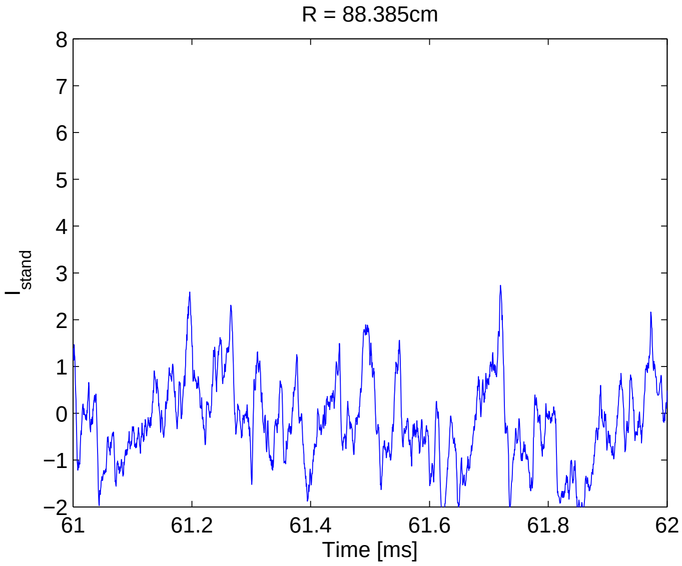

Figure 6.3 – In this figure 1 ms of a signal located in the edge region with $R = 88.385\,\mathrm{cm}$, $Z = -2.99\,\mathrm{cm}$ and $n_e/n_G = 0.25$ is plotted as a function of time.

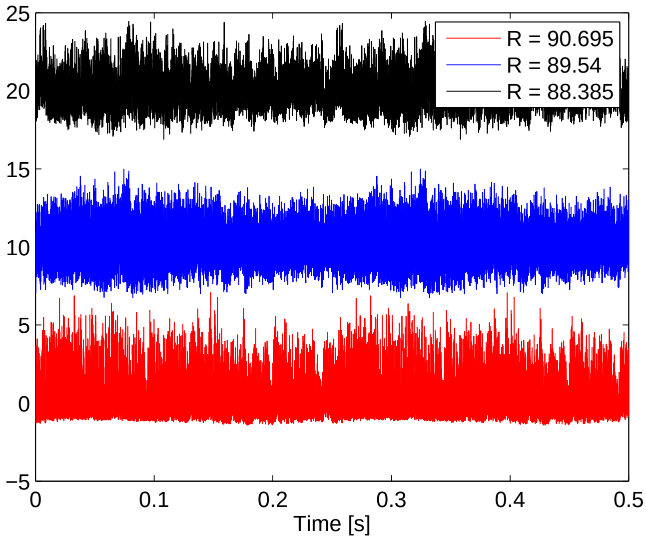

Figure 6.4 – In this figure three signals located at three different radial positions in the fusion reactor is plotted. The red signal is $R = 90.70\,\text{cm}$, the blue signal is $R = 89.54\,\text{cm}$ and the black signal is $R = 88.385\,\text{cm}$. All three signals are located at $Z = -2.99\,\text{cm}$ with $n_e/n_G = 0.25$.

trix the signals seem to have as many positive amplitude peaks as negative ones. Thus due to symmetry a normal distribution could be possible in the edge region and at the separatrix, this will be investigated later. For the SOL region the distribution is expected to have heavy tails towards positive values due to the bursts.

6.2 Statistical properties

In this section the basic statistical properties of the signals will be analyzed for all radial positions and line-averaged densities. In particular the mean and the second, third and fourth order central moments will be estimated. In figure 6.5 the mean value of the signal is plotted for several different line-averaged densities. From the figure it appears that the mean value increase out of the SOL and into the edge region where it drops off. A reason for this shape of the mean value is the diagnostics. In the SOL the plasma is relatively cold which gives low mean intensities. The intensity drop in the edge region is because the amount of neutral gas decreases as the temperature increase since more of the gas becomes ionized [34]. The mean value increase with line-averaged density in the SOL, while the opposite result is seen in the edge region.

In figure 6.6 the standard deviation divided by the mean value is plotted,

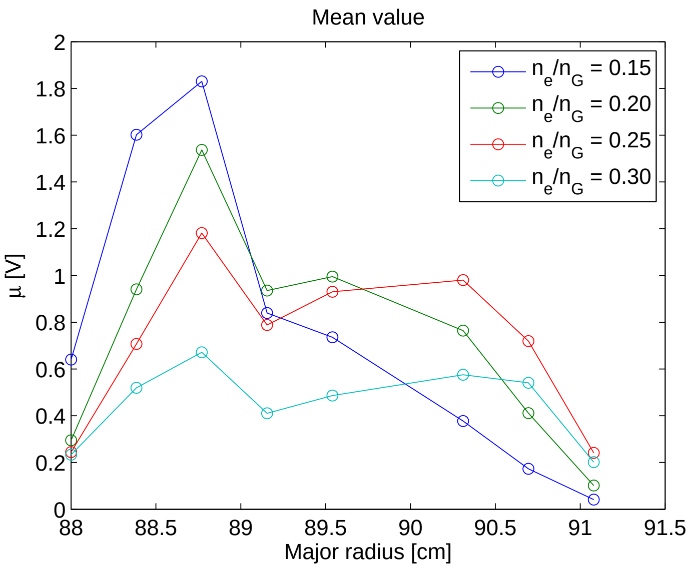

Figure 6.5 – In this figure the mean value of the signals are plotted as a function of major radius and line-averaged density at $Z = -2.99\,\mathrm{cm}$.

this relation can be interpreted as relative fluctuations. The relative fluctuations are small and constant in the edge region. In the SOL there is a sharp increase both with major radius and decreasing line-averaged density. This is an indication of blob existence in the SOL and not in the edge region. By assuming signals described as the stochastic model this figure shows the inverse square root of the shape parameter for the gamma distribution,

$$k = \gamma = \frac{\mu^2}{\sigma^2}. \tag{6.2}$$

Thus the γ parameter decrease with increasing major radius and decreasing line-averaged density. By assuming constant waveforms in the SOL, an increase of γ means decreasing waiting time between events. Thus the waiting time increases with radius and decreasing line-averaged density. More blobs when there are more particles. It should be mentioned that the result found here is highly dependent on the mean value estimated in figure 6.5.

In figure 6.7 the variance divided by mean value is plotted as a function of major radius and line-averaged density at $Z = -2.99\,\mathrm{cm}$. The figure shows small constant values in the edge region and larger values increasing with line-averaged density in the SOL. For a signal defined by the stochastic model this relation can be viewed as the mean peak value of the individual events. The figure shows that the large amplitude events are located in the SOL. Again the result is highly dependent on the mean value in figure 6.5.

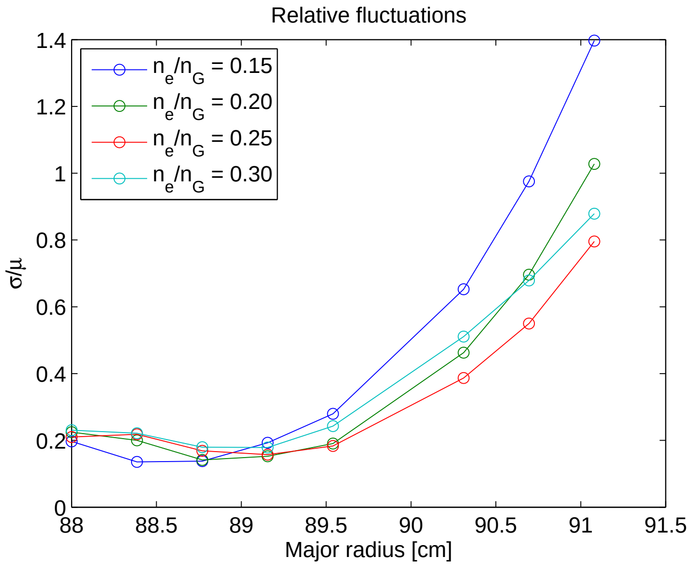

Figure 6.6 – The figure shows standard deviation divided by mean value for all radial positions and line-averaged densities at $Z = -2.99\,\mathrm{cm}$.

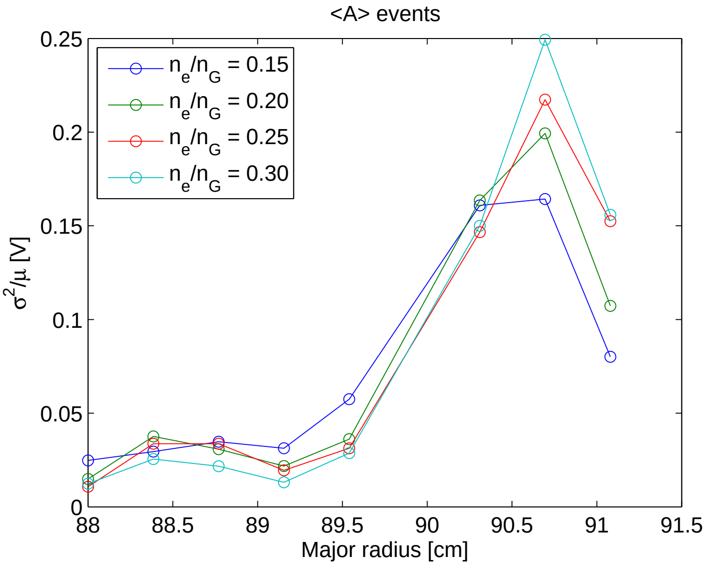

Figure 6.7 – In this figure the variance is divided by the mean value for all line-averaged densities and radii at $Z = -2.99\,\mathrm{cm}$. For a signal defined by the stochastic model this figure shows the mean amplitude of the events.

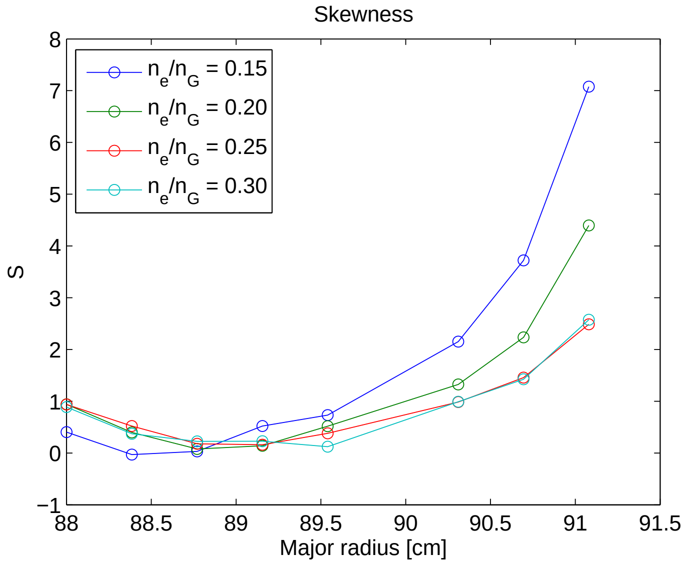

Figure 6.8 – The figure shows the skewness as a function of line-averaged density and major radius at $Z = -2.99\,\mathrm{cm}$.

The skewness of the signals are plotted as a function of major radius and line-averaged density in figure 6.8. In the SOL the skewness increase with major radius and decreasing line-averaged density. In the edge region the skewness is close to zero, which is the value for a Gaussian distribution. The positive skewness in the SOL is as expected from previous figures in this chapter. The signals in the SOL have much larger positive amplitudes than negative ones, thus positive skewness. A positive value of the skewness is a common indication of bursts in the signal. Negative values of the skewness indicate holes, which are negative bursts traveling in the opposite direction, see [8, 94]. For the data analyzed here evidence of holes are not found by skewness estimation.

In figure 6.9 the kurtosis is plotted as a function of line-averaged density and major radius at $Z = -2.99\,\mathrm{cm}$. For comparison a black line representing $K = 3$, which is the Gaussian value, has been inserted in the figure. Note that for the edge region most of the data are quite close to the Gaussian line. Since the skewness was close to zero, a Gaussian distribution seems like a good description for the distribution in the edge region. In the SOL the kurtosis increase with major radius and decreasing line-averaged density. The decrease of S and K with line-averaged density might indicate that blobs are less significant to the overall particle flux when the line-averaged density increases [3].

In Sanchez et al. [79] a method for measuring the magnitude of time asym-

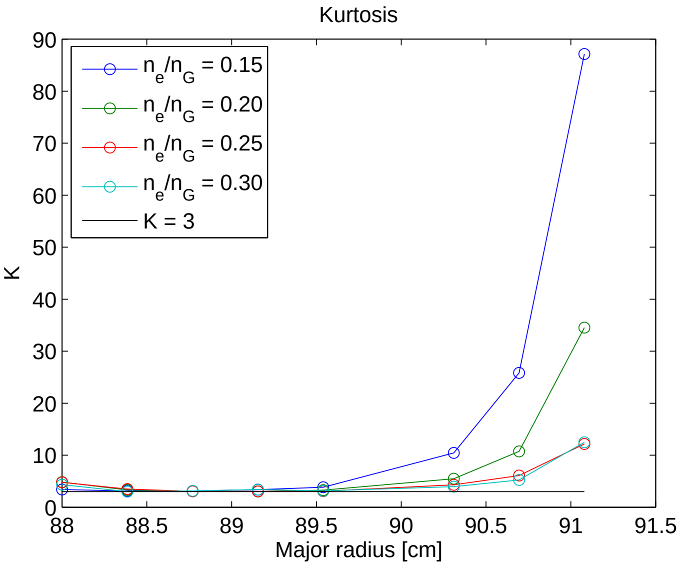

Figure 6.9 – The figure shows estimated kurtosis as a function major radius and line-averaged density at $Z = -2.99\,\mathrm{cm}$. The black line in the figure represent the Gaussian value K = 3.

metry in a signal is proposed. The method calculates the skewness of the time derivative of the signal. For a signal consisting of bursts with a sharp rise and a slow decay positive values is expected. A figure for the estimate of time derivate skewness is given in figure 6.10. From the figure it is seen that especially for the SOL the decay is slower than the rise, represented by a positive value. Going towards the edge region the skewness of the derivative decreases slowly towards zero, where rise and fall takes equal amounts of time. From the figure of time derivative skewness it is clear that even though the kurtosis and skewness seems to be more or less the same throughout the edge the signal does change. The result suggests that if there is a characteristic waveform, the waveform becomes more symmetric as the major radius decreases. The averaged waveform as a function of major radius will be analyzed in a later section.

6.2.1 Comparison with stochastic model

The stochastic model presented in the theory part is a way to describe the burst-like signal seen in the SOL with clearly defined statistical properties. The stochastic model will be tested by plotting the central moments versus each other. The relations provided by the stochastic model were derived in

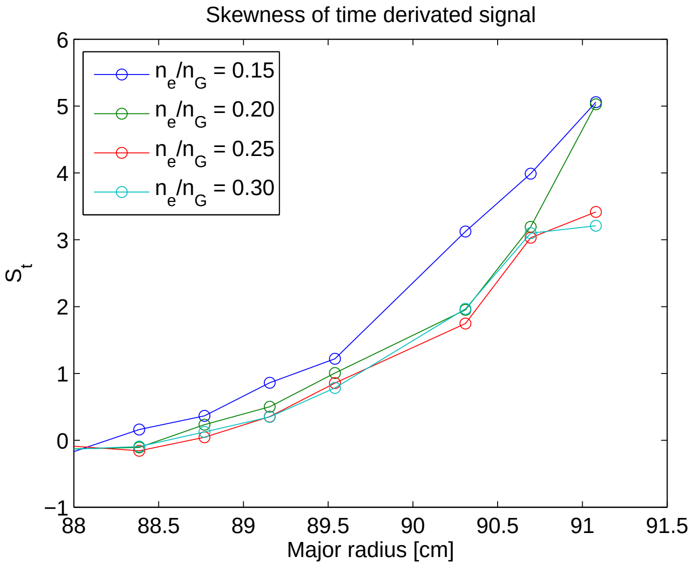

Figure 6.10 – The figure shows the estimated skewness of the time derivative of the signal. In the figure the colors represent different line-averaged densities and the x-axis is the major radius. All signals are measured at $Z = -2.99\,\text{cm}$.

the theory, the results are repeated here for convenience,

$$\begin{aligned} K &= 3 + \frac{3}{2}S^2, \\ K &= 3 + 6C^2, \\ S &= 2C. \end{aligned} \tag{6.3}$$

In the equation above C, S and K represents the normalized variance, skewness and kurtosis respectively. Between kurtosis and variance, skewness there is a parabolic relation and between skewness and variance there is a linear relation. In figure 6.11 the kurtosis is plotted as a function of skewness for SOL measurements. A parabolic line given by the stochastic model and two fitted lines with and without linear term have been inserted in the figure. The fit is found by the least squares method,

$$\epsilon = \sum_{i=1}^{N} \left(y_i - ax^2 - bx - c\right)^2. \tag{6.4}$$

Where a, b, c are constants found recursively by the values which gives the smallest possible ϵ. In the figure the relation between S and K seems to be a bit steeper than the relation provided by the stochastic model and has an offset value half of the stochastic model. It is obvious that the S/K relationship follows a parabolic relation, this has also been seen in other plasma devices [6, 39, 83].

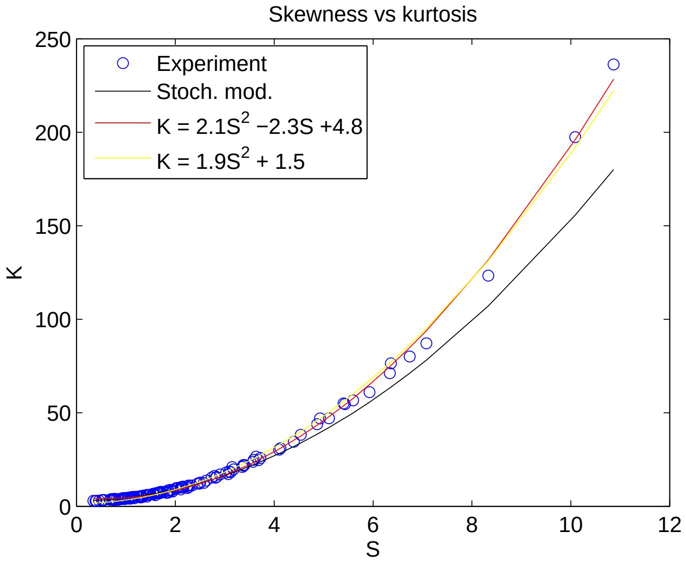

Figure 6.11 – In the figure skewness has been plotted versus kurtosis for signals with $n_e/n_G = 0.15 - 0.30$, $R = 91.08 - 89.93\,\mathrm{cm}$ and $Z = -4.51 - -1.08\,\mathrm{cm}$. Three lines have been fitted to the data, Stochastic model (black), parabolic relation with linear term (red) and parabolic relation without linear term (yellow).

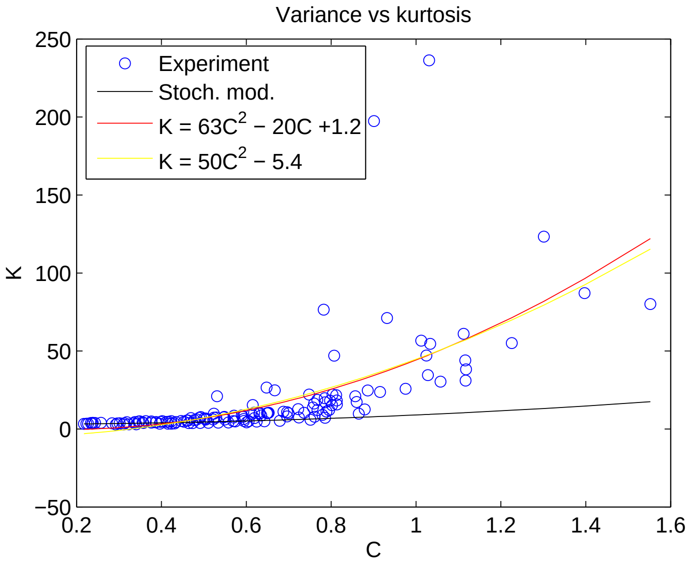

Figure 6.12 – In the figure the kurtosis has been plotted as a function of the normalized variance for signals with $n_e/n_G = 0.15 - 0.30$, $R = 91.08 - 89.93\,\mathrm{cm}$ and $Z = -4.51 - -1.08\,\mathrm{cm}$. Three lines have been fitted to the data, Stochastic model (black), parabolic relation with linear term (red) and parabolic relation without linear term (yellow).

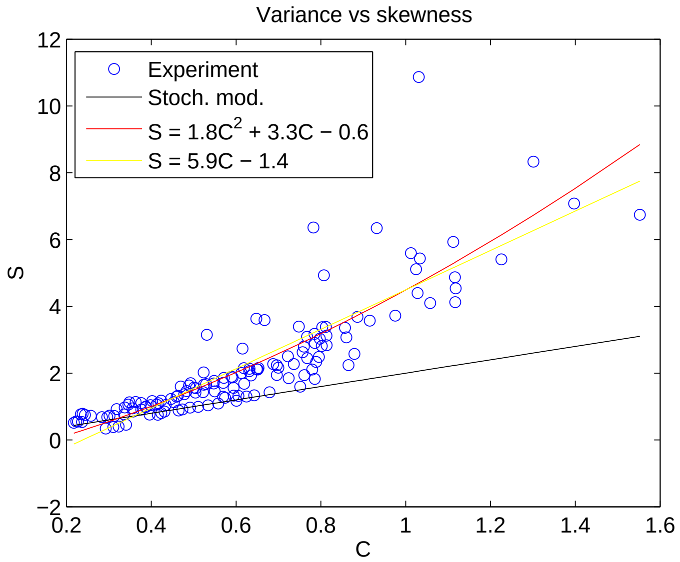

Figure 6.13 – In the figure the skewness has been plotted as a function of the normalized variance for signals with $n_e/n_G = 0.15 - 0.30$, $R = 91.08 - 89.93$ cm and $Z = -4.51 - -1.08$ cm. Three lines have been fitted to the data, Stochastic model (black), parabolic relation (red) and linear relation (yellow).

The kurtosis as a function of variance is plotted in figure 6.12. In this figure the data does not follow a curved relationship as in the previous figure. The black line represents the stochastic model and is a good fit for small values of C. For the larger values a fit has been used which is almost ten times steeper than the value provided by the stochastic model.

In figure 6.13 the skewness is plotted as a function of variance. As in the previous case the data shows an increasing spread with increasing C. The least squares fitted lines gives a better fit than the stochastic model, where the steepness is almost three times that of the stochastic model. The stochastic model seems to provide too moderate curves compared to the experimental results. The extreme values are possibly caused by the temperature dependence of the diagnostics described previously. For low values the stochastic model seems to provide a good fit.

6.3 Correlation

In this section the correlation of the standardized signals are analyzed. In figure 6.14 the autocorrelation for all radial positions with $n_e/n_G = 0.25$ and $Z = -2.99$ cm is plotted as a function of time. From the figure it is clear that in the edge region the signals are more strongly correlated than

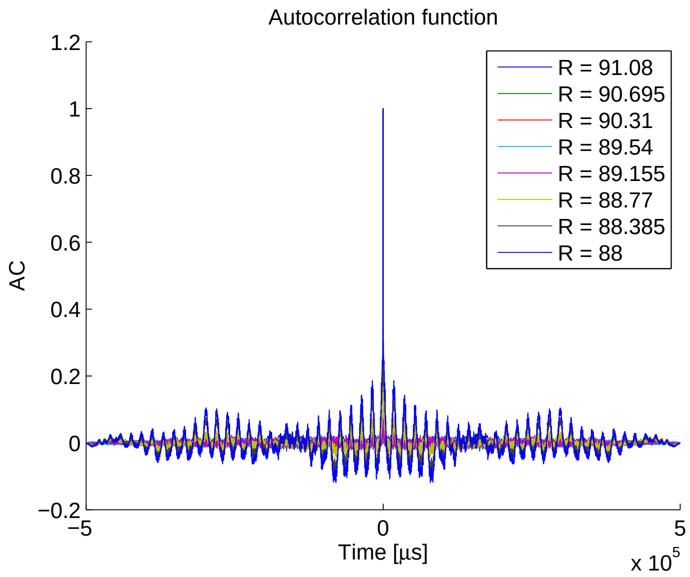

Figure 6.14 – In this figure the autocorrelation coefficients for all values of the major radius ($R = 91.08 - 88\,\mathrm{cm}$) are plotted for $n_e/n_G = 0.25$, $Z = -2.99\,\mathrm{cm}$.

in the SOL. In order to put a number on this result the autocorrelation is zoomed in for the first $50\,\mu s$ in figure 6.15. In the figure the black star lines are data from the edge region, the yellow star line is the point in the edge region closest to the separatrix. The red lines are SOL measurements and the square blue line is the separatrix. From the figure it is clear that in the edge region the autocorrelation has heavy tails compared to the separatrix and SOL autocorrelations. At the separatrix a clear difference is found from the edge region and SOL. This could have something to do with blob generation. Heavy tails could indicate long range correlations. Thus this result might indicate strong long range correlations in the edge region and medium/weak long range correlations in the SOL. The e-folding time scale τ_e is the scale at which the curves in figure 6.15 has decreased by one over e,

$$y = A\exp(-t/\tau_e). \tag{6.5}$$

A figure showing the e-folding times as a function major of radius and line-averaged density is given in figure 6.16. In the figure the e-folding time scale is found by an exponential fit to the exponential part of each curve in figure 6.15. It was previously shown that the autocorrelation should follow a power law, so the fit used here is quite poor. The fit range used is the first part of each curve except the first three points, thus the fit range increase with major radius. The calculations is merely for illustrative purposes to give an indication of how fast each curve falls off. The e-folding time scale increases slightly in the SOL with a slight decrease at the separatrix and first point in

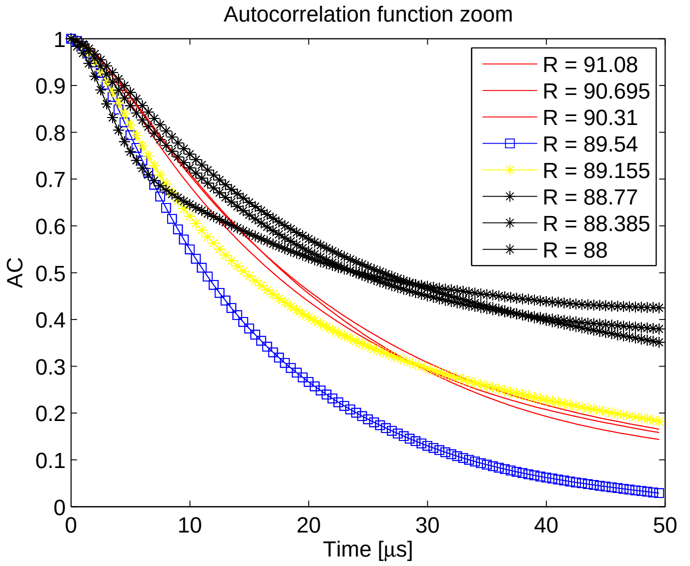

Figure 6.15 – This figure shows the autocorrelation for the first 50 μs for all values of the major radius ($R = 91.08 - 88$ cm) with $n_e/n_G = 0.25$ and $Z = -2.99$ cm.

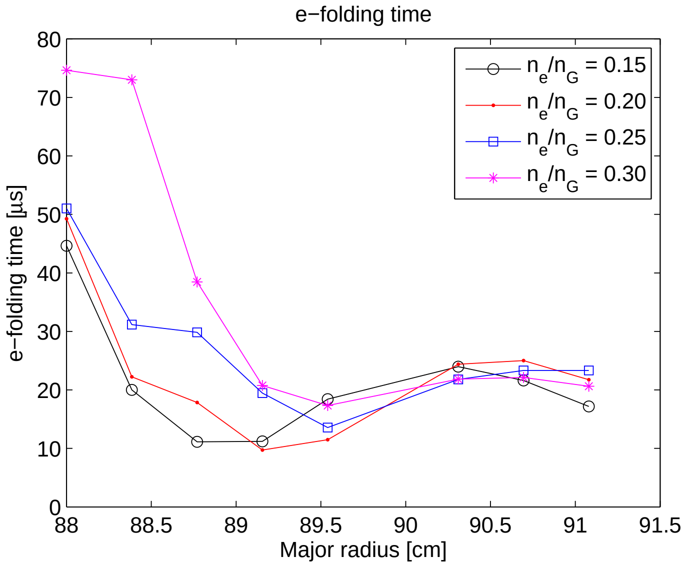

Figure 6.16 – This figure shows the e-folding time scale as a function of major radius for signals with $n_e/n_G = 0.25$ and $Z = -2.99$ cm. The e-folding time is calculated by an exponential fit to the exponential part of figure 6.15.

the edge region. In the edge region far away from the separatrix the e-folding time scale has a sharp increase. The position where the rise starts seems to depend on the line-averaged density, a larger line-averaged density gives a higher e-folding time in more of the edge region. These results suggest strong long range correlations in the innermost part of the edge region and possibly more of the edge region when the line-averaged density increases.

6.4 Distribution of signal amplitudes

Up to this point the signal has been analyzed by its moments and correlations, in this section the full amplitude distributions will be analyzed. From the previous plots of skewness and kurtosis it is clear that in the edge region the signals are close to Gaussian distributed with $S \approx 0$ and $K \approx 3$. In addition Gaussian distributed densities was found by Naulin et al. on drift wave turbulence simulations in the edge region [64]. In figure 6.17 the PDF of a signal in the edge region is plotted together with fitted lines representing the normal, Sattin and gamma distribution functions. The gamma distribution was introduced together with the stochastic model, equation 5.6. The Gaussian probability density function is defined as,

$$f_N(x) = \frac{1}{\sqrt{2\pi\sigma^2}} \exp\left[-\frac{(x-\mu)^2}{2\sigma^2}\right], \tag{6.6}$$

where the constants are,

$$\begin{aligned} \mu &= \langle x \rangle , \\ \sigma^2 &= \left\langle (x - \langle x \rangle)^2 \right\rangle . \end{aligned} \tag{6.7}$$

Sattin et al. has proposed a distribution which has provided a very good fit for several devices [81, 82]. The distribution is derived from the current continuity equation, see appendix equation (F.5),

$$F(n) = \frac{1}{\sqrt{2\pi\sigma^2}} \exp\left\{ -\frac{1}{2} \frac{\left[\ln\left(1 - \frac{(n/n_0)}{K}\right) - \mu\right]^2}{\sigma^2} \right\} \frac{1}{1 - \frac{\ln(n/n_0)}{K}} \frac{1}{n/n_0}, \tag{6.8}$$

where n_0, K, μ, and σ are free parameters. The signal used is located at $R = 88.350\,\text{cm}$, $Z = -2.99\,\text{cm}$ with line-averaged density $n_e/n_G = 0.25$. From the figure it is clear than even while the skewness and kurtosis are close to a normal distribution the normal distribution is not a particularly good fit. The gamma distribution seems to be a good fit as does the Sattin distribution. Slight deviation on the left side tail for the Sattin distribution is observed.

In figure 6.18 the PDF of a signal located in the SOL, $R = 90.70\,\text{cm}$, is

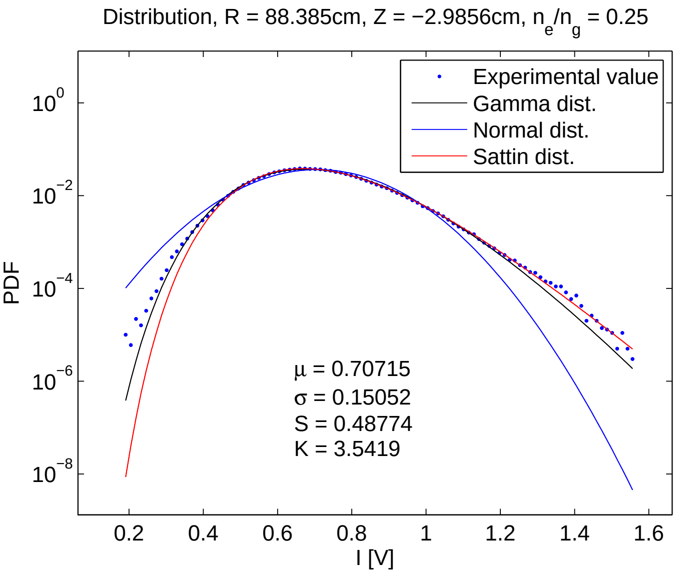

Figure 6.17 – The figure shows the estimated probability distribution function for a signal located in the edge region. The signal used has $R = 88.350\,\text{cm}$, $Z = -2.99\,\text{cm}$ and line-averaged density $n_e/n_G = 0.25$. In the figure three distribution functions have been fitted to the data, gamma distribution (black), normal distribution (blue) and Sattin distribution (red).

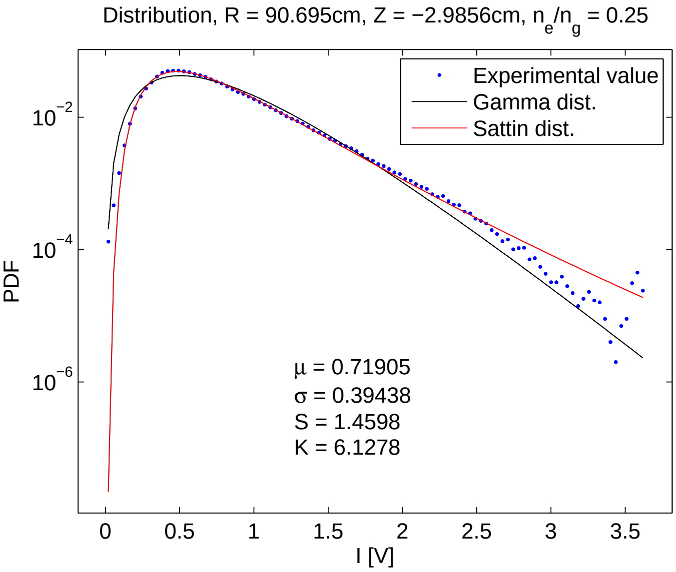

Figure 6.18 – The figure shows PDF of a signal located in the SOL, $R = 90.70\,\text{cm}$, $Z = -2.99\,\text{cm}$ and $n_e/n_G = 0.25$. The estimated values have been fitted by lines representing, gamma distribution (black) and Sattin distribution (red).

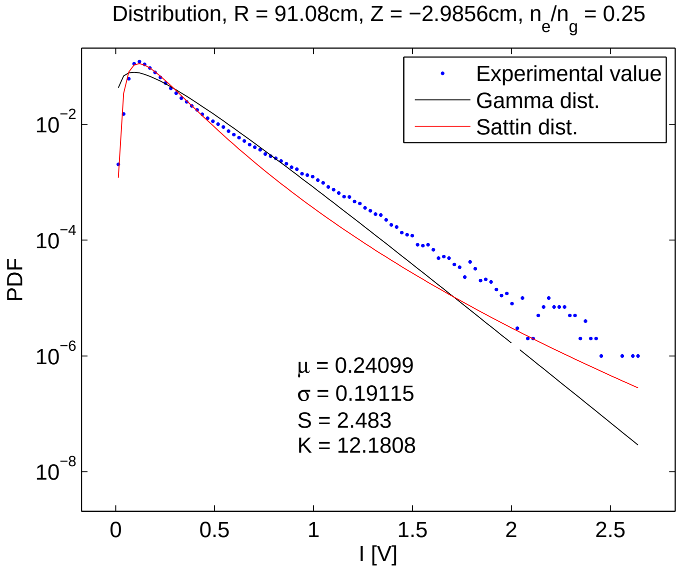

Figure 6.19 – The figure shows PDF of a signal located in the SOL, $R = 91.08\,\mathrm{cm}$, $Z = -2.99\,\mathrm{cm}$ and $n_e/n_G = 0.25$. The estimated values have been fitted by lines representing, gamma distribution (black) and Sattin distribution (red).

plotted with fitted distributions. The signal is located at $Z = -2.99\,\mathrm{cm}$ with $n_e/n_G = 0.25$. The distribution has long heavy tails which is a signature of a signal dominated by large amplitude bursts. Similar probability density functions have been found on many tokamak devices [1, 35]. For these measurements the Sattin distribution fail to fit the left side tails, but is a good fit for the peak and right side tail. The Gamma distribution shows a good fit for both the left and right side, but fails to fit the peak. The scaling and shape parameter can be calculated from the mean value and standard deviation as shown in the appendix. Thus $\theta = 0.21$ and $k = 3.41$. Now assuming that the signal is defined by the stochastic model $\gamma = 3.41$ and $\langle A \rangle = 0.21$.

From the figure of skewness and kurtosis given previously it is clear that the distribution function in the SOL varies with both position and line-averaged density. The distribution for a signal at the same vertical position and same line-averaged density at $R = 91.08\,\mathrm{cm}$ is given in figure 6.19. For these data the Sattin distribution is the best fit. The same calculations has been done on all radial positions for all line-averaged densities in the SOL, it was found that when the skewness is above approximately 3 none of the distributions fit the experimental values. Skewness between 2 and 3 gives a good fit for the Sattin distribution, while skewness between $1 - 2$ gives approximately equally good fit for the Gamma and Sattin distribution. When the skewness decreases even further ≈ 1 the Gamma distribution is the best fit. Thus in general a Sattin distribution is best for positions in the far SOL and small n_e/n_G, while a gamma distribution is best near the separatrix and large n_e/n_G. This is consistent with the previous results where the moments was plotted against each other and compared to the stochastic model. It should also be mentioned that a large error in the fit close to the walls are caused by the GPI diagnostics. Due to cold plasma near the wall there is reduced emission, as seen from the plot of mean value. High emission values can only be seen when there are high density blobs. This leads to increased skewness and kurtosis, higher than the values expected from the stochastic model.

6.5 Measure of intermittency/self-similarity

In this section the cumulated signal will be tested for self-similarity. Self-similarity was explained in the theory part and can be verified by similar distributions at different temporal scales. A simple way to do this is by using the wavelet coefficients. Since the wavelet coefficients have the same scaling properties as the signal, the PDF of the wavelet coefficients at different temporal scales can be used [1,4,10,23,56,81]. The analysis will be done on one signal in the SOL ($R = 90.70\,\mathrm{cm}$) and one signal in the edge region ($R = 88.350\,\mathrm{cm}$), the line-averaged density of both signals are $n_e/n_G = 0.25$ and $Z = -2.99\,\mathrm{cm}$. In figure 6.20 the PDF of wavelet coefficients in the SOL is plotted for different temporal scales. For the short time scales the distribution has a triangular shape gradually evolving to a bell shape when the time scale increases. For large time scales the PDF flattens out towards a straight line. Thus in general the signal is intermittent and not self-similar. In figure 6.21 the PDF of several time scales are plotted on top of each other. The figure shows PDFs for time scales from 128 to 8192 μs. The overlapping PDFs suggests a close to self-similar signal in this range.

Similar calculations has been done on a signal in the edge region, $R = 88.35\,\mathrm{cm}$, $Z = -2.99\,\mathrm{cm}$ and $n_e/n_G = 0.25$. The PDF for four different time scales is given in figure 6.22. In the edge region the PDF seems to have a more curved shape at smaller scales than for the SOL, could result in a self-similar signal at smaller scales. For the same time scales as for the signal in the SOL the edge region signal has a more spread PDF than for the SOL, see figure 6.23. This could indicate a slight deviation from self-similarity at larger scales in the edge region. The self-similar parts of the signals covers approximately two decades. Two decades means that the longest time scale divided by the shortest time scale is 10^2.

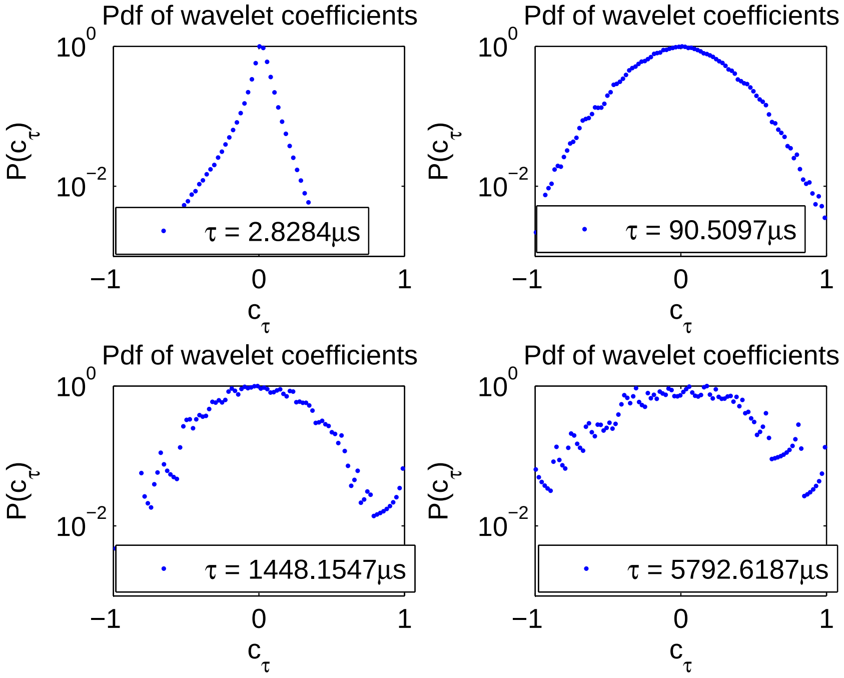

Figure 6.20 – In this figure the PDF of wavelet coefficients in the SOL is plotted for four different time scales. The signals analyzed is located in the SOL, $R = 90.70\,\mathrm{cm}$, $Z = -2.99\,\mathrm{cm}$ and $n_e/n_G = 0.25$.

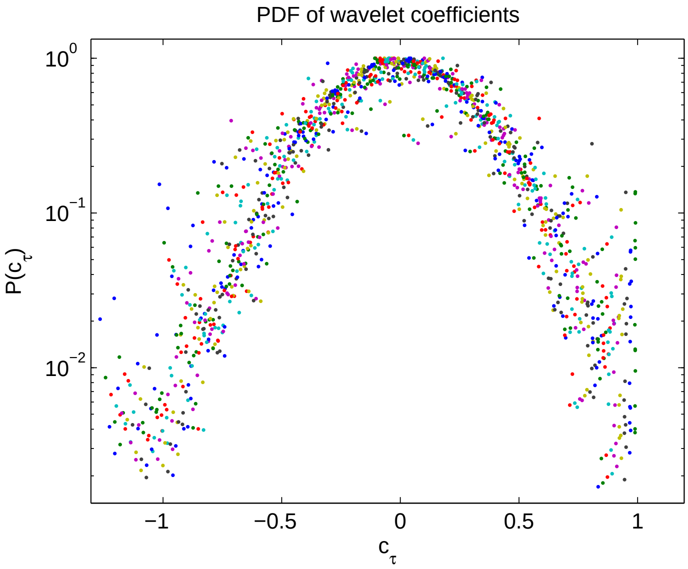

Figure 6.21 – The figure shows the PDF of wavelet coefficients in the SOL for time scales from 128 μs to 8192 μs plotted on top of each other. The signals analyzed is located in the SOL, $R = 90.70\,\text{cm}$, $Z = -2.99\,\text{cm}$ and $n_e/n_G = 0.25$.

6.6 Conditional window averaging

Here the large amplitude events will be analyzed by conditional averaging. The conditional averaging is done with a threshold of 2.5σ, where σ is the standard deviation of the signal. The signal considered, if not stated otherwise, is standardized and located in the SOL at $R = 90.70\,\text{cm}$, $Z = -2.99\,\text{cm}$ with line-averaged density $n_e/n_G = 0.25$. The conditionally averaged waveform is plotted in figure 6.24. The waveform has a fast rise and a slower decay. In the figure it is also given how many events the waveform is averaged over, 957. The waveform has been fitted by two exponentials, one with rise time τ_r and on with decay time τ_d, see the stochastic model. This waveform is consistent with blob formation found by previous experiments and simulations in the far SOL [8,30,36,76]. The average blob duration can be defined as the time it takes before the waveform has decreased by e^{-1}, $\tau_d + \tau_r = 21.5\,\mu$s.

In figure 6.25 the conditionally averaged waveform at a position in the edge region ($R = 88.39\,\text{cm}$) is plotted. The waveform looks like an inverted version of the waveform in the SOL, with a slow rise and a sharper decay. Exponential fits have been attempted on the curve, but not as successful as for the SOL data. Notice also that the number of events in the edge is halved compared to the SOL as should be expected from the signals pre-

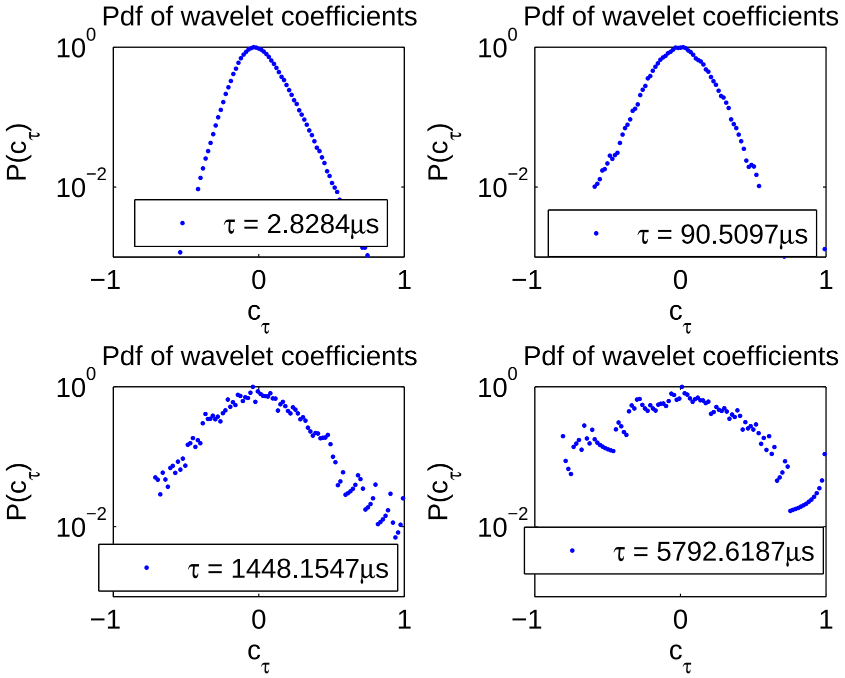

Figure 6.22 – In this figure the PDF of the wavelet coefficients at four different time scales is plotted for a signal at $R = 88.35\,\mathrm{cm}$, $Z = -2.99\,\mathrm{cm}$ with $n_e/n_G = 0.25$.

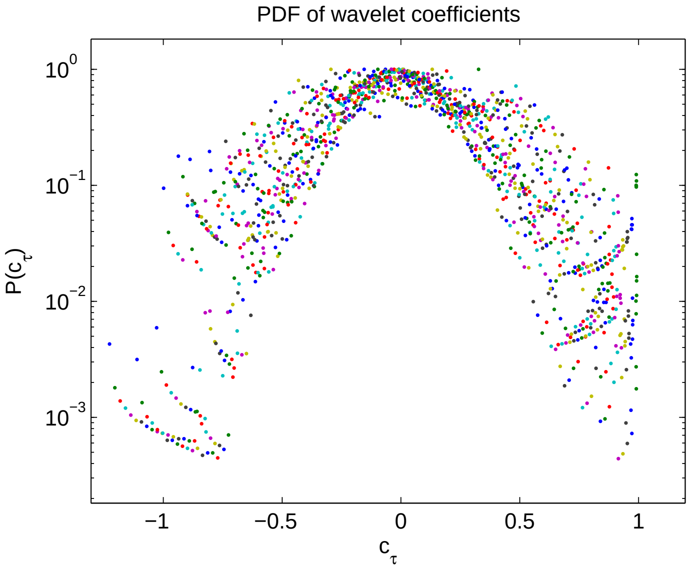

Figure 6.23 – In this figure the PDF of the wavelet coefficients with time scales in the interval $128 - 8192\,\mu\mathrm{s}$ is plotted for a signal at $R = 88.35\,\mathrm{cm}$, $Z = -2.99\,\mathrm{cm}$ with $n_e/n_G = 0.25$.

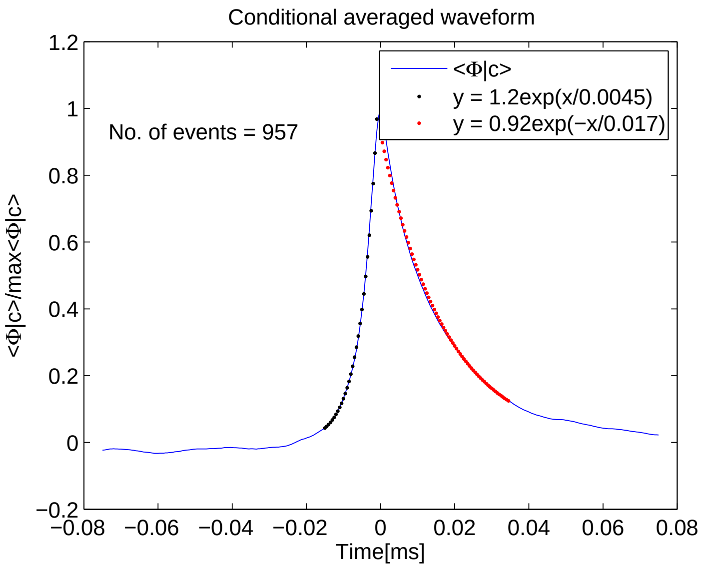

Figure 6.24 – In this figure the conditional averaged waveform in the SOL is plotted. The signal used is located at $R = 90.70\,\mathrm{cm}$, $Z = -2.99\,\mathrm{cm}$ with line-averaged density $n_e/n_G = 0.25$, the threshold used is 2.5σ. The rise and decay has been fitted by exponentials.

sented at the start of this chapter. From the time derivative skewness it was found that the fluctuation should be more symmetric in the edge region with only slightly larger decay than rise. Here it is found that the rise time is longer than the decay. This result could be effected by the fact that the background fluctuations are approximately on the same order as the high amplitude events. In addition events are both positive and negative in the edge region, while only the positive ones are sampled here.

To characterize the events it is important to see how frequent the events occur and and at what amplitudes. When talking about events, the propagating blobs are meant, therefore the analysis is only done in the SOL where the blobs are seen. The analysis is done by calculating the complementary cumulative distribution function for waiting times and burst amplitudes given in figures 6.26 and 6.27. The events are collected by the two different conditional window methods proposed in the theory part, one allowing overlap and one which do not. The events are collected with a threshold 2.5σ on standardized signals. Both figures 6.26 and 6.27 show straight line regions in a plot with logarithmic y-axis, indicating exponential distributions. Thus the events can be seen as independent events in a Poisson process, see appendix. From the figures it is clear that the distribution does not change with the method used, even though the number of events are doubled. The mean values of the exponential distributions are

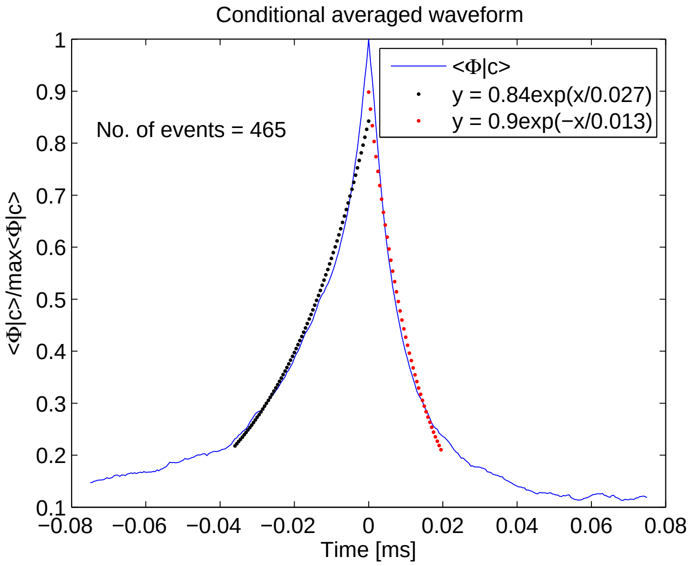

Figure 6.25 – In this figure the conditional averaged waveform in the edge region is plotted. The signal used is located at $R = 88.39\,\mathrm{cm}$, $Z = -2.99\,\mathrm{cm}$ with line-averaged density $n_e/n_G = 0.25$, the threshold condition used is 2.5σ. Exponential fits have been done unsuccessfully.

almost equal. The number before the exponential is due to the fact that this is a discrete signal so the distribution is not a true density function it is a discrete mass function, the integral of the PDF is not equal to 1, but the sum is.

For the amplitude distribution the probability has a curved shape for small amplitudes with the no overlap method, this is likely because the method favors high amplitude peaks. The overlap method suggests another exponential region for small peaks, different than the one for large peaks. The correct mean amplitude is the one for large peaks, since large peaks are not as easily effected by overlapping events. The true mean amplitude is found from the non standardized signal, i.e.,

$$\langle X\rangle = \langle X_{stand}\rangle \cdot \sigma_X + \mu_X. \tag{6.9}$$

Thus $\langle A\rangle = 1.05$, five times larger than the value found by the PDF. The two methods will be compared later with computer generated data. The waiting time and amplitude distribution has been calculated also for the edge region, no exponential distributions was found.

In figure 6.28 λ_w, the mean waiting time, is plotted as a function of line-averaged density and radius in the SOL. The method used for conditional average is the one which allows overlap and the threshold condition used is 2.5σ. From the figure it is clear that events appear more frequently close

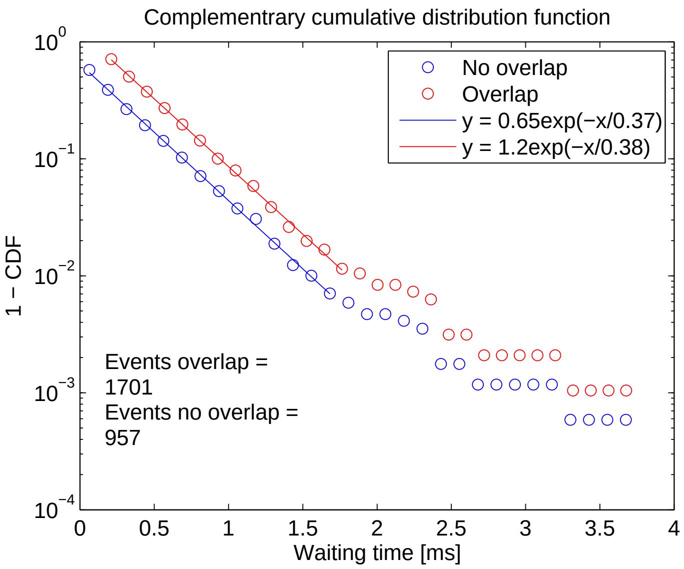

Figure 6.26 – In this figure the complementary cumulative distribution function (CCDF) for waiting times is plotted. Two different methods has been used to collect events, blue no overlap and red overlap. Both methods result in exponential distributed waiting time. The signal used is standardized and located at $R = 90.70\,\mathrm{cm}$, $Z = -2.99\,\mathrm{cm}$ with $n_e/n_G = 0.25$.

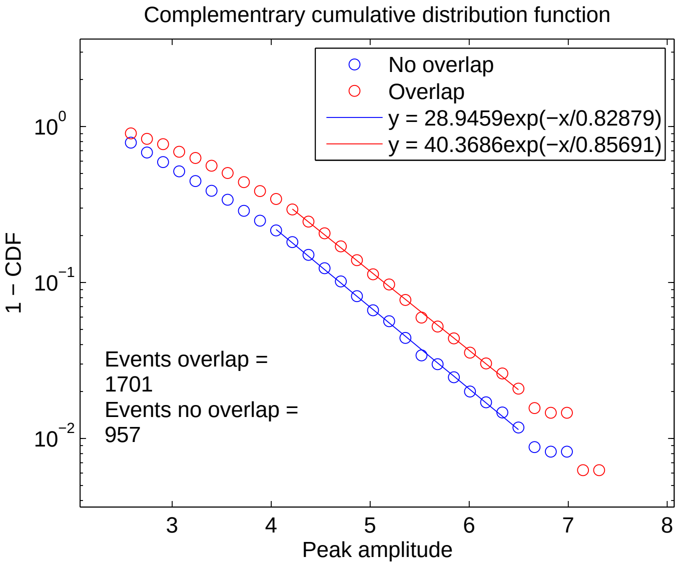

Figure 6.27 – In this figure the CCDF for peak amplitudes is plotted. Two different methods has been used to collect events, blue no overlap and red overlap. Both methods result in exponential distributed peak amplitudes. The signal used is standardized and located at $R = 90.70\,\mathrm{cm}$, $Z = -2.99\,\mathrm{cm}$ with $n_e/n_G = 0.25$.

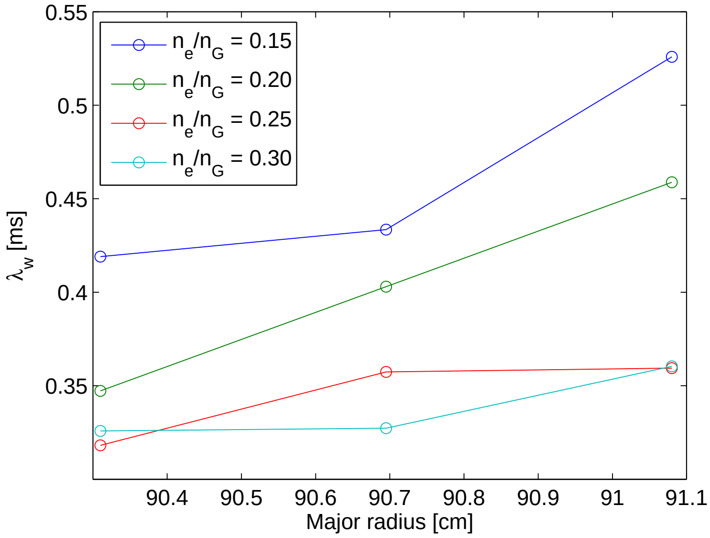

Figure 6.28 – The figure describes the mean waiting time as a function of line-averaged density and radius in the scrape off layer. The signal used is standardized and located at $Z = -2.99\,\mathrm{cm}$.

to separatrix than further away. In addition higher line-averaged density results in more frequent events. These results are consist with the result found from the moments, figure 6.6, by assuming that the signals could be described by the stochastic model. It should be mentioned that the waiting times are highly dependent on the threshold, thus the change of moments with major radius and line-averaged density could effect the result. In figure 6.29 the mean peak amplitude is plotted as a function of major radius and line-averaged density. From the figure one can see that the magnitude of the bursts decreases as the line-averaged density increases. The signals used are standardized signals so the results found are possibly due to the variations of μ and σ/μ in the SOL, see figures 6.5 and 6.6. The true mean values gives the opposite result, decrease with major radius and increase with line-averaged density. The effect of γ on the amplitude distribution will be analyzed by the stochastic model. Another possible error to this result is that the length of the exponential fit varies with major radius and line-averaged density. Especially the highest line-averaged densities show slightly curved exponentials.

It was seen at the beginning of this chapter that a burst-like shape as shown in figure 6.24 was only seen for signals located in the SOL, not in the edge region or at the separatrix. In figure 6.30 the conditionally averaged waveform is plotted for all radial positions. In the figure the waveforms has been subtracted by their minimum value and divided by their maximum. The red

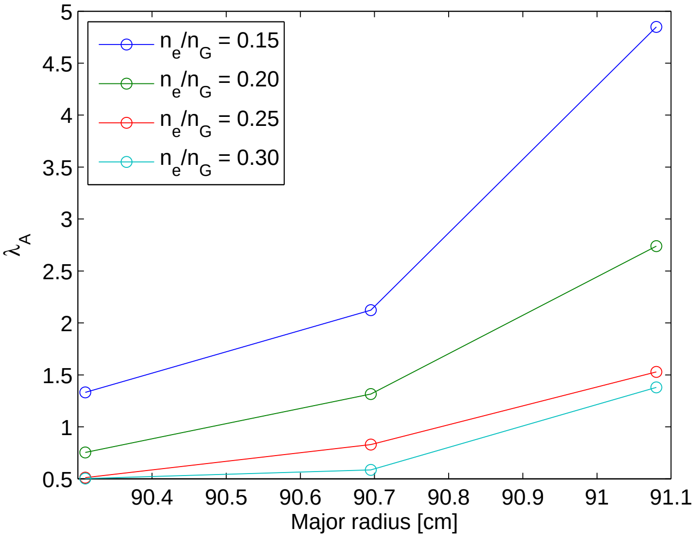

Figure 6.29 – The figure describes the mean amplitude as a function of line-averaged density and radius in the scrape off layer. The signal used is standardized and located at $Z = -2.99\,\text{cm}$.

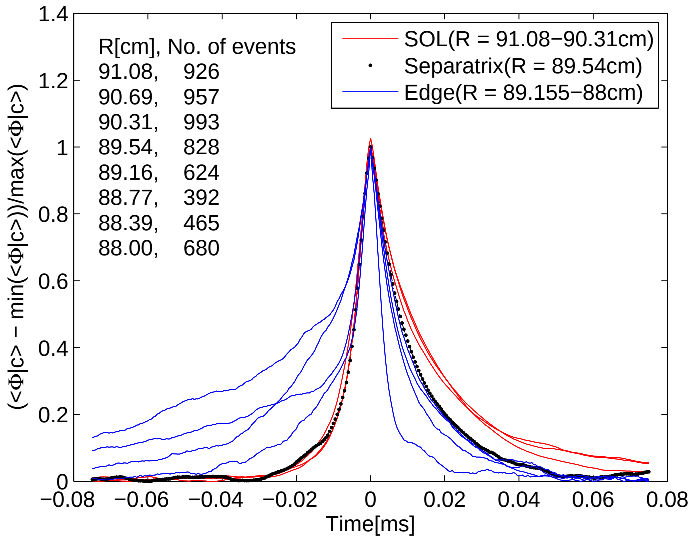

Figure 6.30 – In the figure the average waveform is plotted for all radial positions for $n_e/n_G = 0.25$ and $Z = -2.99\,\text{cm}$. The red lines are points in the SOL, The black dotted line is the separatrix and the blue lines edge region measurements. The upper left corner shows number of events as a function of major radius when the threshold condition is 2.5σ.

lines in the figure are SOL points, black is separatrix and the blue lines are from signals located in the edge region. In the SOL the averaged waveforms are all equal with the same waveform seen in figure 6.24. At the separatrix the waveform has the same rise time as the SOL points, but a faster decay, resulting in a symmetric waveform. In the edge region the conditional waveform suggests a waveform with a slow rise and a faster decay. In the edge region none of the waveforms overlap, there does not seem to be a characteristic waveform. In addition time derivative skewness shown previously, figure 6.10, suggest that the signal on average spends as much time going up as down, thus events seems unlikely to occur.

6.6.1 Plasma holes

In this section the conditional averaged waveform will be estimated for negative amplitudes. Some numerical simulations and experiments have shown that when a burst is created a negative depletion is also created traveling in opposite direction with opposite sign, [8, 18, 94]. From the signal plotted for the SOL in the start of this chapter it is clear that no such thing takes place in the SOL. The SOL does not have significant negative amplitude bursts. In addition a positive skewness in the edge region makes holes unlikely, see Boedo et al. [8]. The negative conditional amplitude waveform for all radii in the edge region is plotted in figure 6.31. In the figure the waveforms have been inverted, the signal has line-averaged density $n_e/n_G = 0.25$ and $Z = -2.99\,\text{cm}$. The amplitude threshold used is -2σ. A lower threshold value is used than for positive events because there are less negative events, can be seen by the positive skewness. For the figure it is clear that negative holes does not take place in the edge region. All waveforms are more or less symmetric and none of them look similar to another.

6.6.2 Waveform consistency

In this section the conditionally averaged waveform will be analyzed at different amplitudes. This is done by setting the condition to an amplitude interval instead of a threshold. The amplitude intervals used are $2 - 4\sigma$, $4 - 6\sigma$ and $6 - 8\sigma$. The results for one single signal located at $R = 90.70\,\text{cm}$, $Z = -2.99\,\text{cm}$ with $n_e/n_G = 0.25$ is given in figure 6.32. From the figure it is clear that the waveform of the event is independent of the amplitude. Even when the number of events get less than 50 the waveform is maintained. Thus the average blob duration for any amplitude of the blob is approximately 20–25μs. It can also be shown that this is the case for all radial positions in the SOL ($R = 91.08 - 90.70\,\text{cm}$) and for all line-averaged densities ($n_e/n_G = 0.15 - 0.30$), the result is given in figure 6.33. In the figure the waveforms for all the amplitude intervals is plotted for all SOL positions and line-averaged densities. Thus the duration of a blob is inde-

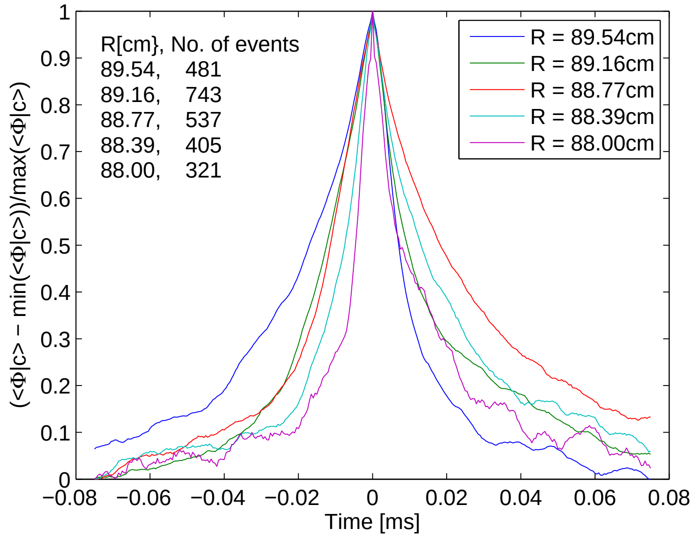

Figure 6.31 – In this figure the inverse of the negative average conditional waveform for negative amplitude peaks are plotted. The signal has $n_e/n_G = 0.25$ located at $Z = -2.99\,\text{cm}$.

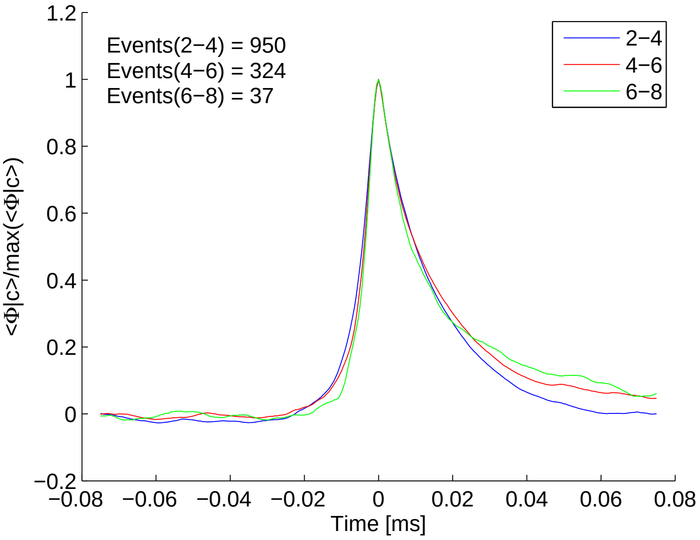

Figure 6.32 – Conditional waveform for four different threshold intervals. The signal is located at $R = 90.70\,\text{cm}$ and $Z = -2.99\,\text{cm}$ with line-averaged density $n_e/n_G 0.25$.

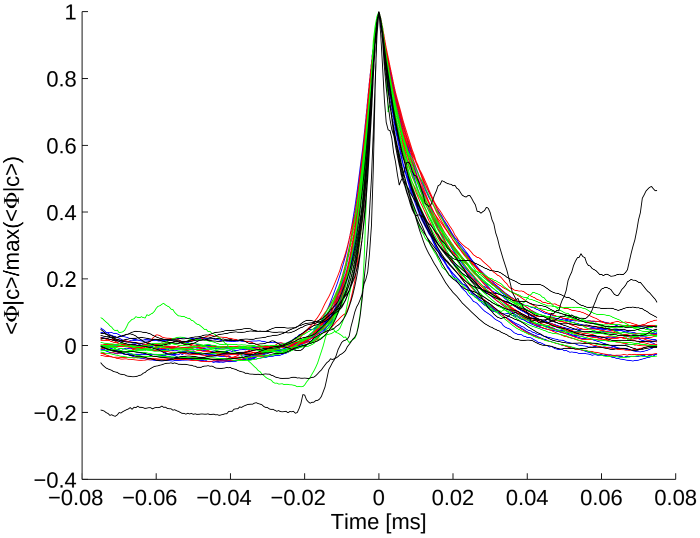

Figure 6.33 – Conditional waveform for all line-averaged densities and amplitude intervals $2-4\sigma$, $4-6\sigma$ and $6-8\sigma$ at $Z=-2.99\,\mathrm{cm}$, $R=89.925$ – $91.08\,\mathrm{cm}$ with $n_e/n_G=0.15$ – 0.30.

pendent of amplitude, line-averaged density and radius. For the edge region this is not the case, in figure 6.34 the conditionally averaged waveform is given for threshold intervals in the edge region ($R=88.39\,\mathrm{cm}$). From the figure it is clear that the shape of the waveform is similar for all thresholds with a slow rise and a sharp decay, but the parameters varies more than in the SOL. Thus as before the edge region does not seem to have a characteristic waveform.

6.7 Conditional variance

As mentioned in the theory part of this thesis the conditional variance is a measure of the reproducibility of a given waveform in the signal. The reproducibility r is defined as,

$$r = 1 - V_{con}, \tag{6.10}$$

where V_{con} is the conditional variance. In this section the data used is located at $Z=-2.99\,\mathrm{cm}$ with line-averaged density is $n_e/n_G=0.25$. In figure 6.35 r is given as a function of time for a measurement in the SOL ($R=90.70\,\mathrm{cm}$). The figure shows high reproducibility of waveform after peak amplitude and weak before. The result has to do with overlap where the sharp rise is much more sensitive to overlap than the decay.

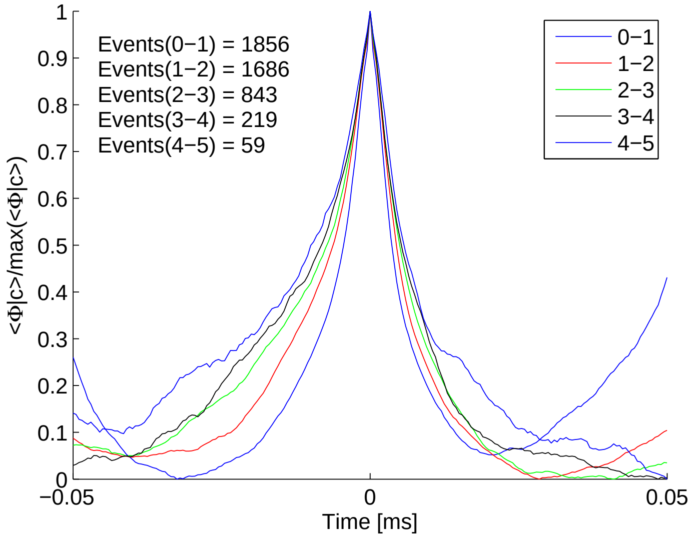

Figure 6.34 – Conditional waveform for four different threshold intervals in the edge region $R = 88.39\,\text{cm}$, $Z = -2.99\,\text{cm}$ and $n_e/n_G = 0.25$.

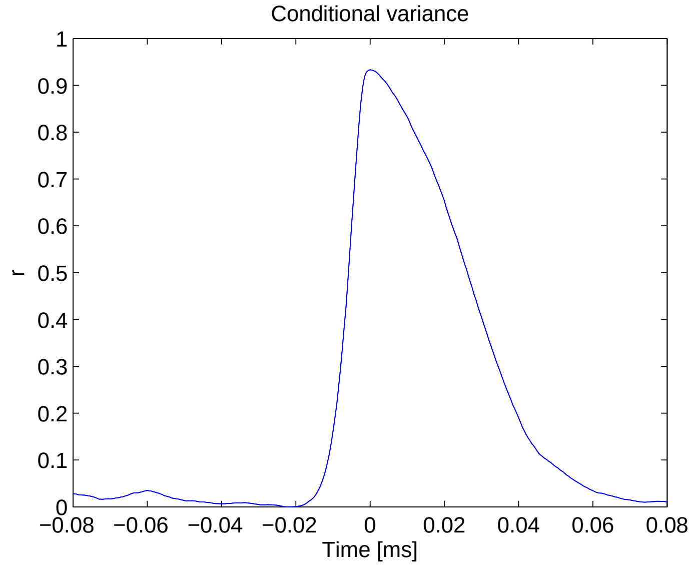

Figure 6.35 – In this figure the reproducibility is plotted as a function of time in the SOL, $R = 90.70\,\text{cm}$, $Z = -2.99\,\text{cm}$ and $n_e/n_G = 0.25$. The figure verifies that there is a returning burst-like shape occurring in the SOL.

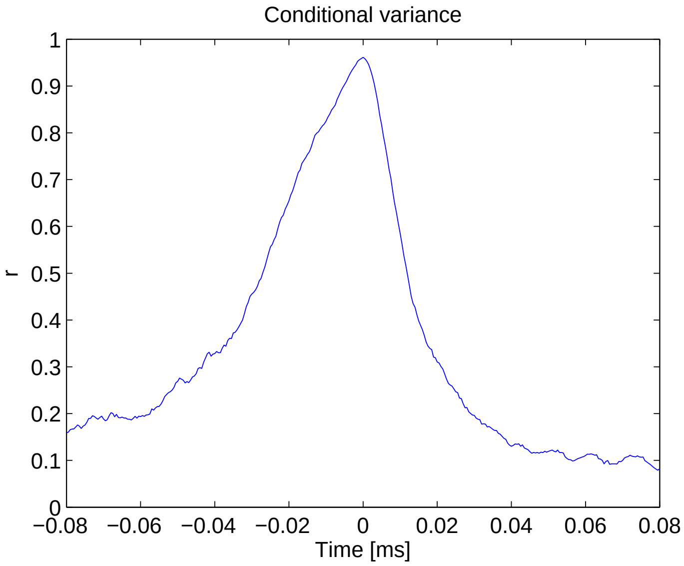

Figure 6.36 – In this figure the reproducibility is plotted as a function of time in the edge region ($R = 88.39\,\mathrm{cm}$). The figure verifies that there is a returning waveform in the edge region data.

In figure 6.36 r is plotted as a function time for a signal in the edge region, $R = 88.39\,\mathrm{cm}$, $Z = -2.99\,\mathrm{cm}$ and $n_e/n_G = 0.25$. In the edge region there is a high reproducibility before the peak and large variability after maximum. This is quite surprising since previous results have suggested that there are no characteristic waveform in the edge region. This effect could be due to the nature of the measurements. Every event is collected by a waveform around maximum so every waveform will decrease on both sides. Thus the reproducibility will always be large around maximum. But still a larger part of the edge region waveform has higher reproducibility than the SOL waveform. Could be something related to drift wave turbulence. Drift wave turbulence will not be covered by this thesis, but have been discussed elsewhere [63–65, 67].

6.8 Self-organized criticality

The concept of self-organized criticality was introduced previously where a system builds itself up to a critical state. It was shown previously that the waiting times are exponentially distributed, thus the individual bursts are independent of each other. Therefore the blobs can not be described by self-organized criticality. Another way to analyze the self-organized criticality is by analyzing the waiting times versus the peak amplitudes. For a self-organized system it is expected that longer waiting times should result in

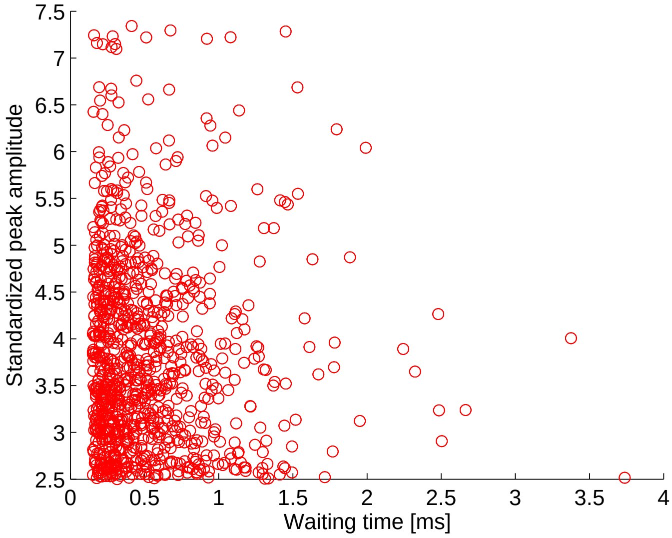

Figure 6.37 – In this figure the peak amplitude is plotted as a function of the waiting time before the peak. The signal used has $n_e/n_G = 0.25$ and is located in the SOL with $R = 90.70\,\mathrm{cm}$ and $Z = -2.99\,\mathrm{cm}$.

larger amplitudes. In figure 6.37 the peak amplitude is plotted as a function of the waiting time leading to that peak. From the data the linear Pearson correlation coefficients has been estimated to -0.0389. Thus the peak amplitude and waiting time is not linearly correlated, a geometric relation also seems unlikely. This further verifies the fact that the blobs in the SOL can not be explained by self-organized criticality.

6.9 Hurst exponent

In this section the Hurst exponent will be estimated by the different methods described in the theory part. The focus of this section will be on one spatial location to introduce the methods on experimental data. The signal used is standardized and located in the SOL, $R = 90.70\,\mathrm{cm}$, $Z = -2.99\,\mathrm{cm}$ with line-averaged density $n_e/n_G = 0.25$.

6.9.1 Autocorrelation

The autocorrelation is calculated in matlab by using the matlab function "xcorr" for a signal with zero mean. The autocorrelation coefficients for the signal used in this section is plotted in figure 6.38. The result shows long decay time, suggesting long range correlations in the signal, as shown in Sanchez et al. [80]. The Hurst exponent can be calculated from the autocorrelation coefficients by a power law fit. For these data no power law

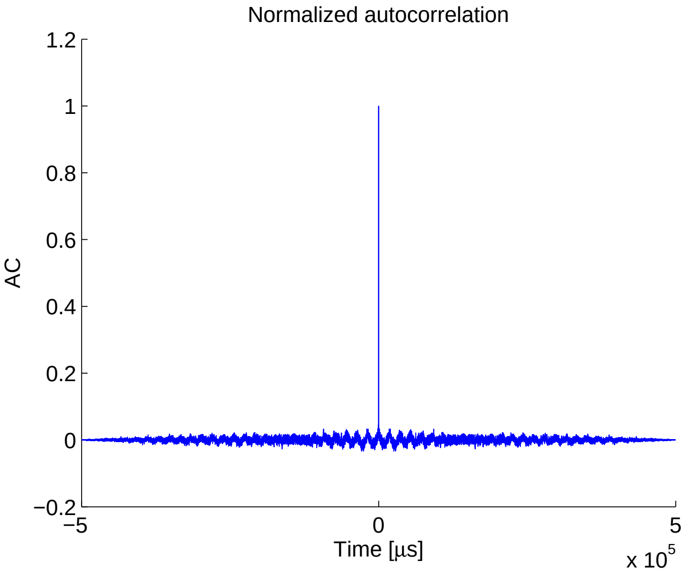

Figure 6.38 – In this figure the autocorrelation coefficients are plotted as a function of time. The signal is located in the SOL with $R = 90.70\,\mathrm{cm}$, $Z = -2.99\,\mathrm{cm}$ and $n_e/n_G = 0.25$ is plotted.

region was found for the autocorrelation coefficients. It was also seen on computer generated data that the method was inconclusive.

6.9.2 Power specter

The power specter is here estimated by Blackman-Turkey spectral estimation [46]. The windows are sampled by a Hamming window with a width of 10000 (length of signal dived by 100). The matlab function used is "pwelch". The power specter is plotted with logarithmic axis in figure 6.39. Three vertical lines have been inserted in the figure representing the mean waiting time (red), e-folding time autocorrelation (magenta) and mean burst duration (black). Two possible power law regions have been fitted to the data resulting in $\beta = 0.26$ for large time scales ($2.5 * 10^2 - 4 * 10^3\,\mu\mathrm{s}$), the power law region is slightly over one decade. This region is also consistent with the self-similar region found previously by the wavelet method. It was previously found that the Hurst exponent can be calculated from the power specter by [57],

$$\begin{aligned} S(f) &\propto f^{-\beta}, \\ \text{fGn: } \beta &= 2H - 1, \\ \text{fBm: } \beta &= 2H + 1. \end{aligned} \tag{6.11}$$

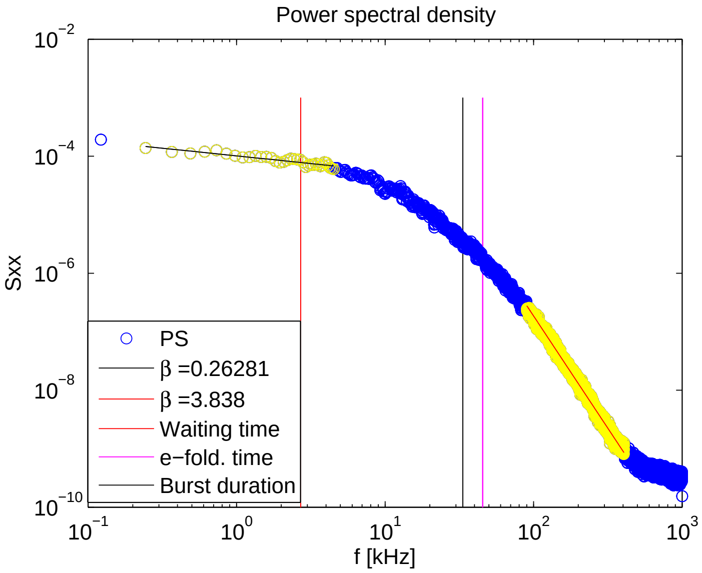

Figure 6.39 – In this figure the power specter has been estimated and plotted with logarithmic axis. In the figure three vertical lines are inserted representing mean waiting time, e-folding time autocorrelation and burst duration. In the figure two lines have been fitted marking possible power law regions. The signal used is located in the SOL with $R = 90.70\,\text{cm}$, $Z = -2.99\,\text{cm}$ and $n_e/n_G = 0.25$.

Thus for large time scales the signal is an fGn, $-1 < \beta < 1$, which gives $H = 0.63$. For short time scales $(2.5 - 16.67\,\mu\text{s})$ β is above the fBm value, in addition the power law fit is less than one decade. Thus Hurst exponent calculation for short time scales does not make sense.

6.9.3 Rescaled range

The method for calculating the rescaled range was introduced previously and will be used in this subsection to calculate the Hurst exponent. A logarithmic plot of the rescaled range as a function of the time scale is given in figure 6.40. In the figure vertical lines have been inserted representing the mean waiting time, e-folding time scale for the autocorrelation and the mean burst duration. In the figure the estimated points have been fitted by three lines for three different time scale regions. The short time scales less than $10^2\mu$s has $H = 1$, this is due to a non stationary signal as was shown by the power specter. For time scales larger than $10^4\mu$s, $H \approx 0.5$ resulting in no long range correlations, could also be an effect of limited time series length. For the intermediate time scales $H = 0.68$. The fit covers almost two decades, approximately in the same range as the power law fit to the power specter and the self-similar region calculated previously.

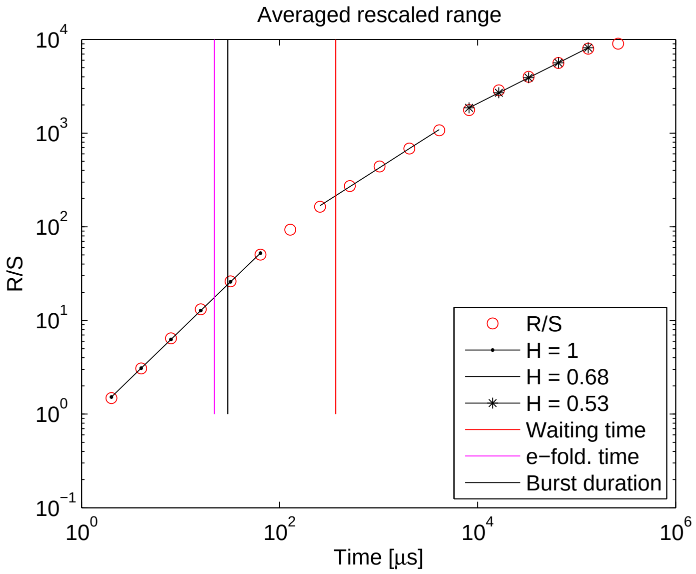

Figure 6.40 – In this figure the estimated averaged rescaled range is plotted with logarithmic axis. In the figure three vertical lines are inserted representing mean waiting time, e-folding time autocorrelation and burst duration. In the figure three lines have been fitted marking possible power law regions. The signal used is located in the SOL with $R = 90.70\,\mathrm{cm}$, $Z = -2.99\,\mathrm{cm}$ and $n_e/n_G = 0.25$.

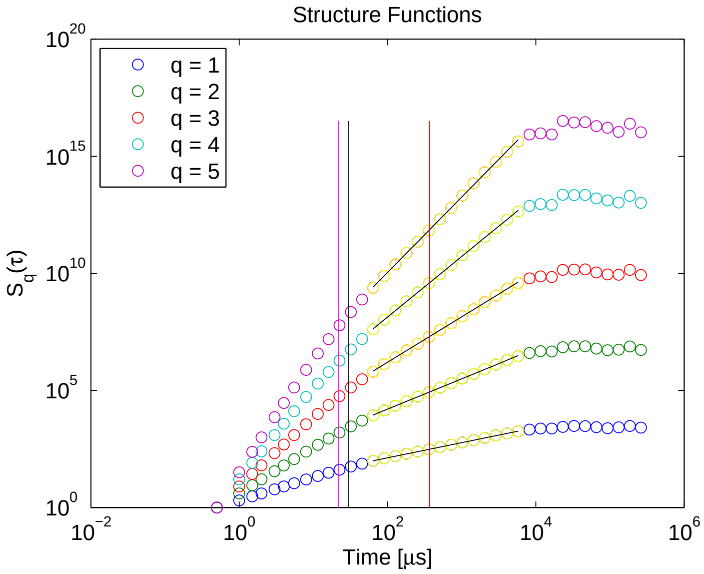

Figure 6.41 – In this figure the structure functions for $q = 1, 2, 3, 4, 5$ is plotted. In the figure three vertical lines are inserted representing mean waiting time (red), e-folding time autocorrelation (magenta) and burst duration (black). The yellow marked areas with a black lines represent the stationary part of the fGn where the fit has been estimated.

6.9.4 Structure Functions

In this section the structure functions for $q = 1, 2, 3, 4, 5$ is calculated and used to evaluate the Hurst exponent. The structure functions are plotted in figure 6.41 with a fitting range from $10^2 - 10^4 \mu$s. The fitting range is found by plotting the structure functions for the non cumulated signal, where a straight line represents the stationary part. Notice that the fitting range is similar to that used by previous methods and the self-similar region found by the wavelet method. Three vertical lines has been inserted in the figure representing mean waiting time (red), mean burst duration (black) and e-folding time scale for the autocorrelation (magenta). The method for estimating the Hurst exponent from the structure functions was found previously, see Yu [95],

$$S_q \propto |\tau|^{\zeta(q)} = |\tau|^{qH}. \tag{6.12}$$

Thus the Hurst exponent can be found from linear regression of ζ vs q given in figure 6.42. From the figure the Hurst exponent is estimated to 0.64.

6.9.5 Wavelet analysis

In this subsection wavelet coefficients are estimated and used to calculate the Hurst exponent. The variance of wavelet coefficients are plotted with

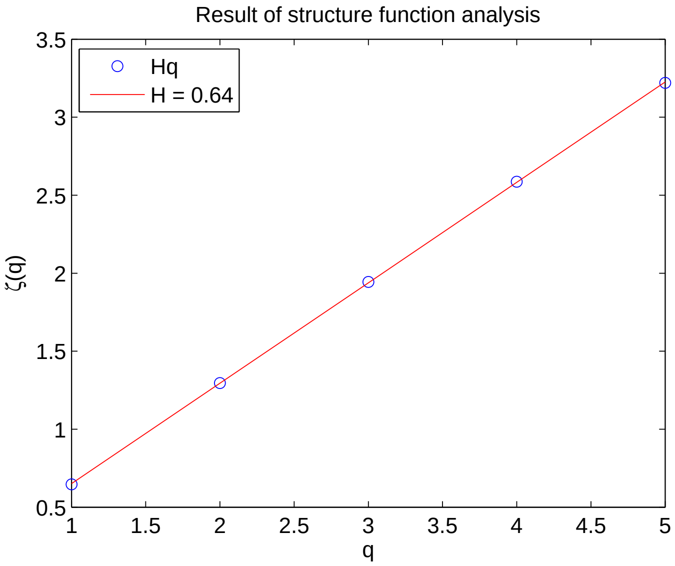

Figure 6.42 – In this figure ζ found in figure 6.41 is plotted as a function of q. A linear function have been fitted to the data and used to estimate the Hurst exponent. The signal used is located in the SOL with $R = 90.70\,\text{cm}$, $Z = -2.99\,\text{cm}$ and $n_e/n_G = 0.25$.

logarithmic axis as a function of time scale in figure 6.43. The vertical lines is as before mean waiting time, e-folding time scale for autocorrelation and mean burst duration. The Hurst exponent is estimated from the variance of wavelet coefficients by [57, 88],

$$\begin{aligned} \sigma_W^2 &\propto \tau^{-\beta}, \\ \text{fGn: } \beta &= 2H - 1, \\ \text{fBm: } \beta &= 2H + 1. \end{aligned} \tag{6.13}$$

A fitted line has been inserted for short time scales less than $10\,\mu\text{s}$ resulting in a β value slightly larger than the fBm limit. Thus $H = 1$ due to short scale effects. For intermediate time scales $10^2 - 10^4\,\mu\text{s}$ the fitted line has $\beta = 0.16$, $H = 0.58$. The fit covers approximately two decades and the fit range is similar to previous results.

6.9.6 Summary of Hurst exponents

For the signal located in the SOL, $R = 90.70\,\text{cm}$, $Z = -2.99\,\text{cm}$ and $n_e/n_G = 0.25$ the Hurst exponent has been estimated by four different methods. The estimation results are summarized in table 6.2. The results show that four methods give similar results. On average the SOL region seems to have weak

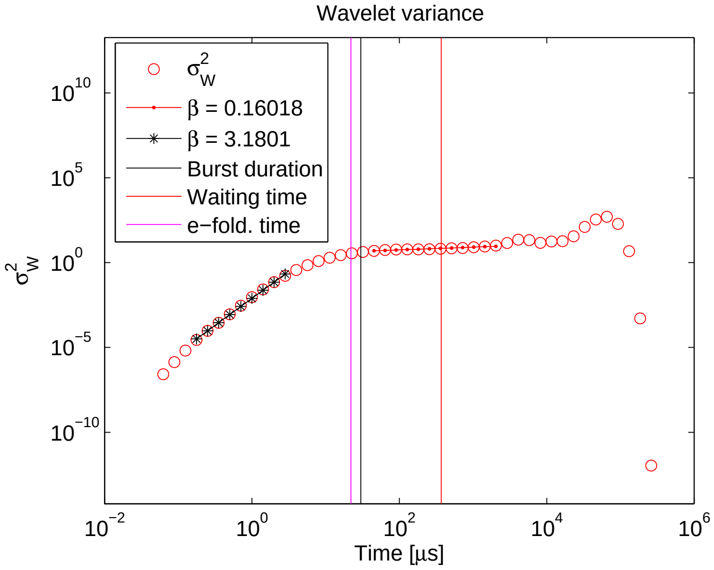

Figure 6.43 – In this figure the variance of wavelet coefficients is plotted as a function of time for a signal with $R = 90.70\,\text{cm}$, $Z = -2.99\,\text{cm}$ and $n_e/n_G = 0.25$. In the figure three vertical lines are inserted representing mean waiting time (red), e-folding time autocorrelation (magenta) and burst duration (black). The estimate has been fitted by two lines, a star line for short time scales and a dotted line for intermediate time scales.

Power Specter	0.63
Rescaled Range	0.68
Structure Functions	0.64
Wavelet analysis	0.58

Table 6.2 – The table shows result of Hurst exponent estimation by four different methods. The signal used is located in the SOL with $R = 90.70\,\text{cm}$, $Z = -2.99\,\text{cm}$ and $n_e/n_G = 0.25$.

long range correlations, this will be analyzed further for more positions and line-averaged densities in the next section. All methods have a fitting range approximately 2 decades within the self-similar region found previously, the power specter has a slightly shorter fitting range than the other methods.

6.10 Radial variations of the Hurst exponent

In this section the radial variation of the Hurst exponent will be analyzed. The signals used are standardized and located at $Z = -2.99\,\text{cm}$, $R = 91.08$ – $88.00\,\text{cm}$ with $n_e/n_G = 0.25$. In figure 6.44 the Hurst exponent are estimated by structure functions, power spectra, rescaled range and wavelets as a function of major radius. The figure shows Hurst exponent approximately constant in the SOL varying between 0.57 and 0.68. This confirms weak long range correlations in the SOL. The independent large amplitude events indicates that the signal here could consist of a superposition between a shot noise process as defined by the stochastic model and a fGn. At the separatrix a high H is estimated by the wavelet method while a low value is found by the power specter method. This could be due to bad measurements, the power law fit is only slightly longer than one decade for the wavelet method at this position. For the edge region the fit region is more or less the same as the fit region in the SOL, see the previous section. In the edge region the Hurst exponent increase from 0.5/0.6 to 0.8/1.0. Thus in the edge region there are strong long range correlations. This result confirms the long range correlation suggested by the high e-folding times for the autocorrelation found earlier in this chapter. Similar Hurst exponents as a function of majors radius has been found by Yu [95]. Carreras found an increasing Hurst exponents away from the separatrix in the SOL as in the edge region [14], but here it is approximately constant. The high Hurst exponents found in the edge region could be explained by a non-stationary signal. In Yu [95] it is shown that a non stationary signal will have Hurst exponents close to 1. The stationary test by the use of structure functions reveal that as the major radius decreases in the SOL the signal deviates slightly from stationarity. In addition the self-similar wavelet test showed that the signal is not perfectly self-similar in the edge region. A contradiction to these results are the wavelet and power specter methods which are able to verify whether the signals are stationary or non-stationary, these methods confirm that the signal is a fGn.

6.11 Hurst exponent for different line-averaged densities

In this section the Hurst exponent will be analyzed as a function of the line-averaged density. The signals used in this section are located at $Z =$

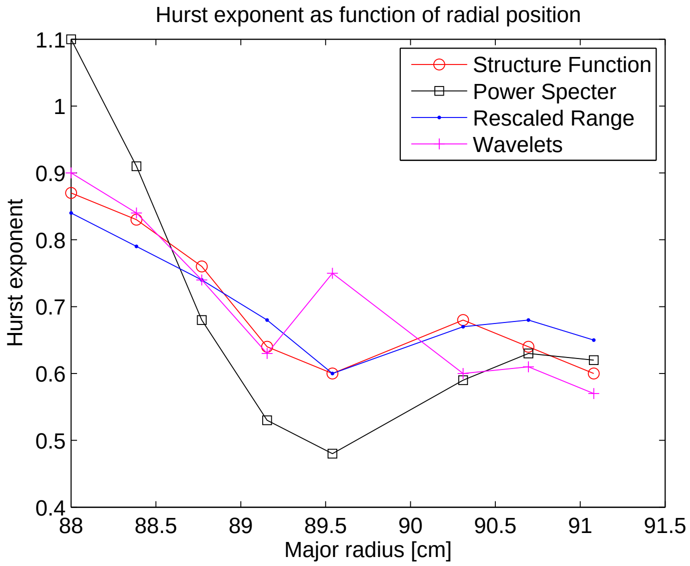

Figure 6.44 – The figure shows estimated Hurst exponent with structure function, power specter, rescaled range and wavelets as a function major radius. The signal used is located at $Z = -2.99\,\text{cm}$ and has $n_e/n_G = 0.25$.

$-2.99\,\text{cm}$. In figure 6.45 the Hurst exponents estimated by the wavelet method is given as a function of major radius for all line-averaged densities. From the figure it seems that when the line-averaged density increases the Hurst exponent in the SOL seems to increase. It should be mentioned that for the highest line-averaged density there is only one data set and the wavelet variance is curved resulting large uncertainty. Similar calculations have been done with the other methods and the Hurst exponent tends to increase with line-averaged density in the SOL, but not as drastically as for the wavelet method. For comparison the Hurst exponent calculated by the structure functions as a function of major radius and line-averaged density is given in figure 6.46. For the edge region all methods show a similar increase with approximately equal H values for all line-averaged densities.

6.12 Vertical variations of the Hurst exponent

In this section the vertical variations of the Hurst exponent will be analyzed. A contour plot of the Hurst exponents calculated by the rescaled range analysis for signals with $n_e/n_G = 0.25$ is plotted in figure 6.47. In the SOL ($R > 89.925\,\text{cm}$) the Hurst exponents are approximately constant in space. In the edge region ($R < 89.155\,\text{cm}$) the figure shows primarily vertical lines representing a Hurst exponent constant in the vertical direction. The white spots are missing data samples from the measurements.

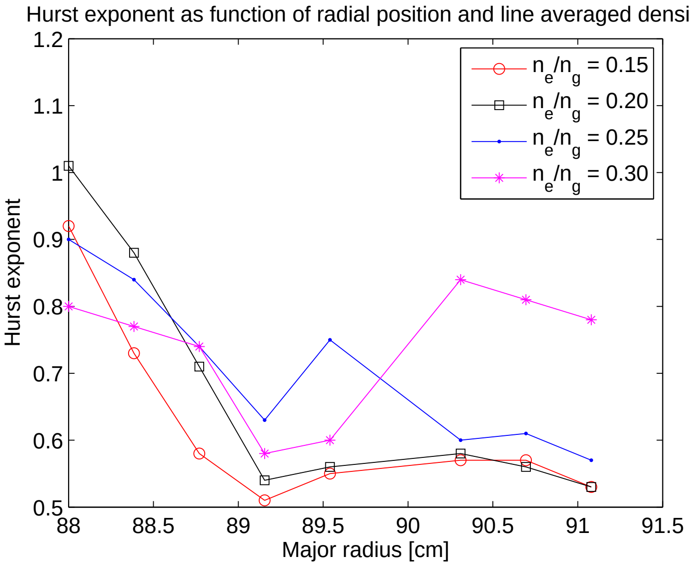

Figure 6.45 – The figure shows Hurst exponents estimated by the wavelet method as a function of line-averaged density and major radius at $Z = -2.99\,\text{cm}$.

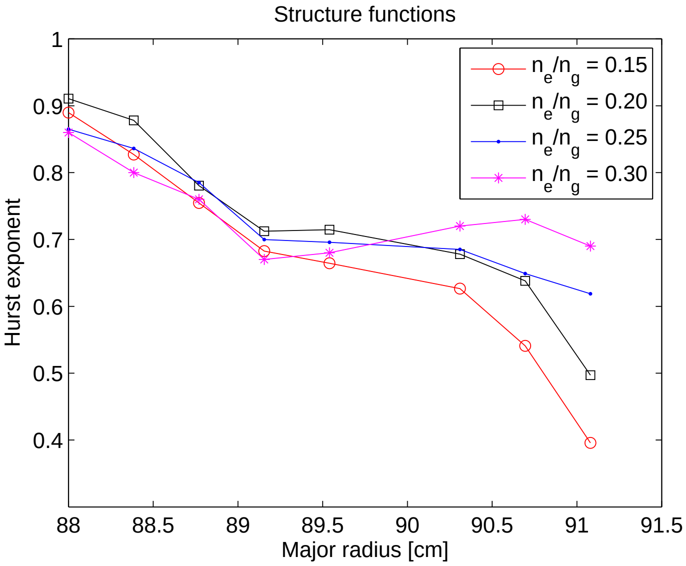

Figure 6.46 – The figure shows Hurst exponents estimated by the structure functions as a function of line-averaged density and major radius at $Z = -2.99\,\text{cm}$.

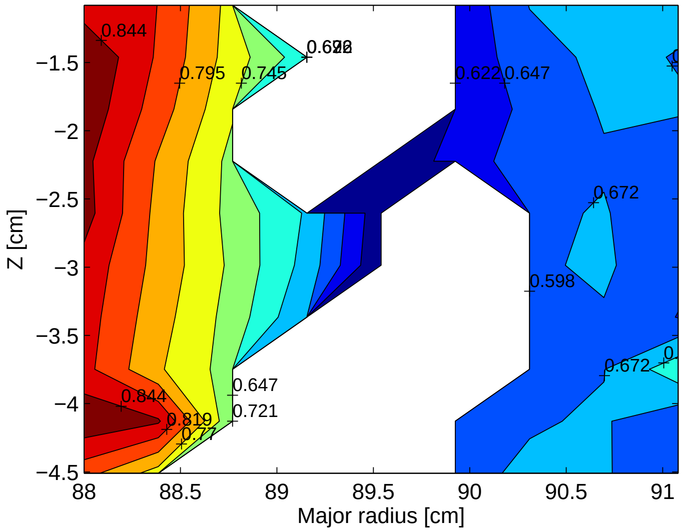

Figure 6.47 – In this figure the Hurst exponent has been calculated by the rescaled range method as a function of space for $n_e/n_G = 0.25$.

6.13 Data block randomization

In this section the Rescaled Range method will be verified by data block randomization. It has been argued that the Hurst exponent found on long time scales might be an effect of the large Hurst exponent at small time scales, [38, 84, 92]. To prove this they have done a data block randomization of the signal. If the Hurst exponent increases or stays the same after randomization the time scales considered does not have long range correlations, see Peters [69]. Data block randomization consist of splitting the signal up into equal sized boxes. Then a new signal is made by inserting each box at a random position in the signal. In figure 6.48 a comparison between autocorrelation of the signal and autocorrelation of the randomized signal is given. The long heavy tails related to long range correlations are gone for the scrambled signal. In figure 6.49 the rescaled range analysis is plotted for the signal, before (red) and after (blue) randomization. The signal used is located in the SOL $R = 90.70\,\text{cm}$, $Z = -2.99\,\text{cm}$ and $n_e/n_G = 0.25$. The Hurst exponent has significantly decreased after randomization, thus the Hurst exponent is not an effect of the smaller scales. The window size used has width 10 μs ($\delta n = 20$). Larger windows, less than the power law region, has been used and the Hurst exponent is found to decrease even for larger window sizes. For a windows size 100 μs the randomized signal has H = 0.63, while for 1000 μs H has increased to 0.70. In figure 6.50 the same calculations are done for a signal located in the edge region $R = 88.39\,\text{cm}$, $Z = -2.99\,\text{cm}$ and $n_e/n_G = 0.25$, where a larger Hurst exponent was found.

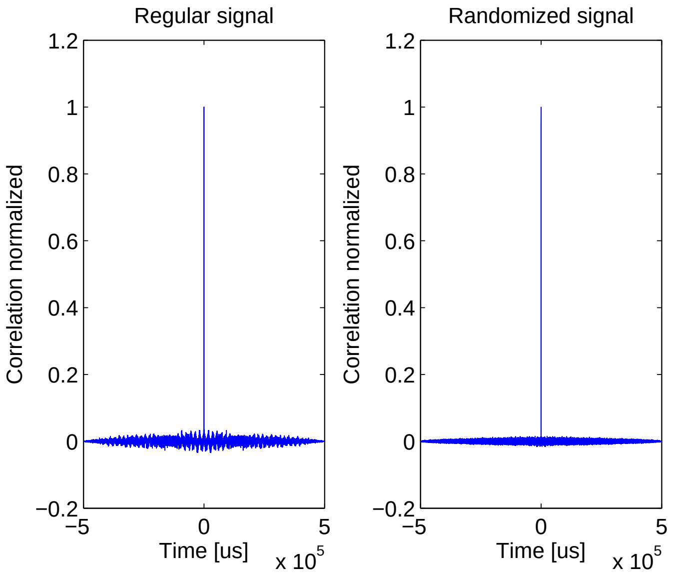

Figure 6.48 – In this figure the autocorrelation of a signal at $R = 90.70\,\mathrm{cm}$, $Z = -2.99\,\mathrm{cm}$ with $n_e/n_G = 0.25$ is plotted on the left. On the right the data randomized version of the signal is plotted.

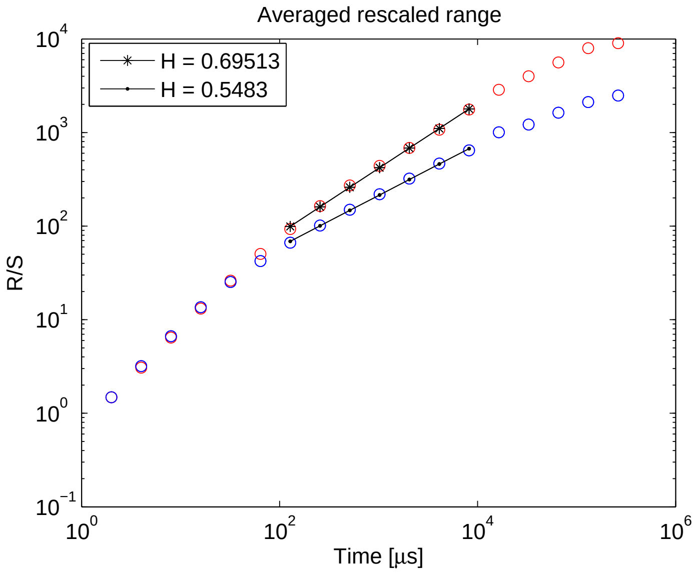

Figure 6.49 – In this figure the rescaled range method has been used to estimate the Hurst exponent for a signal at $R = 90.70\,\mathrm{cm}$, $Z = -2.99\,\mathrm{cm}$ with $n_e/n_G = 0.25$, red dots. Blue dots are the estimated rescaled range for the data randomized signal.

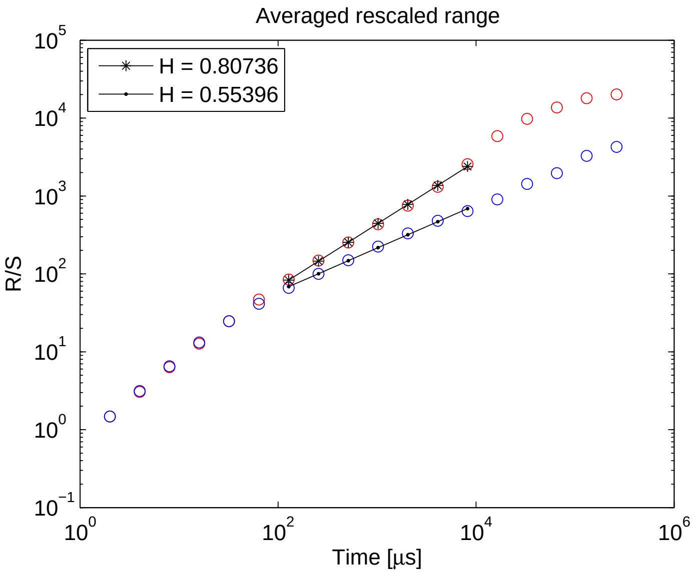

Figure 6.50 – In this figure the rescaled range method has been used to estimate the Hurst exponent for a signal at $R = 88.39\,\mathrm{cm}$, $Z = -2.99\,\mathrm{cm}$ with $n_e/n_G = 0.25$, red dots. Blue dots are the estimated rescaled range for the data randomized signal.

In this figure the result is the same as before a Hurst exponent slightly above 0.5 is found.

In figure 6.51 the same calculations are done for a computer generated fGn with $H = 0.7$. The Hurst exponent after data block randomization is similar to the value found in both the SOL and in the edge. Thus there is no evidence of high Hurst exponent being influenced by smaller scales.

6.14 Blob size and velocity

Two important properties regarding the high density blobs are their size and velocity. The size in this case is the vertical size, which in a practical sense can be interpreted as the poloidal blob size. The poloidal blob size is found by doing a conditional average with $Z = -2.99\,\mathrm{cm}$ as a reference point. Every time a local peak is sampled at $Z = -2.99\,\mathrm{cm}$ the value at all other vertical positions is saved. Thus the average value can be plotted as a function of Z to see how far from the reference the measurements have a high density measure at the same time as the reference. The conditional size is given in figure 6.52. All the data in the figure is divided by the reference value. The signals used are standardized and located at $R = 90.70\,\mathrm{cm}$. In the figure the size has been plotted for different line-averaged densities and the size is found to be independent of line-averaged density. Thus more

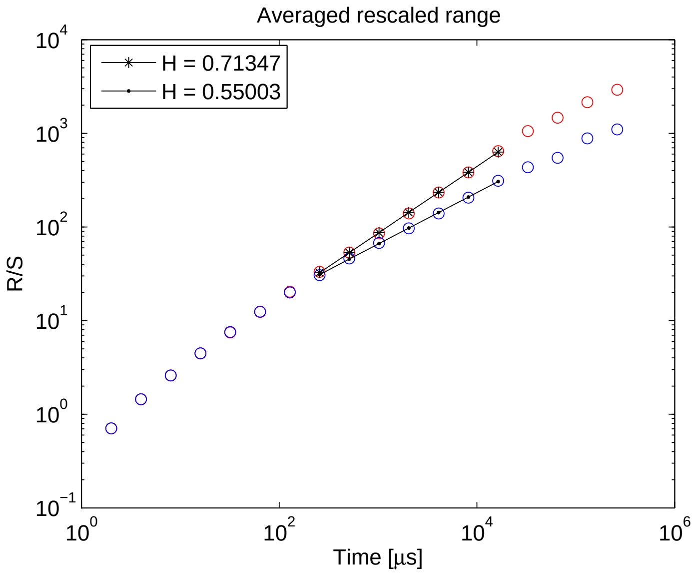

Figure 6.51 – In this figure the rescaled range has been estimated on a computer generated fGn with $H = 0.7$, before (red) and after (blue) data randomization.

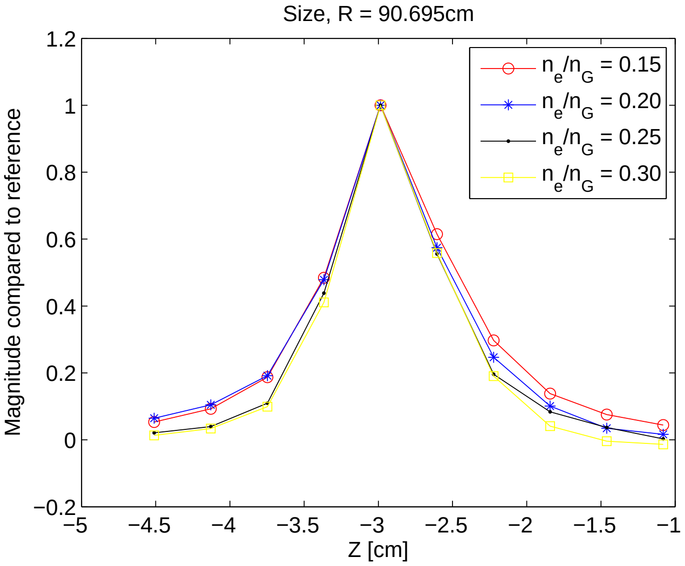

Figure 6.52 – The figure gives the vertical size blobs for different line-averaged densities at $R = 90.70\,\mathrm{cm}$.

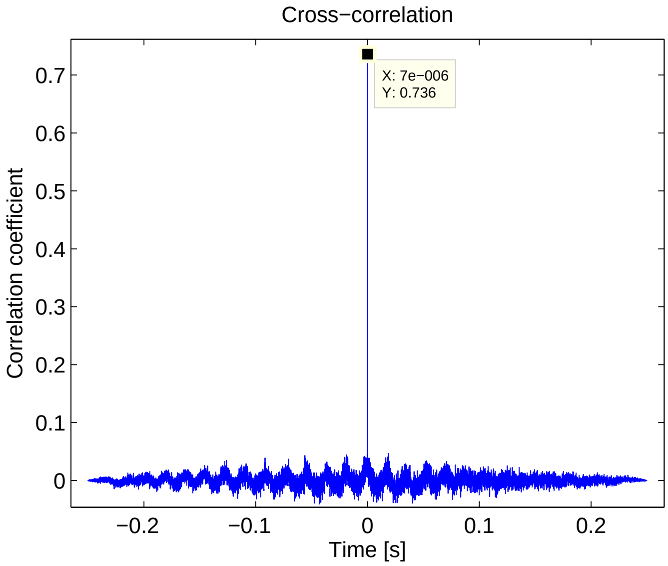

Figure 6.53 – The figure shows an example of cross correlation between two radial positions in the SOL. The signals used are located at $R = 90.70\,\mathrm{cm}$, $90.31\,\mathrm{cm}$, $Z = -2.99\,\mathrm{cm}$ and $n_e/n_G = 0.25$.

particles does not give poloidally larger blob structures. In addition the size has been found to be equal for all radial positions. From the figure the size can be estimated to $1 - 2\,\mathrm{cm}$. This is in good agreement with what was reported in a review article by Boedo [9].

The average time it takes for a blob to travel from one position to another can be found by cross-correlation. An example of the cross correlation between two radial positions is given in figure 6.53. The figure shows cross correlation between $R = 90.70\,\mathrm{cm}$ and $R = 90.31\,\mathrm{cm}$, both signals are located at $Z = -2.99\,\mathrm{cm}$ with $n_e/n_G = 0.25$. The correlation time is defined as the time shift of the peak compared to zero. The cross correlation peak has a coefficient value of around 0.7. A similar value has been found between all positions for different line-averaged densities. The relatively small values are likely caused by poloidal motion, and background density fluctuations. The blob speed can be found by dividing the distance by the correlation time between two points. Four contour plots showing the radial velocity as a function of space and line-averaged density is given in figure 6.54. The estimated radial velocity decreases with major radius and slightly with vertical position. Thus the radial velocity is largest near the separatrix where the blobs are believed to be created, possibly slowed by non-linear dispersion in the SOL [30]. As a function of line-averaged density the radial velocity seems constant except for the largest line-averaged density where it has a slight increase. The average radial velocity is approximately 1000m/s.

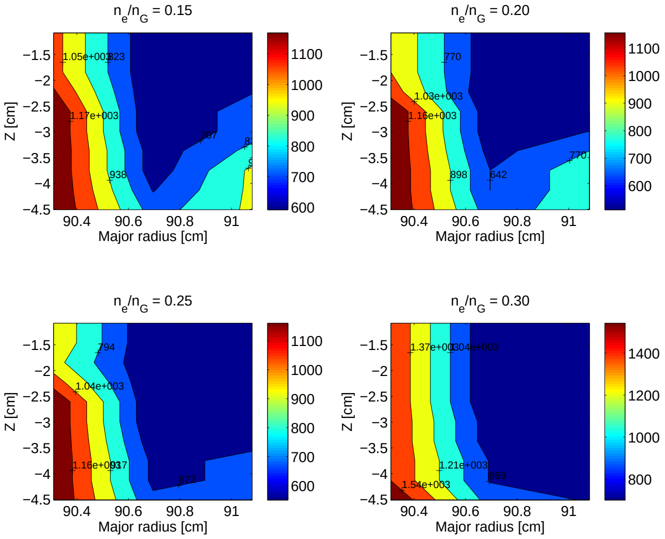

Figure 6.54 – These figures describe the estimated radial velocity as a function of space for different line-averaged densities.

The vertical (poloidal) blob velocities are given in figure 6.55. In the vertical direction the speeds are slightly larger than in the radial direction with a slight increase for increasing line-averaged density. The average velocity is directed downwards, away from the midplane. Similar results are reported in the review article by Boedo [9]. The result is consistent with blobs created at the midplane propagating towards the divertor targets. For the highest line-averaged density the maximum velocity is found far away from the midplane, inconsistent with the other line-averaged densities. It should be mentioned that some of the sensors are damaged, in these cases the velocity value is taken from the nearest neighbor.

In the theory part two velocity scalings were found from the current continuity equation with two different closure schemes, sheath dissipation and ideal interchange. The velocity scalings where given by,

$$\frac{V_b}{C_s} = 2\left(\frac{\rho_s}{l}\right)^2 \frac{l_\parallel}{R}. \tag{6.14}$$

$$\frac{V_b}{C_s} = \left(2\frac{l}{R}\frac{\Delta n}{N}\right)^{1/2}, \tag{6.15}$$

The physical quantities for this experiment was $B = 4$T, $M_i = 3.32{*}10^{-27}$, $T_e = 30$eV, $\Delta n/N \approx 1$, $l \approx 1.5\,$cm, $L_\parallel = 12\,$m and $R = 0.9\,$m. From the

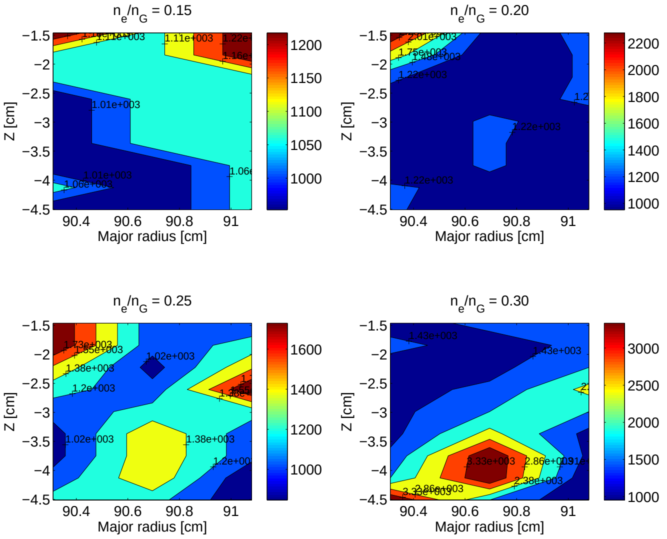

Figure 6.55 – These figures describes the estimated vertical blob velocity as a function of position and line-averaged density.

sheath closure this gives a velocity of 180 m/s. This is 4 – 5 times less than estimated from the data. For the ideal interchange a velocity of around 7000 m/s is found, much larger than the experimental value. The velocities seen for both closure schemes are expected since they represent ideal cases. When all terms are kept in the current continuity equation we expect a velocity which lies in between the two [50], as does the measurements.

Chapter 7

Probe measurements

In this chapter data measured by Langmuir probes on Alcator C-Mod will be analyzed. The measurements consist of two shot sessions 1120210 (ISP) and 1111208 (ASP). The ASP measures floating potential in two channels and ion saturation current ($I_{sat} \propto nT^{1/2}$) in two channels. The ISP data has one channel measuring ion saturation current. Both measurements are taken at the upper outboard midplane. The data consists of long time series of around $0.5 - 1.5\,\mathrm{s}$, with $3 - 5$ million data points. The useful parts where the physical quantities are constant is approximately $0.3 - 0.8\,\mathrm{s}$.

7.1 ASP measurements

In this section ASP data in the far SOL, primarily shot 1111208010, will be analyzed. Due to varying data quality, only three other shots will be used from the ASP session, the varying physical quantities are listed in table 7.1. The constant physical quantities are, $B_\phi = 5.4\,\mathrm{T}$, $R = 0.865\,\mathrm{m}$ and $\rho = 0.111\,\mathrm{cm}$. As for the GPI data the measurements have been detrended and standardized.

In figure 7.1 the standardized (a) ion saturation current and (b) floating potential is plotted as a function of time. The ion saturation current has a burst-like shape with individual burst amplitudes much larger than the standard deviation, as seen for the GPI data in the SOL. The floating potential (b) seems to have a signal dominated by negative bursts, but compared to

Shot	008	010	011	016
n_e/n_G	1.0	1.15	1.12	0.86
I_p [MA]	0.55	0.55	0.55	0.80

Table 7.1 – This table shows the varying physical quantities for the shots which will be used in this section.

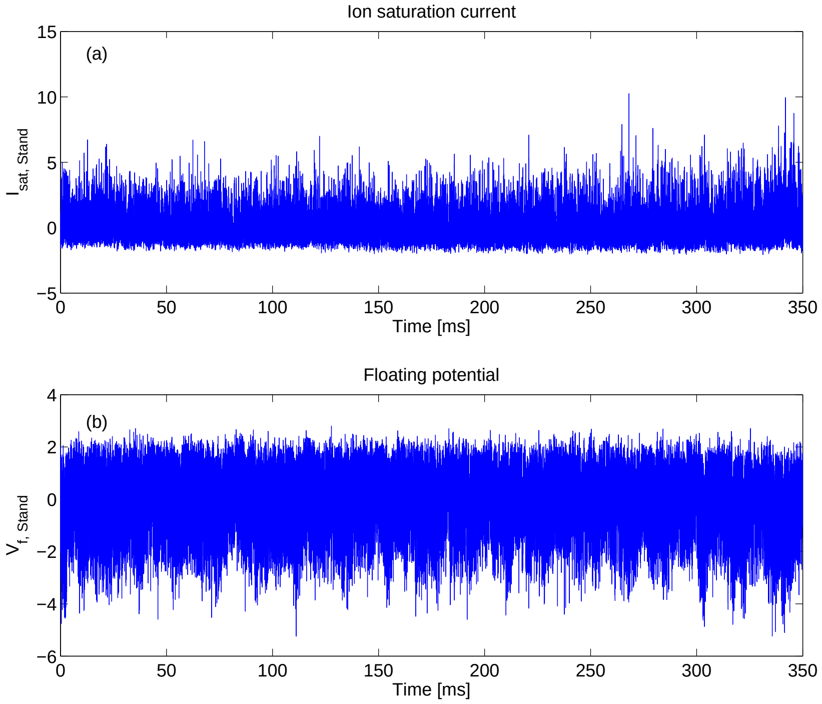

Figure 7.1 – In this figure the raw time series of standardized (a) ion saturation current and (b) floating potential is plotted. The shot used is ASP 010.

the standard deviation the peaks are relatively small. A closer look at the signal reveals no clear waveform, but seemingly random fluctuations. Since the probe consist of four heads, it is possible to estimate the electric drift and particle flux by,

$$\begin{aligned} u_E &= \frac{\Delta V_f}{\Delta r B}, \\ \Gamma &= I_{sat} u_E. \end{aligned} \tag{7.1}$$

In the equation above u_E is the electric drift, ΔV_f is the difference between the measured floating potentials of the two channels, Δr is the distance between probe heads, B is the magnetic field strength, Γ is the particle flux and I_{sat} is the ion saturation current.

In figure 7.2 the probability density functions (PDF) of I_{sat}, V_f, u_E and Γ is plotted. The non standardized PDF for ion saturation current (a) has a heavy tail towards large positive values indicating frequent appearance of bursts. In the figure fitted lines for gamma and Sattin distributions have been inserted. The Sattin distribution provides an almost perfect fit while the gamma distribution fails to fit the right side tail. The scale and shape parameters for the gamma distribution are $k = 0.27$ and $\theta = 0.012$. Assuming that the signal can be described by the stochastic model $\langle A \rangle = 0.12$ and $\gamma = 0.27$. This implies relatively long waiting times as seen for the far SOL by the GPI measurements. The floating potential (b) has a slightly skewed PDF, possibly caused by temperature fluctuations. Similar deviation from Gaussian statistics is found for all shots analyzed. The electric drift (c) follows a normal distribution, with an average radial velocity of 120m/s. The distribution has a shift towards large positive values caused by the fast moving blobs. The low velocity value could be explained by the distance between probe heads of only 2.2mm, which is smaller than the radial blob size found for the GPI data. In addition the velocity is the drift for the whole plasma not just the blobs, it has both positive and negative values, a small average value should be expected. The flux distribution has heavy tails towards large values, caused by the large density blobs, as seen by Carreras [11].

The conditionally averaged waveforms for the signals are found by using the ion saturation current as reference. This means that every time the threshold condition is met for the ion saturation current a waveform is sampled for all signals. Thus the waveforms related to large density events are found for each signal. The threshold condition used is 2.5σ. The resulting conditionally averaged waveforms are plotted in figure 7.3. The conditionally averaged waveform for (a) the ion saturation current has a burst-like shape with a fast rise and a slower decay similar to the GPI data. The waveform is too peaked and flats out too fast for exponential raise and decay to fit well. The duration is found to be $15 - 25\,\mu$s, similar to the value found by the GPI data. For the ISP data the conditionally averaged waveform has been found for 15 different shots and found to have approximately the same form, see figure 7.4. Except for the sharp peaks the waveforms seems to fit exponential rise and decay times well. In the figure a typical conditionally averaged waveform measured by the GPI in the SOL, $R = 90.70\,\mathrm{cm}$, $Z = -2.99\,\mathrm{cm}$, $n_e/n_G = 0.25$, is also plotted. It can be seen that the probe data has a sharper, symmetric peak than the GPI data. The same result is found for the ASP measurements. This could be due to a smoothing effect caused by the 3.7 mm in spot size of the GPI diagnostics [34]. In figure 7.3 both the velocity (c) and standardized flux (d) are positive, thus the blobs are on average transported radially outwards. The average radial peak velocity of the blobs is around 1200 m/s which is on the same order as the velocity calculated by the GPI data. The floating potential (b) has a negative burst for one head and a positive burst for the other head, similar results has been found for shot 011. If the other ion saturation had been used as reference both conditionally averaged floating potential waveforms would be negative. For the shots 008 and 016 the floating potential is found to have a dipole

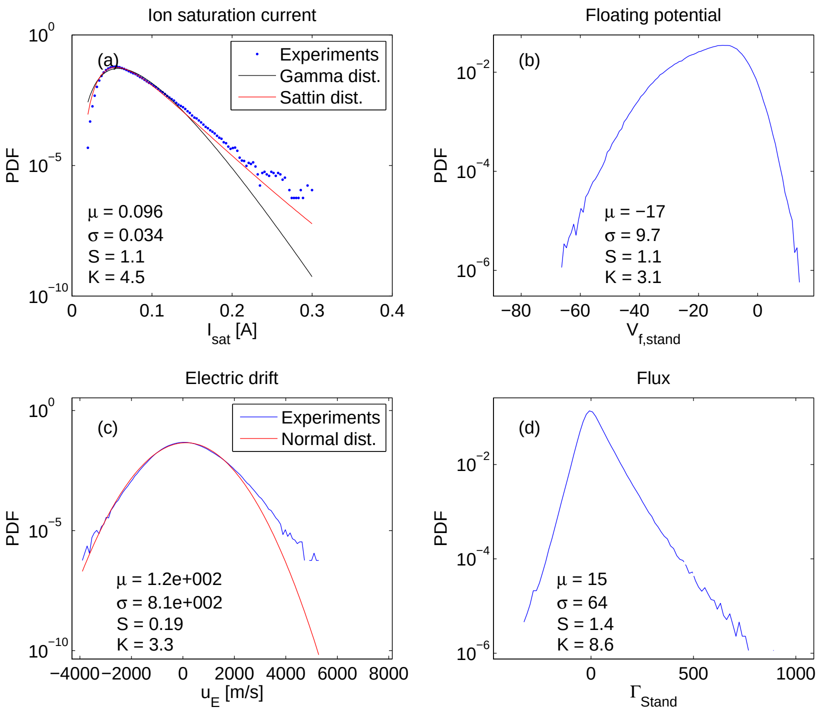

Figure 7.2 – In this figure the distributions for (a) ion saturation current, (b) standardized floating potential, (c) electric drift and (d) standardized flux are plotted. The moments are plotted on the figures, μ is the mean, σ the standard deviation, S skewness and K kurtosis. For the ion saturation current two lines has been inserted representing the gamma and Sattin distributions. For the electric drift a normal distributed fitted line has been inserted.

shape as expected from numerical simulations and theory [30]. The dipole shaped floating potential can be seen in figure 7.5, where the same calculations as figure 7.3 has been done on shot 008. A dipolar potential has also been seen previously on Alcator C-Mod, see Grulke [42]. For shot 008 the burst duration, radial velocity and flux is smaller than for shot 010. Thus less particles are transported radially. In general it has been see that that a dipolar potential is consistent with slower and shorter blobs. Thus it could be that for shot 010 and 011 the blobs are too big or radially too fast for a dipolar potential to be measured.

The amount of blobs propagating in the positive radial direction varies between the shots. For shot 010 and 011 over 90 percent of the blobs are propagating radially outwards with velocities of 1.4km/s. For shot 008 88% of the blobs propagte in the positive direction with mean velocity 1km/s, while for shot 016 only 79% propagets along the major radius with average velocity 900m/s. When more blobs propagte radially also their velocity is increased. From these calculations it could be that the blob speed and size increase with line-averaged density, consisten with the inertial velocity limit.

When collecting events for conditional averaging the events can be used to calculate waiting time and peak amplitude distributions. The distributions are calculated with a threshold 2.5σ with $I_{sat,Stand}$ as a reference in 100 bins. In figure 7.6 the complementary cumulative distribution function for (a) waiting times between events in I_{sat} (b) standardized peak values I_{sat} (c) peak value electric drift and (d) standardized peak values for the flux is plotted. From figure (a) and (b) one can see that the waiting times and peak amplitudes are exponential distributed as for the GPI data. The events seems to follow a Poisson process where each event is independent of other events. The true mean amplitude value for the non standardized signal is 0.1269 [A], approximately the same as the value found from the PDF. The electric drift amplitudes related to blob movement follow a normal distribution. From the figure one can see that the blobs propagate both inwards and outwards, as seen previously. For shot 008 and 016 where the floating potential was shown to have a dipolar shape the waiting times and peak amplitudes in (a) and (b) are not exponentially distributed. From the 15 ISP measurements, 13 is found to have exponentially distributed waiting times, where the last two is only slightly curved, all have exponential peak amplitudes. Thus the lower line-averaged density value of shot 008 and 016 is not the reason for different results.

In figure 7.7 the conditionally averaged waveforms in figure 7.3 are plotted for different threshold intervals to see how the blob statistics vary with blob density. The figure shows that the waveforms does not change with

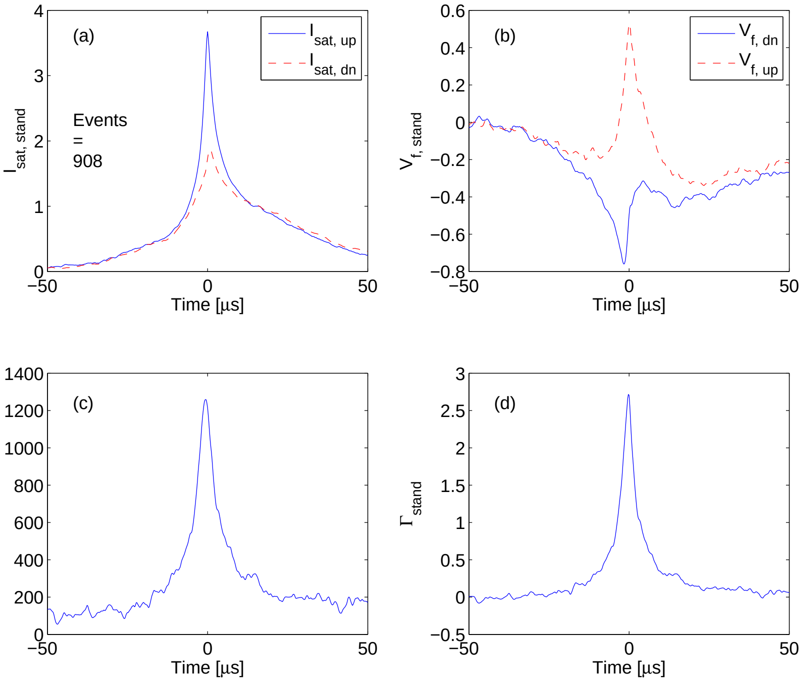

Figure 7.3 – In this figure the conditionally averaged waveforms (CAW) for shot ASP 010 are plotted for (a) standardized ion saturation current, (b) standardized floating potential, (c) electric drift and (d) standardized flux. The conditional average is calculated with the ion saturation current as reference and a threshold condition 2.5σ.

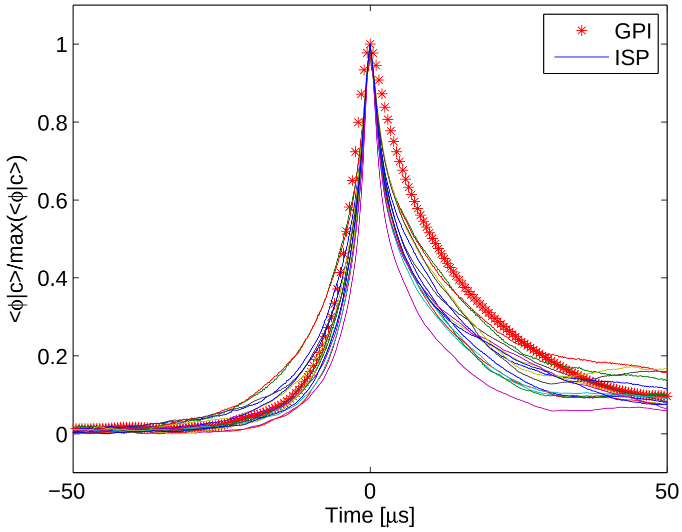

Figure 7.4 – In this figure the conditionally averaged waveforms (CAW) for 15 ISP data shots have been plotted on top of each other. All data points are taken from the SOL with line-averaged densities ranging from 0.4-1.5. The red star line is the conditionally averaged waveform found for GPI data, $n_e/n_G = 0.25$, $Z = -2.99\,\text{cm}$ and $R = 90.70\,\text{cm}$.

threshold, only the amplitude changes. Thus the duration of events is independent of the blob size, as was found for the GPI measurements. The waiting time and peak amplitude distributions have also been found to be exponentially distributed independent of the amplitude threshold. From the figure it is clear that the radial velocity (c) increases with amplitude (blob size). This is consistent with the inertial regime discussed previously where the gradient of the parallel currents are assumed to be zero.

The poloidal blob velocity can be found by dividing the distance between probes by the correlation time as done in the previous chapter. The correlation time is calculated to be $0.5\,\mu s$ and the distance between probe heads are 2.2 mm resulting in a poloidal velocity of 3.7 km/s for shot 010. This is almost four times greater than what was found from the GPI measurements. This high value might be an effect of the distance between probe heads being much smaller than the poloidal blob size.

As for the GPI data the ion saturation current is proportional to the density, in addition previous results in this section confirms similar properties. It is therefore natural to expect that the ion saturation current should exhibit long range correlations, as found in previous studies with Langmuir probes [14, 62, 92]. The autocorrelation for shot 010 is given in figure 7.8.

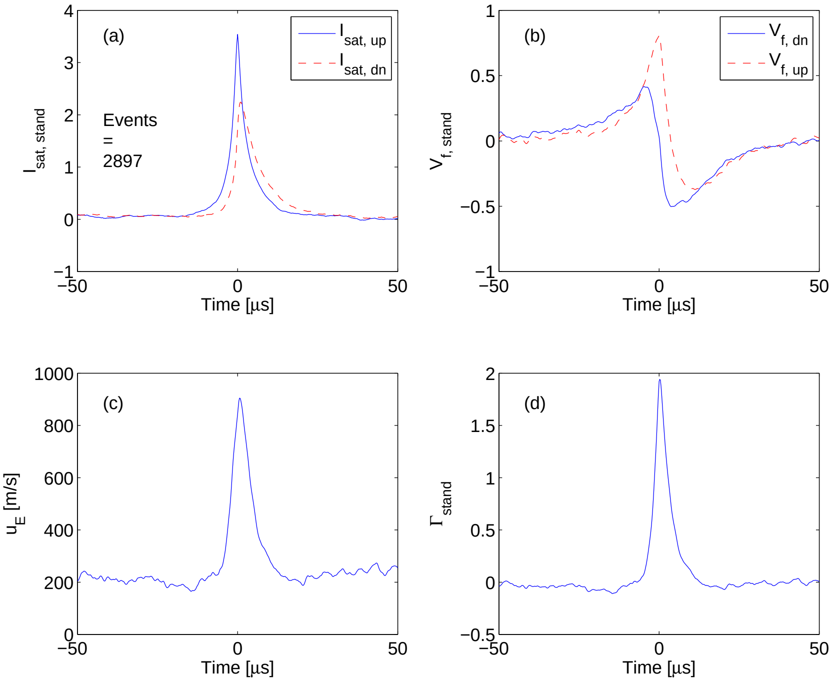

Figure 7.5 – In this figure the conditionally averaged waveforms (CAW) for shot ASP 008 are plotted for (a) standardized ion saturation current, (b) standardized floating potential, (c) electric drift and (d) standardized flux. The conditional averaged is calculated with the ion saturation current as reference and a threshold condition 2.5σ.

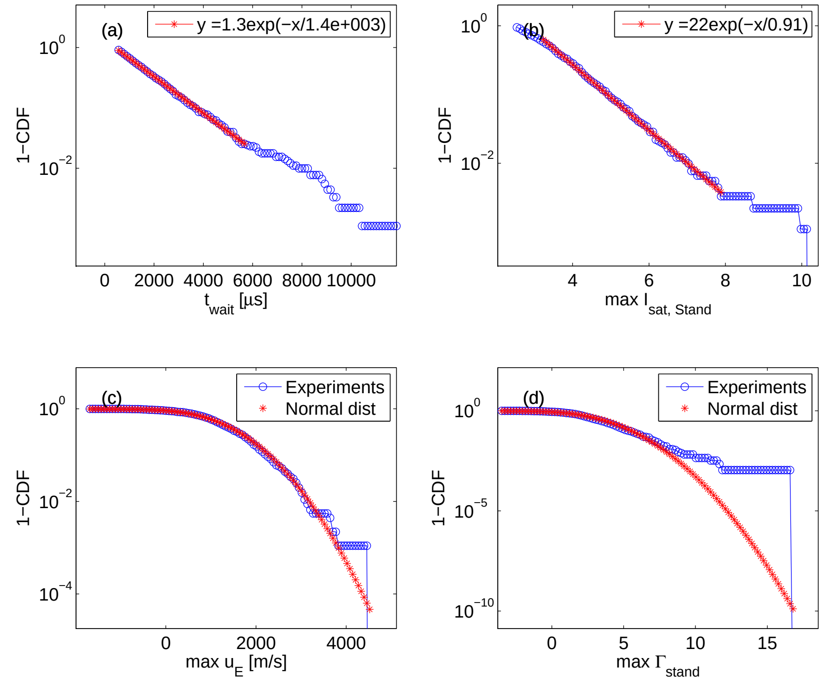

Figure 7.6 – In this figure the conditionally averaged distribution is found for (a) waiting time between events in the ion saturation current signal, (b) standardized maximum amplitudes ion saturation current, (c) maximum amplitudes electric drift and (d) standardized maximum amplitudes flux. An exponential fit has been done for the waiting time and amplitude distribution. For the velocity and flux distributions a normal fit has been inserted. The signal analyzed is the ASP shot 010.

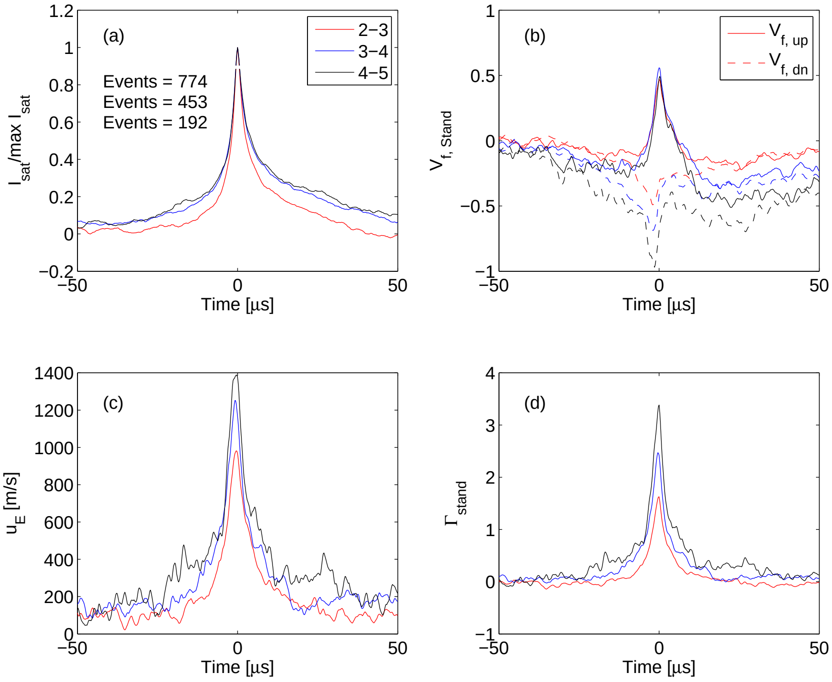

Figure 7.7 – In this figure the conditionally averaged waveform in figure 7.3 has been plotted for several amplitude intervals. The signal analyzed is ASP 010 with threshold intervals 2-3σ, 3-4σ, 4-5σ.

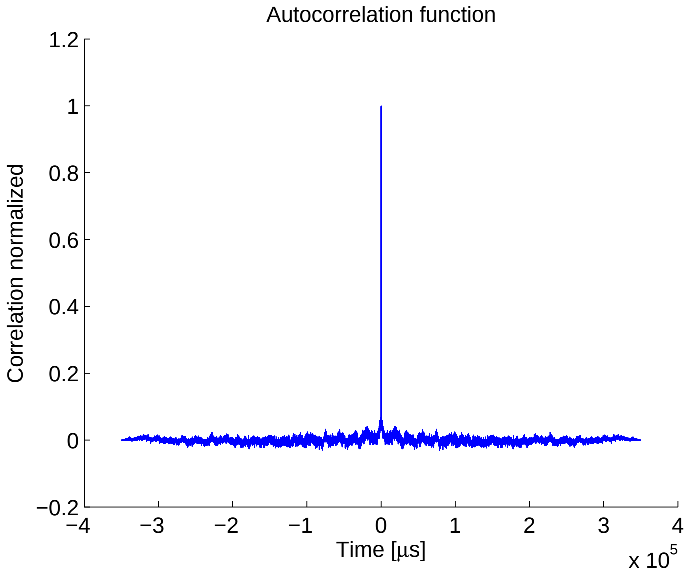

Figure 7.8 – The autocorrelation of the ion saturation current, ASP shot 010.

From the figure it is seen that the autocorrelation has small heavy tails which suggests weak long range correlations. This is expected since the measurements are from the far SOL where weak long range correlations was seen for the GPI data. The power specter for shot 010 is given in figure 7.9. From the figure the signal has $H \approx 0.5$ for long time scales, but the fitting range is less than one decade. At shorter time scales it is a fractional Brownian motion with H = 0.34. The vertical lines represent mean waiting time (red), burst duration (black) and e-folding time scale for the autocorrelation (magenta). To further verify this result the rescaled range analysis has been used in figure 7.10. From the figure the Hurst exponent is calculated to be 0.69, which is on the same order as what was found for the GPI data, in addition a data randomization has been done for verification. The fitting range covers approximately two decades. For the structure function analysis a Hurst exponent of 0.72 is found, consistent with the rescaled range analysis, but not the power specter. For shot 008 and 016 the rescaled range analysis, structure function and wavelet analysis does not have a power law region. Shot 011 looks approximately as shot 010 with H_{RR} = 0.68 and H_{SF} = 0.63. The power specter gives a Hurst exponent close to 0.5 for all shots, but only one decade is fitted. The wavelet method does not have a power law region for any of the shots. Four different methods for calculating the Hurst exponent gives four different answers. Similar results are found from the ISP data, the estimates are slightly curved and the different methods give different results. The rescaled range and structure functions give similar results, but the result is highly fluctuating as a function of line-averaged

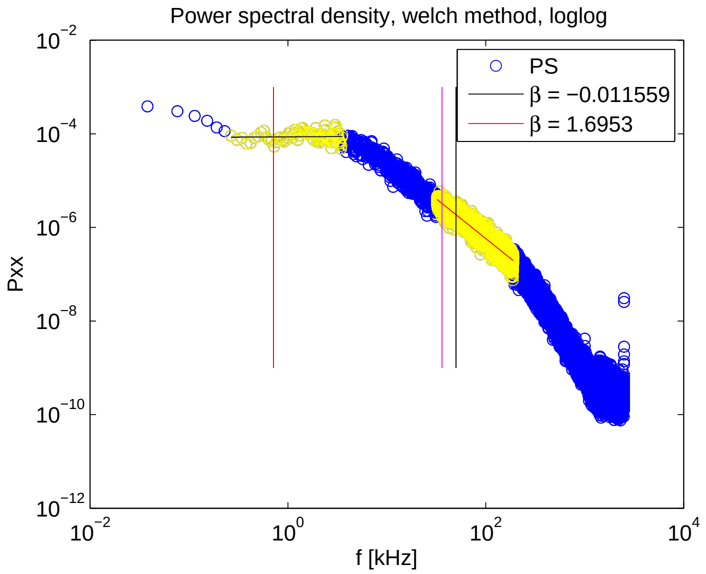

Figure 7.9 – The power spectral density of ion saturation current, ASP shot 010. A fit has been done on both long and medium time scales. Three vertical lines has been inserted representing mean waiting time (red), e-folding time (magenta) and mean burst duration (black).

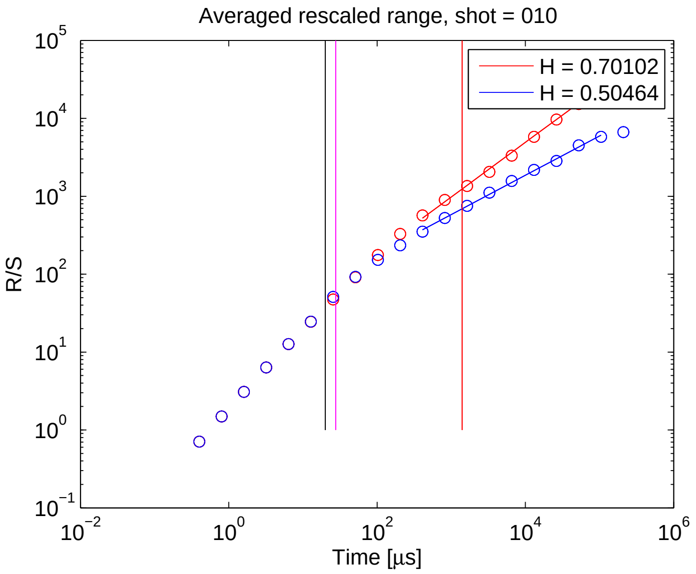

Figure 7.10 – Rescaled range for ion saturation current. The red dots are RR on regular signal while the blue is data randomized signal. Three vertical lines has been inserted representing mean waiting time (red), e-folding time (magenta) and mean burst duration (black).

density. It could be that the data acquisition method effects both the long range correlations and the conditionally averaged waveform. Another reason could be the high line-averaged density for the probe data compared to the GPI data. For the highest line-averaged density in the GPI measurements it was found that the variance of wavelet coefficients was slightly curved in the SOL. Thus it could be that since the probe data have even higher line-averaged density the wavelet estimation method does not work. Stationarity have been tested with the structure functions and found to be valid for all measurements.

Chapter 8

Results Stochastic Model

In this chapter statistical analysis will be done on realizations of the stochastic model introduced in the theory. The importance of this chapter is to analyze the methods when bursts overlap.

8.1 Signal

The signal is made using the stochastic model explained in the theory, the matlab code can be found in the appendix. All signals have $l = \tau_r/\tau d = 0.18$, approximately the value found for the GPI measurements. The signal length is $N = 4000000$ with $dt = 10^{-2}$. In figure 8.1 realizations are plotted for different values of the intermittency parameter γ. The intermittency parameter is as before defined as,

$$\gamma = \frac{\tau_r + \tau_d}{\tau_w}. \tag{8.1}$$

For the realizations used here τ_d and τ_r are kept constant, thus an increase of the intermittency parameter is a decrease of the average waiting time τ_w. From the figure it is seen that as γ increases the individual bursts are harder to separate because of overlap. The signals is as before standardized.

8.2 Autocorrelation and power specter

The autocorrelation of four realizations is given in figure 8.2. From the figure one can see that the autocorrelation does not have heavy tails, which is expected for a memoryless process such as a Poisson process. This does not change as a function of γ. The power specter of the stochastic model is given in figure 8.3. For low frequencies the power specter is flat with a β value close to zero, consistent with uncorrelated white noise. For short time scales the β values are well above the fBm limit, as seen for the GPI data.

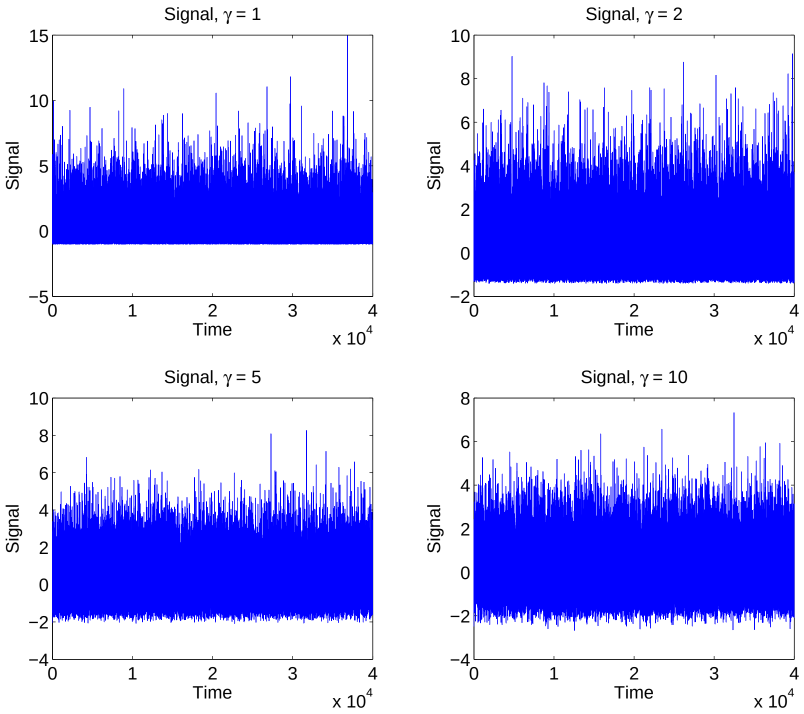

Figure 8.1 – The figure shows signals plotted for four realizations with different values of the intermittency parameter γ.

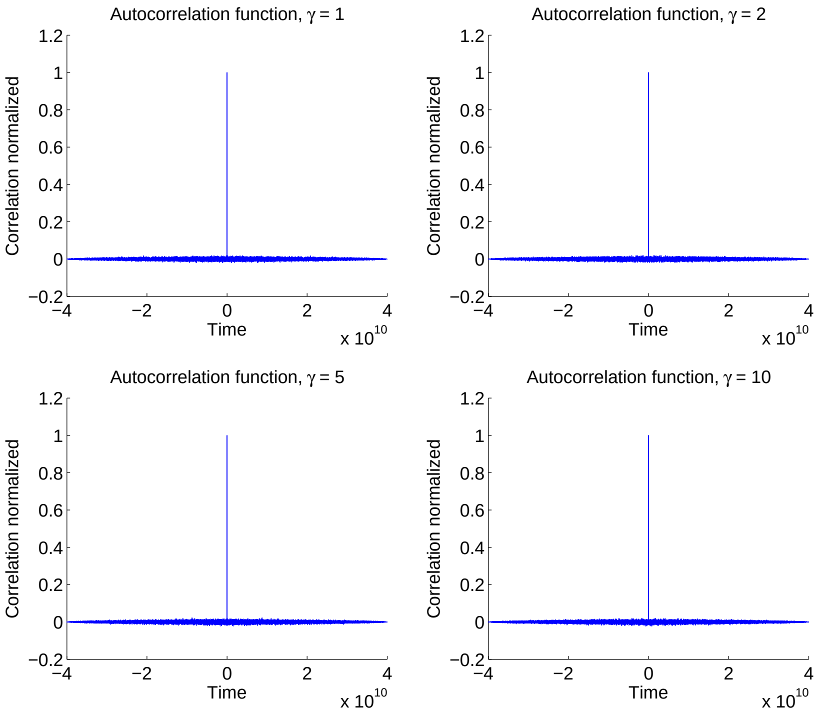

Figure 8.2 – Autocorrelation for stochastic model realizations with different values of γ.

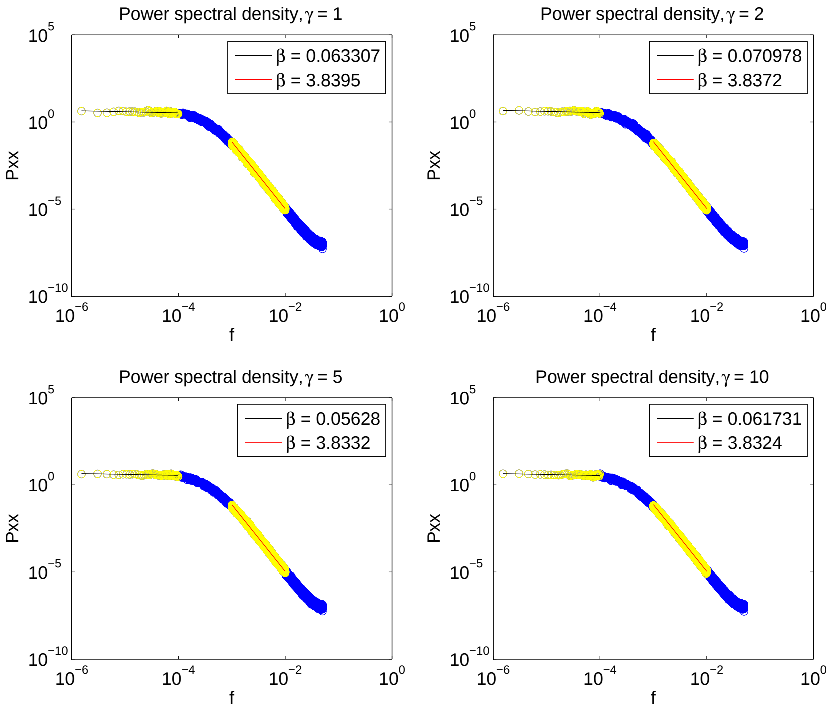

Figure 8.3 – Power specter for stochastic model realizations with different values of γ.

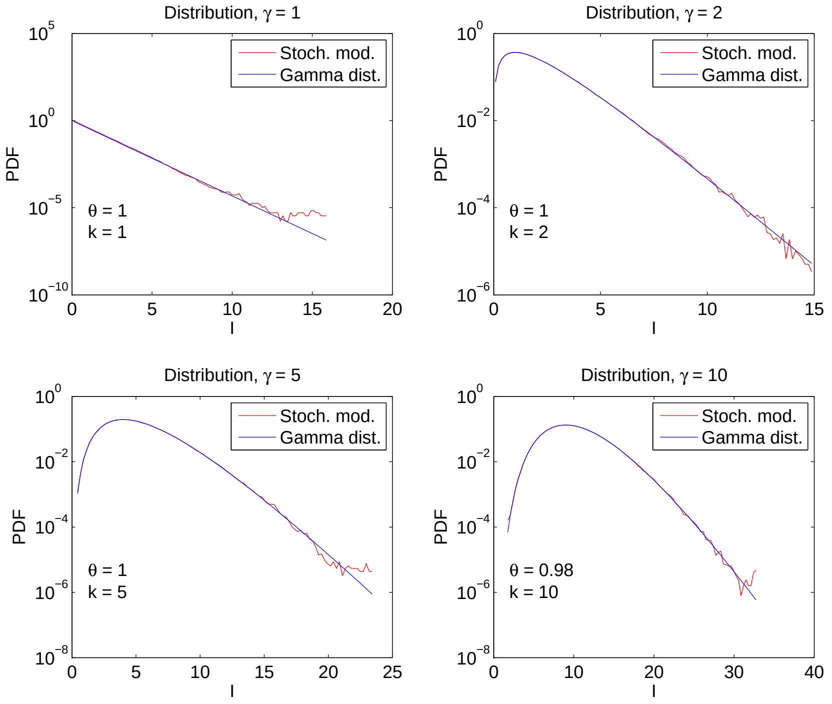

Figure 8.4 – Distribution of the stochastic model fitted by a gamma distribution for realizations with different values of γ.

8.3 Distribution of signal amplitudes

The stochastic model predicts a gamma distribution for the generated signal, see figure 8.4. The distribution can only be plotted for $\gamma \geq 1$ since lower values has too many points close to zero. When γ increases the distribution goes towards a Gaussian distribution, S and K goes towards 0 and 3 for large γ. In the figures the scale θ and shape k parameters are also given. The realizations was made with $\langle A \rangle = 1$, thus the exact values of the model is returned independent of γ.

8.4 Conditionally averaged waveform

The conditionally averaged waveform is calculated using the method which favors high tops and no overlap. The threshold condition used is 2.5σ. In figure 8.5 the conditionally averaged waveform is plotted for γ values from 0.1 to 10. When γ increases the rise time increases while the decay time stays approximately the same. Thus an increase of γ gives a more symmetric waveform. In the numerical simulation of the model the rise and decay times

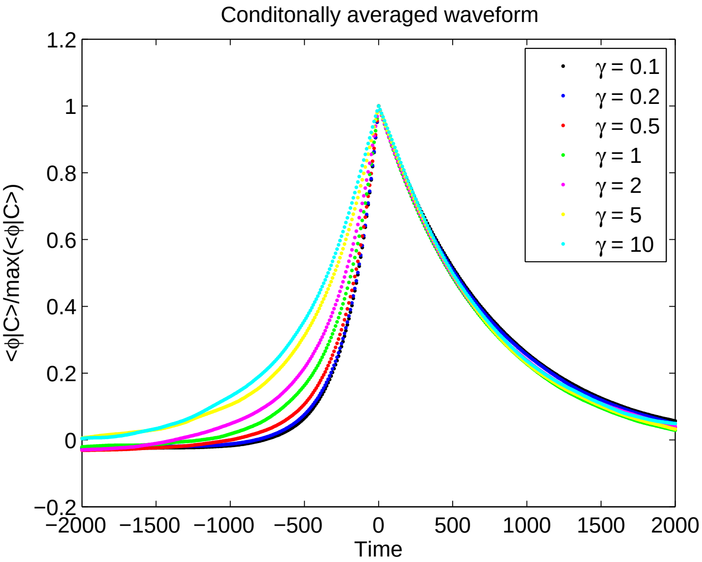

Figure 8.5 – Conditional windows for stochastic model realizations with different values of γ

are defined by the normalized function $l = \tau_r/\tau_d$. For $\gamma = 0.1$ the values is calculated to 0.26 while the theoretical value was 0.18. Since the raise time increases for increasing γ, the true l can not be found. The increased rise time for increased γ is seen because the rise time is more sensitive to overlapping bursts than the decay time. A small blob on the right side will effect the value very little while a small blob on the left side will have a large impact. It should be mentioned that in the way the conditionally averaged waveform is calculated all overlapping events are smaller.

Since the waveform becomes more symmetric with increasing γ, the increased waiting time in the SOL from the GPI measurements is most likely due to the acquisition method. For the GPI measurements γ decreases in the SOL, but the average waveform does not change. Therefore the waiting time in the SOL is the same for all radial positions and line-averaged densities.

8.5 Waiting time statistics

The complementary cumulative distribution for waiting times has been calculated both for the method with overlap as well as the method without overlap. A comparison of the two methods for one single gamma value is given in figure 8.6. In the figure the distribution for waiting times of a signal with $\gamma = 2$ and 80000 bursts is plotted. The conditional average has been

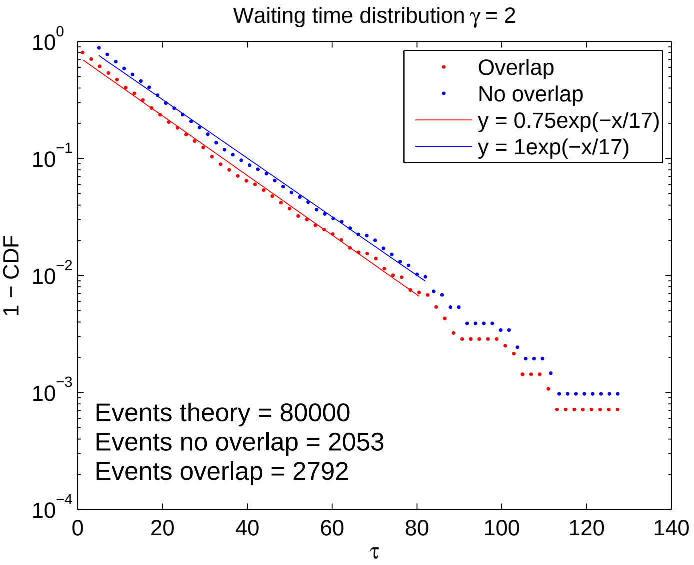

Figure 8.6 – The figure compares waiting time distribution for two conditional averaging methods. The threshold condition used is 2.5σ and the signal has $\gamma = 2$ with 4000000 data points, $dt = 10^{-2}$.

sampled by a threshold condition of 2.5σ. From the lower left corner in the figure one can see that only a tiny fraction of the 80000 theoretical bursts are sampled. This low value is partly due to overlapping bursts above the threshold and also because many of the events are under the threshold. In the figure it is seen that the distribution is exponential and an exponential fit has been given in figure. The fit suggests an average waiting time of 17, which is quite far from the theoretical value $\tau_w = 0.5$. The difference reflects the amount of bursts sampled compared to the theoretical number of bursts. The expected number of events above the threshold can be calculated by,

$$E[N(X > 2.5)] = N \cdot p(X > x) = N \cdot \exp(-2.5/\langle A \rangle). \qquad (8.2)$$

Where $\langle A \rangle = 1$ has been used. Thus for $\gamma = 2$ the expected number of events sampled when there are no overlap is 6567 events. So when $\gamma = 2$ about two thirds of the events are lost due to overlap.

8.6 Amplitude statistics

The conditional amplitude distribution for both averaging methods is given in figure 8.7. In the figure the signal has $\gamma = 2$ and the threshold used is 2.5σ. From the figure it is seen that the amplitudes follow an exponential distribution and a fit has been inserted to verify this. The fit suggest an average amplitude of one which is the exact value of the generated data. But

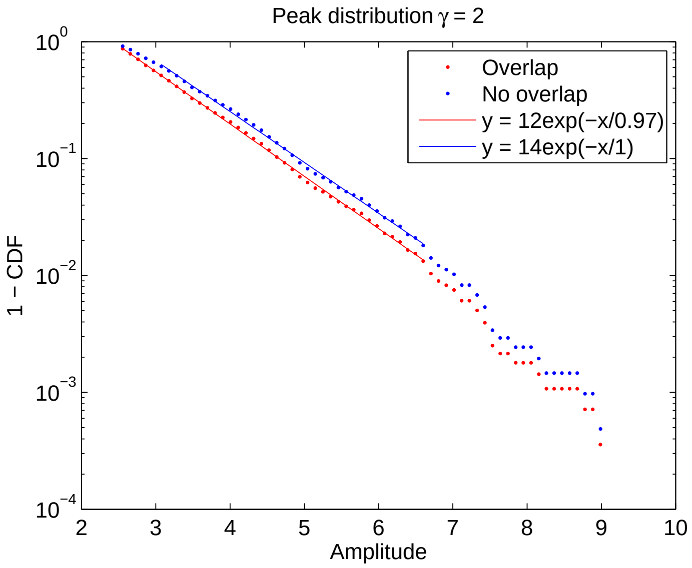

Figure 8.7 – The figure displays conditional amplitude distributions calculated with both methods. The conditional data has been sampled by a threshold condition 2.5σ and the realization has $\gamma = 2$.

since the signal used is the standardized, the true mean amplitude has to be changed by multiplying by the standard deviation and adding the mean value. For $\gamma = 2$ this gives a mean amplitude value of 3.4, much larger than the theoretical value of 1. In general the standardized mean amplitude decreases for increasing γ and the unstandardized amplitude increases for increasing γ. This result is expected since overlap leads to increased amplitudes. This explains the result seen for the GPI data where the mean standardized amplitude decreased with increasing γ. The mean conditional amplitude of the GPI data can not be used to say anything about the blob size, it is just caused by a change of γ, which seems to be caused by the diagnostics. For large waiting times, small γ, an amplitude value close to the theoretical value can be found, $\gamma = 0.5$ gives $\langle A \rangle = 1.7$. Thus for large γ the mean amplitude of the model, $\langle A \rangle$, is best found from the PDF of the signal.

8.7 Long range correlations

The shot noise process is by definition a Poisson process, which is memoryless with an expected Hurst exponent 0.5. In figure 8.8 the rescaled range analysis is done on a signal with four different γ values. The rescaled range analysis gives a Hurst exponent slightly above 0.5.

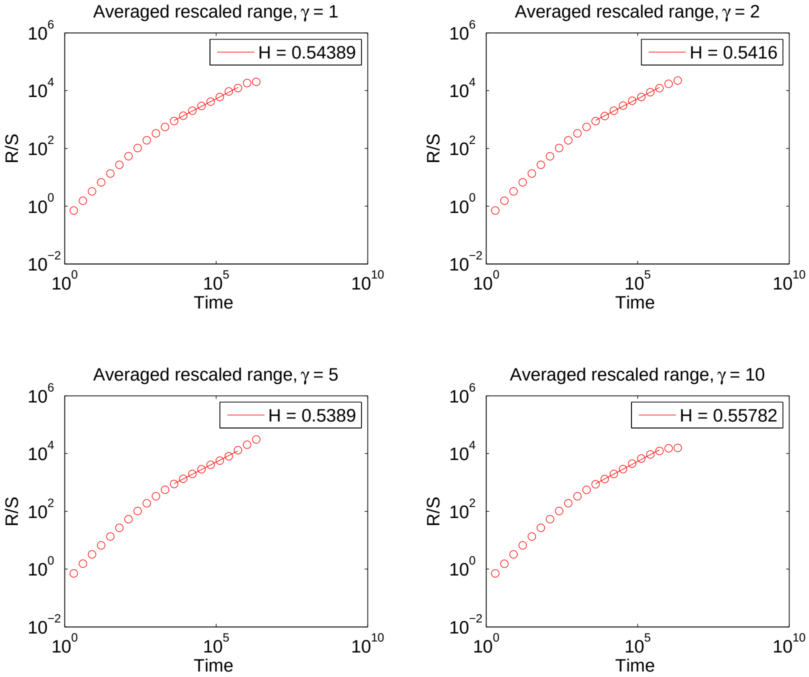

Figure 8.8 – Hurst exponent calculated by rescaled range analysis for four realizations of the stochastic model with different γ values.

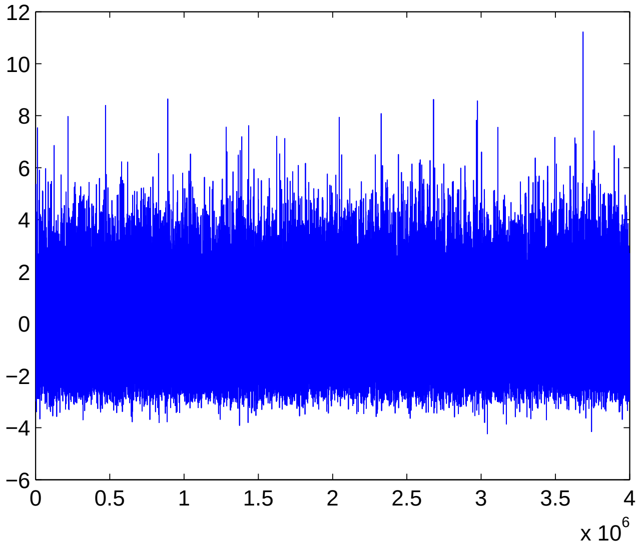

Figure 8.9 – Superposition of a fGn and a shot noise process. Both signals has mean zero and standard deviation 1. The Hurst exponent of the fGn is 0.85. The shot noise has $\gamma = 1$.

8.8 In relation to SOL measurements

The GPI results suggest that even while the blobs are independent of each other a significant Hurst exponent is found in the SOL. A possible explanation for the high Hurst exponents could be that the signal is a superposition between a shot noise process defined by the stochastic model and a fGn. Where the fGn process is related to mechanisms in the edge region transported into the SOL by the blobs. In figure 8.9 a superposition between a shot noise and a fGn is plotted. In this figure the two signals has equal standard deviation one and zero mean. The fGn has a Hurst exponent of 0.85, which is close to the value seen in the edge region. The shot noise has $\gamma = 1$. In figure 8.10 the Hurst exponents are estimated by rescaled range and structure function analysis for superposition processes with different γ values. Each Hurst exponent has been calculated ten times for each γ value and averaged, the error bars represent the standard deviation. From the figure it is clear that the non persistent bursts acts as to lower the overall Hurst exponent. The Hurst exponents have quite high standard deviation and covers the values seen in the SOL. It should be mention that the GPI measurements suggest a fluctuating part smaller than the shot noise process.

In figure 8.11 the Hurst exponent estimated by the rescaled range analysis of a combined signal is plotted as function σ_{fGn}/σ_{SN}. Where σ_{fGn} and σ_{SN} are respectively the standard deviation of the fGn and shot noise process.

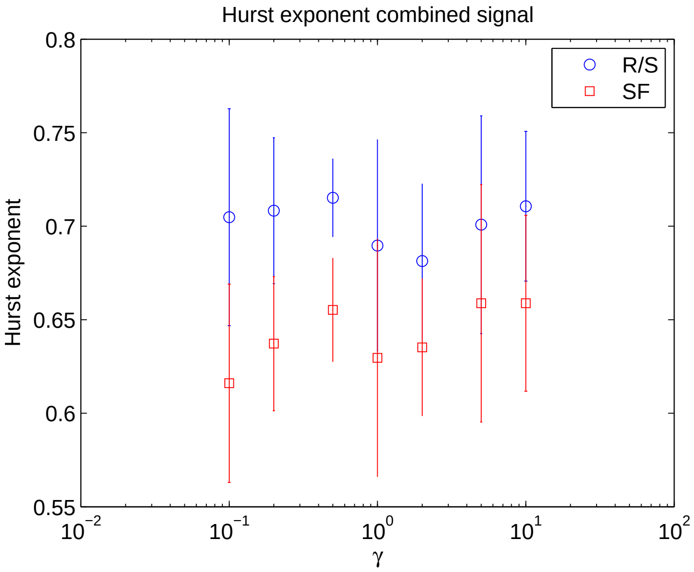

Figure 8.10 – Hurst exponents calculated by rescaled range and structure functions for a signal consisting of a superposition between a fGn and a shot noise. Both signals have mean zero. The fGn has $H = 0.85$ and the shot noise has $\gamma = 1$.

The fGn has a theoretical Hurst exponent of 0.85 and the shot noise generated has $\gamma = 1$. In the figure it is shown that up to about $\sigma_{fGn}/\sigma_{SN} = 0.5$ the fGn does not effect the Hurst exponent. For $\sigma_{fGn}/\sigma_{SN} > 10$ the signal is dominated by the fGn. In order for a a signal which consist of a superposition between a fGn and shot noise to have long range correlation, they have to have at least equal magnitude, while for the experimental data $\sigma_{fGn}/\sigma_{SN} \approx 10^{-2}$.

Another way to test the superposition is by looking at the distribution of the signal. When calculating the distribution for the GPI data previously it was found that for the lowest line averaged densities the gamma distribution was in most cases not a good fit. The reason for the poor fit was that it failed to fit the tails. In figure 8.12 the PDF of a superposition between a fGn and a shot noise process is plotted together with the PDF of a GPI signal at $R = 90.31\,\text{cm}$, $Z = -2.99\,\text{cm}$ with $n_e/n_G = 0.20$. The shot noise process has $\gamma = 2$, $\sigma = 0.35$ and $\mu = 0.5$. The fGn has $H = 0.85$, $\sigma = 0.0493$ and $\mu = 0.27$. From the figure it is clear that the combined signal is almost a perfect fit to the signal while the gamma distribution is quite poor. Thus this could indicate that a superposition might be possible in some form. In relation to the Hurst exponent this does not explain the high values seen in the SOL because $\sigma_{fGn}/\sigma_{SN} = 0.14$ which from figure 8.11 should not give any significant change of Hurst exponent.

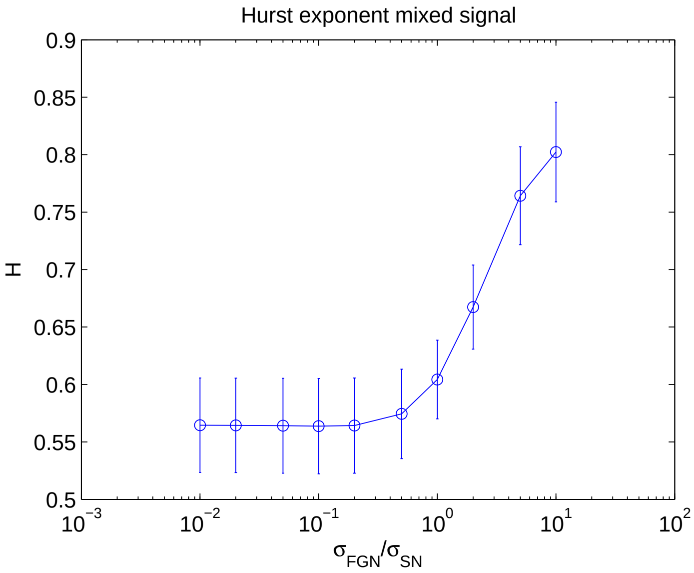

Figure 8.11 – In this figure the Hurst exponent of a signal consisting of a shot noise and a fGn is plotted for different values of σ_{fGn}/σ_{SN}. The Hurst exponent is calculated by the rescaled range method. The fGn has $H = 0.85$, and the shot noise has $\gamma = 1$.

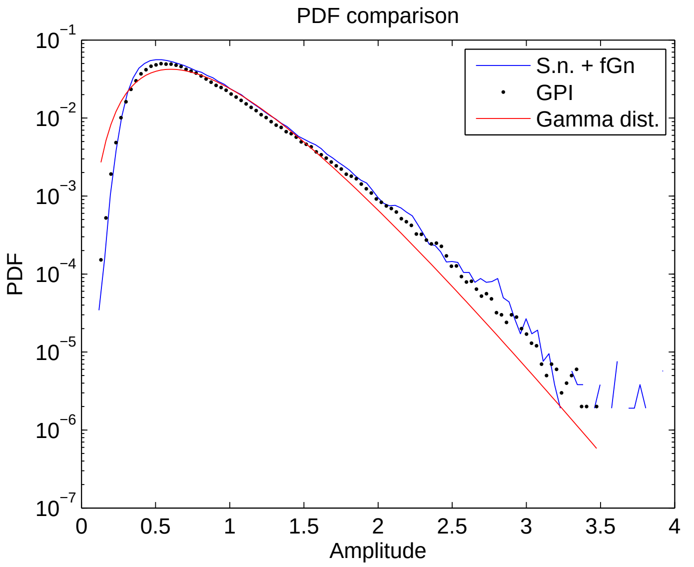

Figure 8.12 – In this figure the PDF of a signal measured by the GPI diagnostics at $R = 90.31$cm, $Z =$ -2.99cm with $n_e/n_G = 0.20$ is plotted. The PDF is fitted by a gamma distribution red line with $k = 4.6$ and $\theta = 0.17$. The distribution is also fitted by a blue line, the PDF of a superposition between a fGn and shot noise process.

Chapter 9

Summary and conclusion

The large amplitude events in plasma fluctuations close to the walls in Alcator C-Mod have been studied. In this chapter all results from GPI, Langmuir probes and stochastic model will be summarized and compared.

9.1 Signal

GPI measurements have been analyzed as a function of line-averaged density and major radius. It was found that the signals are dominated by burst-like shapes in the SOL. The waveforms have a fast rise and a slower decay. The bursts have much larger amplitudes than the standard deviation and they are only positive. For the edge region a first look on the signals reveals seemingly random fluctuations around the mean value. Thus the blobs are generated near the separatrix.

For the probe data the ion saturation current show a similar shape as the GPI data in the SOL. The signals have characteristic shapes with amplitudes much larger than the standard deviation. The floating potential looks like random fluctuations around the mean value.

9.2 Probability density functions

For the GPI data it was found that the PDF vary with radial position and line-averaged density. In the edge region the PDF was found to be well fitted by a slightly skewed and peaked gamma distribution. In the SOL the skewness and kurtosis was found to increase with major radius and decreasing line-averaged density. The high skewness and kurtosis was caused by large density fluctuations, blobs. For small values close to the separatrix the gamma distribution was found to be the best fit as proposed by the stochastic model. For larger values of skewness and kurtosis it was found that the Sattin distribution derived from SOL equations was the best fit.

For the highest values of skewness and kurtosis none of the distributions provided a good fit. The result is most likely effected by the temperature dependence of the diagnostics. The change of PDF from edge to SOL is another confirmation of blob generation near the separatrix.

Between skewness and kurtosis a parabolic relations was found, close to the value expected by the stochastic model. Between the other moments no particular relation was found.

For the probe data the ion saturation current shows a similar fit with gamma and Sattin distribution as the GPI data. All probe data is located at the same radial position, therefore the radial dependence of the GPI measurements can not be verified. The floating potential were found to be slightly skewed, with $S \approx 1$ and $K \approx 3$. The radial velocity was found to be Gaussian distributed, while the particle flux has a very sharp tail towards positive values caused by large blob transport.

9.3 Conditionally averaged waveform

The conditionally averaged waveform for GPI measurements in the edge region was found to have a high reproducibility. The waveform is dependent on amplitude, line-averaged density and radius. Thus there is no characteristic waveform related to the mechanisms in the edge region. In the SOL, the GPI measurements shows a characteristic waveform equal for all amplitudes, line-averaged densities and radial positions. The waveform has a sharp exponential rise and a slower exponential decay. The average blob duration is $20 - 25\,\mu$s. The similar waveform for all radii and line-averaged densities indicate that the blob frequency does not change. Therefore the increased background turbulence makes the blobs less significant for increased line-averaged density [3]. This confirms the decreasing skewness and kurtosis with increased line-averaged density.

For the ASP (1111208) probe data the conditionally averaged waveform has a sharp rise and a trailing wake, but exponential rise and decay is not suitable. The duration was found to vary between $10 - 20\,\mu$s. For the ISP (1120210) data the waveform is almost universal as a function of line-averaged density. All probe conditionally averaged waveforms have a sharper peak and a more symmetric conditionally averaged waveforms than the GPI equivalents, which can be due to the diagnostics. The floating potential shows a dipolar shape for small slow blobs, while for larger faster blobs the floating potential has a burst-like shape.

9.4 Waiting time distribution

The waiting times between bursts were found to be exponentially distributed both for the GPI and Langmuir probe measurements. This suggests that blobs are independent events described by a Poisson process. It was found that even while the overlapping conditional averaging method returns twice as many bursts the average waiting times were the same for both methods. With the use of the stochastic model it was found that only a tiny fraction of the actual number of bursts are collected due to threshold and overlap. The true mean waiting time can not be retrieved from the data. For the ASP (1111208) measurements only the measurements with large fast blobs have exponential waiting times. For the ISP (1120210) all measurements were found to have more or less exponential distributed waiting times. The line-averaged density does not effect the exponentially distributed waiting time. For the GPI data it was found that there are more blobs close to the separatrix, the stochastic model showed that this might be caused by the GPI diagnostics.

9.5 Peak amplitude distribution

The peak amplitudes were found to be exponentially distributed for both the GPI data and the probe data. From the GPI data it was found that the mean standardized peak amplitude increased with major radius and decreasing line-averaged density. This was found to be a result of decreased mean value towards the wall.

9.6 Long range correlations

The Hurst exponent was estimated on computer generated fGns. It was found that the power specter, structure function and rescaled range have a slight bias, while the wavelet method measured H perfectly. The rescaled range and the structure functions analysis have much larger error in the estimate than the power specter and wavelet methods. The autocorrelation was found to verify long range correlations by heavy tails. It was found that an amplified part in the signal does not alter the Hurst exponent. The structure function analysis was found to be very sensitive to trends, where only a slight trend alter the result completely. The other methods were found to change only when the trend had a period less than, or equal to the fitting region and a magnitude larger than the signal itself.

For the GPI measurements the Hurst exponents increase with line-averaged density in the SOL. The Hurst exponent in the SOL varies from $0.6 - 0.7$. Since the blobs were found to be independent the large Hurst exponent in the SOL is not likely caused by the blobs. The increase of the Hurst exponent with increasing line-averaged density in the SOL could be due to increased blob size in the SOL. A large blob is able to carry more of the long range correlated processes in the edge region into the SOL [3]. In the edge region the Hurst exponents was found to increases away from the separatrix. The Hurst exponent in the edge region varies from approximately 0.6 at the separatrix to $0.8 - 0.9$ at the innermost measurement.

The probe data gives different values of the Hurst exponent with the different methods. The rescaled range and structure function analysis returns values close to those found for the GPI measurements, the power specter results thus not coincide with the other methods and cover only one decade. The wavelet method seems to curve with increasing line-averaged density for the GPI measurements, making it useless for the high line-averaged density probe measurements.

9.7 Velocity

The radial velocity was calculated for both probe data and GPI data and found to be approximately 1000m/s. The magnitude suggests a solution where the blob is driven by both perpendicular and parallel currents with non zero vorticity, as analyzed in Kube and Garcia [50]. For the GPI measurements the radial velocity increases towards the separatrix and slightly with line-averaged density. The result suggests a deacceleration of the blobs in the SOL, most likely caused by non linear dispersion. The poloidal velocity increase with line-averaged density with magnitude $1 - 3\,\mathrm{km/s}$.

For the probe data the radial velocity was found to increase with the blob size as for the inertial scaling closure. For the probe it was found that for high line-averaged density, over 90% of the blobs have positive velocites. For decreasing line-averaged density it was found that both the mean velocity of positiv propagating blobs and the percentage of positive propagating blobs decrease. The poloidal velocity found by probe data also shows increased magnitude compared to the radial velocity.

9.8 Blob size

For the GPI data the poloidal blob size was found for all line-averaged densities, and major radius in the SOL by conditional averaging. An average poloidal blob size $\ell = 1 - 2\,\mathrm{cm}$ was found independent of line-averaged density and major radius. For the probe data it was found that for increasing line-averaged density both the velocity and duration increased, thus the blobs must be larger. It should be mentioned that the small duration found for the lowest line-averaged density of the ASP (1111208) measurements are not consistent with the ISP measurements. Therefore the ASP session should be analyzed further to check if the session is valid.

9.9 Stochastic model

For the stochastic model the distributions were found to be gamma distributed with the exact parameters provided by the model independent of γ. The conditionally averaged waveform becomes more symmetric when γ increases, caused by rise time more sensitive to overlap than the decay time. The result shows that the increase of γ for the GPI measurements in the SOL is most likely caused by the diagnostics. The waiting times and peak amplitudes were found to be exponentially distributed, but the returned values are not those of the model. The result explains the increased waiting times and amplitudes found for the GPI measurements as a function of γ.

Since the blobs were found to be independent of each other an underlying process must be the source of the Hurst exponent. A superposition of a fGn and a shot noise process has been found to fit the distribution where the gamma distribution could not. For the same signal it was found that the contribution by the fGn was to small to significantly influence the Hurst exponent estimate. It was found that in order for the fGn to influence the Hurst exponent the fGn must be of the same order or greater than the shot noise. In addition it was found that the influence by the shot noise does not depend on the value of γ. The stochastic model seems to recreate the GPI measurements close to the separatrix. Far away from the separatrix the diagnostics seems to destroy the fit with the stochastic model.

9.10 Conclusion

For the GPI data the SOL consist of signals dominated by burst events. The results shows that the blobs are likely generated at or near the separatrix. These events have exponentially distributed waiting times and peak amplitudes, consistent with a Poisson process. The blob dominated signals have a characteristic waveform independent of line-averaged density, amplitude and major radius. Therefore the stochastic model should be a perfect fit for the measurements. The long range correlations in the SOL were found to be unrelated to blob structures. Thus the blobs can not be explained by SOC.

It was found that the Hurst exponents increase in the SOL with line-averaged density. This is assumed to be due to more long range correlated process being transported into the SOL when there are more particles. The Hurst exponent in the SOL reveals the possibility of another process in addition to the Poisson process. For the probe data the long range correlation analysis is inconclusive. The rescaled range analysis and structure function analysis gives similar results as found for the GPI data for most of the probe measurements. The wavelet analysis does not have a power law region and the power specter gives varying results. These result might be an effect of the acquisition method or the high line-averaged density. For ASP probe measurements the blob velocities were found to increase with size and line-averaged density, consistent with an inertial velocity scaling. The velocity magnitudes were consistent with a mixture of MHD instabilities, i.e. kink and ballooning. For GPI measurements the poloidal size of blobs were found to be independent of line-averaged density and major radius.

In summary the GPI results show that the blob duration, waiting time and poloidal size is independent of line averaged density, while the radial velocity and Hurst exponents increase with line-averaged density. In addition the importance of blobs compared to the background were found to decrease as the line-averaged density increased.

9.11 Further work

In order to extend the results found in this thesis the following projects should be investigated further:

- Redefine the stochastic model so it can include a background process able to reproduce the Hurst exponent seen in the SOL.
- The ASP (1111208) measurements should be analyzed further to see if a new session must be taken due to varying results, not in agreement with the GPI and ISP (1120210) measurements.
- More thorough investigation of dominant blob velocity closures, analyze the magnitude of each term in the current continuity equation for the velocities found.
- GPI data with line-averaged density on the same order as the probe data should be analyzed.
- More thorough denoising of the data, try to separate the shot noise process from the long range temporal correlated processes.
- Test robustness of the stochastic model to see if other amplitude and waiting time distributions can return exponential distributions when γ varies.
- ISP (1120210) measurements should be analyzed further to see the effects of line-averaged density.

Appendix A

List of abbreviations

- AC - Autocorrelation
- CDF - Cumulative distribution function
- fBm - fractional Brownian motion
- fGn - fractional Gaussian noise
- GPI - Gas puff imaging
- H - Hurst exponent
- ITER - International Thermonuclear Experimental Reactor
- K - Kurtosis
- MHD - Magnetohydrodynamics
- MIT - Massachusetts Institute of Technology
- PDF - probability density function
- PS - Power specter
- r - Reproducibility
- R - Major radius
- RR - Rescaled range
- r.v. - Random variable
- S - Skewness
- SF - Structure functions
- SN - Shot noise

- SOC - Self-organized criticality
- SOL - Scrape-off layer
- Z - Vertical position
- μ - mean value
- σ - standard deviation

Appendix B

Bohm criterium

In this appendix the Bohm criterium is derived. The Bohm criterium gives a minimum value the velocity must have to overcome the sheath potential barrier. The derivation done here follows Stangeby [86] closely. At the sheath edge the electrons are in force balance between a pressure gradient force, $F_p = T_e \nabla n_e$, pushing the electrons towards the surface and a repelling potential force, $F_\phi = e n_e \nabla \phi$. Integrating gives the Boltzmann relation for the electrons,

$$n_e = n_0 \exp\left[e\left(\phi - \phi_0\right)/T_e\right]. \tag{B.1}$$

Where n_0 is the electron density at the sheath, ϕ_0 is the electrostatic sheath potential, e is the elementary charge and T_e is the electron temperature. For simplicity cold, collisionless ions will be assumed, the equation of motion along $\mathbf{B}$ can then be written as,

$$M\frac{du}{dz} = -e\frac{d\phi}{dz}. \tag{B.2}$$

Where M is the ion mass and u is the velocity. Integrating this equation gives,

$$\frac{1}{2}Mu^2 = -e\phi. \tag{B.3}$$

Ion density is assumed to be kept constant in time by a delta function source and the generated ions have zero velocity. The ion continuity equation then reduces to,

$$n_i u = \text{constant}. \tag{B.4}$$

An equation for the ion density as a function of the potential can now be written as,

$$n_i = n_0 \left(\frac{\phi_0}{\phi}\right)^{1/2}. \tag{B.5}$$

This equation together with the electron density equation can now be put into the one dimensional Poisson's equation,

$$\begin{aligned}
\frac{d^2\phi}{dx^2} &= -\frac{e}{\epsilon_0}\left(n_i - n_e\right) \\
&= -\frac{en_0}{\epsilon_0}\left[\left(\frac{\phi_0}{\phi}\right)^{1/2} - \exp e(\phi-\phi_0)/T_e\right] \\
&\approx -\frac{en_0}{\epsilon_0}\left[\left(\frac{\phi+\Delta}{\phi}\right)^{1/2} - \left(1-\frac{e\Delta}{T_e}\right)\right] + \vartheta(\phi^2) \\
&\approx -\frac{en_0}{\epsilon_0}\left[1 - \frac{1}{2}\frac{\Delta}{|\phi_0|} - \left(1-\frac{e\Delta}{T_e}\right)\right] + \vartheta(\phi^2) \\
&= -\frac{en_0}{\epsilon_0}\left[-\frac{1}{2}\frac{\Delta}{|\phi_0|} + \frac{e\Delta}{T_e}\right] + \vartheta(\phi^2) \\
&= -\frac{en_0\Delta}{\epsilon_0}\left[\frac{e}{T_e} - \frac{1}{2}\frac{1}{|\phi_0|}\right] + \vartheta(\phi^2), \\
\frac{d^2\Delta}{dx^2} &\approx \frac{en_0\Delta}{\epsilon_0}\left[\frac{e}{T_e} - \frac{1}{2}\frac{1}{|\phi_0|}\right] + \vartheta(\phi^2),
\end{aligned} \tag{B.6}$$

In the equation above Δ is defined as,

$$\Delta = \phi_0 - \phi. \tag{B.7}$$

The region considered is just inside the sheath, $\Delta \ll 1$, $\Delta > 0$. If the term in the parenthesis of equation (B.6) is less than zero the solution is oscillatory which have never been seen in experiments [86], thus,

$$\begin{aligned}
\frac{e}{T_e} &\geq \frac{1}{2|\phi_0|} \\
u_0 &\geq C_s
\end{aligned} \tag{B.8}$$

This is called the Bohm criterium, where the isothermal sound speed is given by ($T_i = 0$, m = 0),

$$C_s = \left(T_e/M\right)^{1/2}. \tag{B.9}$$

Appendix C

Exponential distribution

In this appendix the exponential distribution will be introduced. The appendix follows Ross closely [75]. The exponential probability density function is defined as,

$$f(x) = \frac{1}{\lambda} \exp\left(-\frac{x}{\lambda}\right), \; x \geq 0. \tag{C.1}$$

Where λ is the mean value of x. In this thesis the complementary cumulative distribution function (CCDF) will be used because it looks smoother on experimental data,

$$\begin{aligned} CCDF = F_X(X > x) = 1 - F_X(X \leq x) = 1 - \int_{-\infty}^{x} f(x)dx \\ = 1 - \left(1 - \exp\left[-\frac{x}{\lambda}\right]\right) = \exp\left(-\frac{x}{\lambda}\right). \end{aligned} \tag{C.2}$$

The moment generating function of an exponential distribution can be written as,

$$\begin{aligned} \phi_x(t) &= E[e^{tx}] \\ &= \int_0^\infty \frac{1}{\lambda} \exp[-(\frac{1}{\lambda} - t)x] \\ &= (1 - \lambda t)^{-1}, \; t < \frac{1}{\lambda}. \end{aligned} \tag{C.3}$$

From the equation above the moments can be calculated by,

$$E(x^n) = \frac{d^n}{dt} \phi_x(0). \tag{C.4}$$

Thus the first four moments in an exponential distribution is,

$$\begin{aligned} E(x) &= \frac{d}{dt}\phi_x(0) = \lambda(1-\lambda t)^{-2}|_0 = \lambda, \\ E(x^2) &= \frac{d^2}{dt^2}\phi_x(0) = 2\lambda^2(1-\lambda t)^{-3}|_0 = 2\lambda^2, \\ E(x^3) &= \frac{d^3}{dt^3}\phi_x(0) = 6\lambda^3(1-\lambda t)^{-4}|_0 = 6\lambda^3, \\ E(x^4) &= \frac{d^4}{dt^4}\phi_x(0) = 24\lambda^4(1-\lambda t)^{-5}|_0 = 24\lambda^4, \end{aligned} \tag{C.5}$$

Thus the moments in an exponential distribution can be written as,

$$E(x^n) = \lambda^n n!\,. \tag{C.6}$$

Now assuming that Z is a sum of n independent exponential variables,

$$Z = \sum_{i=1}^{n} x_i. \tag{C.7}$$

Since the variables are independent, the moment generating function of Z can be written as the product of the moment generating functions,

$$\phi_Z(t) = \prod_{i=1}^{n} \phi_{x_i}(t) = (1-\lambda t)^{-n}\,,\ \frac{1}{\lambda} > t. \tag{C.8}$$

Now it will be shown that this is just the moment generating function of a gamma distributed variable with $\lambda = \theta$ and $n = k$. The gamma probability density function is given by,

$$f(x) = \frac{1}{\theta^k}\frac{1}{\Gamma(k)}x^{k-1}\exp\left(-\frac{x}{\theta}\right), x, k, \theta > 0. \tag{C.9}$$

In a similar way as for the exponential distribution the moment generating function for a gamma distributed variable can be written as,

$$\begin{aligned} \phi_x(t) &= E\left(e^{tx}\right) \\ &= \frac{1}{\theta^k}\frac{1}{\Gamma(k)}\int_0^\infty x^{k-1}\exp[-\left(\frac{1}{\theta}-t\right)x] \\ &= \frac{1}{\theta^k}\frac{1}{\Gamma(k)}\int_0^\infty x^{k-1}\exp(-ax), a = \frac{1}{\theta}-t > 0 \\ &= \frac{1}{\theta^k}\frac{1}{a^k}\underbrace{\int_0^\infty \frac{a^k}{\Gamma(k)}x^{k-1}\exp(-ax)}_{1} \\ &= \frac{1}{\theta^k}\frac{1}{a^k} \\ &= (1-\theta t)^{-k},\ \frac{1}{\theta} > t. \end{aligned} \tag{C.10}$$

The equation above is the same as the moment generating function for the sum, (C.8), with $\theta = \lambda$ and $n = k$. Thus the sum of n independent exponential random variables with mean value λ follow a gamma distribution with parameters λ, n.

Appendix D

Poisson process

In this appendix the Poisson process will be introduced. The appendix follows Ross closely [75]. A Poisson process is a counting process with independent and stationary increments where the number of events in an interval T is Poisson distributed,

$$P(K(T+s)-K(s)=k)=\frac{1}{k!}\left(\frac{T}{\lambda}\right)^k e^{-\frac{T}{\lambda}},\ k,\lambda,T>0. \tag{D.1}$$

The moment generating function can be found by,

$$\begin{aligned}\phi_k(t)=E[e^{tk}]&=\sum_{k=0}^{\infty}e^{tk}\frac{1}{k!}(\frac{T}{\lambda})^k e^{-\frac{T}{\lambda}}\\&=e^{-\frac{T}{\lambda}}\sum_{k=0}^{\infty}\frac{\left(e^t\frac{T}{\lambda}\right)^k}{k!}\\&=e^{-\frac{T}{\lambda}}e^{et\frac{T}{\lambda}}=e^{\frac{T}{\lambda}\left(e^t-1\right)}.\end{aligned} \tag{D.2}$$

The first four moments are then given by,

$$\begin{aligned}E(k)&=\frac{d}{dt}\phi_k(0)\\&=\left(\frac{T}{\lambda}\exp\left[\frac{T}{\lambda}\left(e^t-1\right)\right]e^t\right)_0\\&=\frac{T}{\lambda},\end{aligned} \tag{D.3a}$$

$$\begin{aligned}E(k^2)&=\frac{d^2}{dt^2}\phi_k(0)\\&=\left(\left(\frac{T}{\lambda}\right)^2\exp\left[\frac{T}{\lambda}(e^t-1)\right]e^{2t}+\frac{T}{\lambda}\exp\left[\frac{T}{\lambda}\left(e^t-1\right)\right]e^t\right)_0\\&=\left(\frac{T}{\lambda}\right)^2+\frac{T}{\lambda},\end{aligned} \tag{D.3b}$$

$$\begin{aligned} E(k^3) &= \frac{d^3}{dt^3}\phi_k(0) \\ &= \left(\left(\frac{T}{\lambda}\right)^3 \exp\left[\frac{T}{\lambda}(e^t-1)\right] e^{3t} + 3\left(\frac{T}{\lambda}\right)^2 \exp\left[\frac{T}{\lambda}(e^t-1)\right] e^{2t} \right. \\ &\qquad \left. + \frac{T}{\lambda}\exp\left[\frac{T}{\lambda}\left(e^t-1\right)\right] e^t \right)_0 \\ &= \left(\frac{T}{\lambda}\right)^3 + 3\left(\frac{T}{\lambda}\right)^2 + \frac{T}{\lambda} \end{aligned} \tag{D.3c}$$

$$\begin{aligned} E\left(k^4\right) &= \frac{d^3}{dt^3}\phi_k(0) \\ &= \left(\left(\frac{T}{\lambda}\right)^4 \exp\left[\frac{T}{\lambda}\left(e^t-1\right)\right] e^{4t} + 6\left(\frac{T}{\lambda}\right)^3 \exp\left[\frac{T}{\lambda}\left(e^t-1\right)\right] e^{3t} \right. \\ &\qquad \left. + 7\left(\frac{T}{\lambda}\right)^2 \exp\left[\frac{T}{\lambda}\left(e^t-1\right)\right] e^{2t} + \frac{T}{\lambda}\exp\left[\lambda\left(e^t-1\right)\right] e^t \right)_0 \\ &= \left(\frac{T}{\lambda}\right)^4 + 6\left(\frac{T}{\lambda}\right)^3 + 7\left(\frac{T}{\lambda}\right)^2 + \frac{T}{\lambda}. \end{aligned} \tag{D.3d}$$

The time between to events in a Poisson process can be written as,

$$\begin{aligned} P(T_{k+1} > t | T_k = t_k) &= P(0 \; event \; in \; (t_k, t_k + t) | T_k = t_k) \\ &= P(0 \; events \; in \; (t_k, t_k + t)) \\ &= P(0 \; events \; in \; t) \\ &= P(K = 0). \\ &= \exp(-\frac{t}{\lambda}). \end{aligned} \tag{D.4}$$

In the derivation above it has been used that a Poisson process has independent and stationary increments. In equation D.4 the complementary cumulative distribution function for waiting times is given. By comparing this to the complementary cumulative exponential function in equation C.2 one can see that the waiting times in a Poisson process are exponentially distributed.

Appendix E

Moments for a shot noise process

In this appendix the moments of the shot noise process given in equation (5.1) will be calculated. The waveform, and distributions for amplitude and number of events was defined in equations (5.2, 5.3, 5.5). The calculations done here is similar to Campbell's theorem [66]. The waveform consisting of exactly K events is given by,

$$\Phi_K(t) = \sum_{k=1}^{K} A_k \psi(t - t_k). \tag{E.1}$$

The average of this function can be written as,

$$\begin{aligned} E[\Phi_K(t)] &= \sum_{k=1}^{K} \prod_{i=1}^{K} \int_0^T E[A_k]\psi(t - t_k)\frac{dt_i}{T} \\ &= E[A]\frac{K}{T}\int_{-\infty}^{\infty} \psi(t)dt \\ &= E[A]\frac{K}{T}(\tau_r + \tau_d). \end{aligned} \tag{E.2}$$

To get the mean value for any K the solution has to be averaged over all realizations of K,

$$E[\Phi(t)] = \sum_{K=0}^{\infty} P(K)E[\Phi_K(t)] \quad = E[A]\gamma. \tag{E.3}$$

Where γ is as before,

$$\gamma = \frac{\tau_r + \tau d}{\tau_w}. \tag{E.4}$$

The calculations for the other moments are derived in a similar way,

$$
\begin{aligned}
E[\Phi_K^2(t)] &= \sum_{m=1}^{K}\sum_{k=1}^{K}\prod_{i=1}^{K}\int_0^T E[A_kA_m]\psi(t-t_k)\psi(t-t_m)\frac{dt_i}{T} \\
&= E[A^2]\frac{K}{T}\int_{-\infty}^{\infty}\psi^2(t)dt + E[A]^2\frac{K^2-K}{T^2}\left(\int_{-\infty}^{\infty}\psi(t)dt\right) \\
&= E[A]^2\left(2\frac{K}{T}\frac{\tau_r+\tau_d}{2} - \frac{K^2-K}{T^2}\left(\tau_r+\tau_d\right)^2\right).
\end{aligned}
\tag{E.5a}
$$

$$
\begin{aligned}
E[\Phi^2(t)] &= \sum_{K=0}^{\infty} P(K)E[\Phi_K^2(t)] \\
&= E[A]\left(\gamma+\gamma^2\right).
\end{aligned}
\tag{E.5b}
$$

$$
\begin{aligned}
E[\Phi_K^3(t)] &= \sum_{k=1}^{K}\sum_{m=1}^{K}\sum_{l=1}^{K}E[A_kA_mA_l]\prod_{i=1}^{K}\int_0^T \psi(t-t_k)\psi(t-t_m)\psi(t-t_l)\frac{dt}{T} \\
&= E[A^3]\frac{K}{T}\int_{-\infty}^{\infty}\psi^3(t)dt \\
&\quad + E[A^2]E[A]\frac{3K(K-1)}{T^2}\int_{-\infty}^{\infty}\psi^2(t)dt\int_{-\infty}^{\infty}\psi^2(t')dt' \\
&\quad + E[A]^3\frac{K^3-3K^2+2K}{T^3}\int_{-\infty}^{\infty}\psi^2(t)dt \\
&= E[A]^3\left(6\frac{K}{T}\frac{\tau_r+\tau_d}{3} + \frac{3K(K-1)}{T}(\tau_r+\tau_d)^2\right. \\
&\qquad\qquad\qquad\qquad \left. + \frac{K^3-3K^2+2K}{T^2}(\tau_r+\tau_d)^2\right).
\end{aligned}
\tag{E.5c}
$$

$$
\begin{aligned}
E[\Phi^3(t)] &= \sum_{K=0}^{\infty} P(K)E[\Phi_K^3(t)] \\
&= E[A]^3\left(2\gamma+3\gamma^{@}+\gamma^3\right).
\end{aligned}
\tag{E.5d}
$$

$$
\begin{aligned}
&E[\Phi_K^4(t)] \\
&= \sum_{k,l,m,n}^{K} E[A_kA_lA_mA_n]\prod_{i=1}^{K}\int_0^T \psi(t-t_k)\psi(t-t_m)\psi(t-t_l)\psi(t-t_n) \\
&= E[A]^4\left(\frac{K}{T}\frac{\tau_r+\tau_d}{4} + \frac{3(K^2-K)}{T^2}(\tau_r-\tau_d)^2 + \frac{6(K^3-3K^2+2K)}{T^3}(\tau_r+\tau_d)^3\right. \\
&\qquad \left. + \frac{4(K^2-K)}{T^2}(\tau_r+\tau_d)^2 + \frac{K^4-6K^3+11K^2-6K}{T^4}(\tau_r+\tau_d)^4\right).
\end{aligned}
\tag{E.5e}
$$

$$\begin{aligned} E[\Phi^4(t)] &= \sum_{K=0}^{\infty} P(K) E[\Phi_K^4(t)] \\ &= E[A]^4 \left(6\gamma + 11\gamma^2 + 6\gamma^3 + \gamma^4\right) . \end{aligned} \tag{E.5f}$$

Appendix F

Sattin PDF for blob dominated signal

In this appendix the PDF of blob dominated signals are derived from the current continuity equation, the method is described in detail by Sattin et al [81]. The current continuity equation for plasma in the sheath resistive regime was given in the theory part, equation (3.38),

$$\frac{d}{dt}\nabla_{\perp}^{2}\phi+\frac{2}{BR}\frac{\partial n}{\partial y}=e^{2}n_{0}C_{s}\left[\exp\left(\phi-\phi_{0}\right)/T\right]. \tag{F.1}$$

Assuming zero vorticity the potential can be written as,

$$\frac{e}{T}\phi(n)=\ln\left[1-\frac{\ln\left(\frac{n}{n_0}\right)}{K}\right]. \tag{F.2}$$

In the equation above K and n_0 is defined as,

$$\begin{aligned} K&=\frac{\exp\left(\frac{e}{T}\phi_0\right)}{2}eC_sBR,\\ n_0&=\exp\left\{\frac{eC_sBR\left[\exp\left(-\phi_0\frac{e}{T}\right)-1\right]}{2}\right\}. \end{aligned} \tag{F.3}$$

The PDF of n can be written as a function of the potential ϕ,

$$F(\phi)d\phi=F[\phi(n)]\frac{d\phi(n)}{dn}dn. \tag{F.4}$$

By assuming that the potential is normal distributed with μ, σ the particle density distribution can be written as,

$$F(n) = F[\phi(n)]\frac{d\phi(n)}{dn} = \frac{1}{\sqrt{2\pi\sigma^2}}\exp\left\{-\frac{1}{2}\frac{\left[\ln\left(1-\frac{\left(\frac{n}{n_0}\right)}{K}\right)-\mu\right]^2}{\sigma^2}\right\}\frac{1}{1-\frac{\ln\left(\frac{n}{n_0}\right)}{K}}\frac{1}{\frac{n}{n_0}}. \tag{F.5}$$

Thus a probability distribution for a blob dominated signal can be fitted with the equation above above where the four free parameters n_0, K, μ, and σ can be found by iteration.

Appendix G

Matlab code

In this appendix the most important matlab function used is displayed.

```
function [tops,wtime,peak,pos] = conditional_win_avg(sign,tresh,ndist,maxs)
% This function calculates the conditional average window of a signal. The
% function takes in the signal, sign, the threshold for which bursts are
% defined, tresh, the half length of conditional window, ndist, and the maximum burst
% amplitude allowed, maxs. The function returns all conditional window
% tops, the waiting time, wtime, the amplitude of the peaks, peak, and the
% position of the peaks, pos. The method goes through the signal by finding the
% maximum and putting the area 2*ndist around the peak value and then find
% the next maximum until there are no more maximums above the threshold.
ntops = 0;
stmp = sign;
nntops = 0;
tops = zeros(2.*ndist + 1,1);
pos = zeros(2.*ndist + 1,1);
wtime = 0;
peak = 0;
stmp(1:ndist) = 0;
stmp(end ndist:end) = 0;
while max(stmp) > tresh
    [topp,i] = max(stmp);
    if topp < maxs
        if min(abs(nntops   i(1))) > 2*ndist
            ntops = ntops + 1;
            peak(ntops) = topp(1);
            nntops(ntops) = i(1);
            tops(:,ntops) = sign(i(1)   ndist:i(1) + ndist);
            pos(:,ntops) = i(1)   ndist:i(1) + ndist;
        end
    end
    stmp(i(1)   ndist:i(1) + ndist) = 0;

end

% calculate waiting times
snn = sort(nntops);
```

```
for k = 1:length(snn)   1;
    wtime(k) = snn(k +1)   snn(k);
end




function [start,slutt,Top,Topt] = cond_avg_overlap(sign,thresh)
% This function calculates the amplitude of the local maxima above a
% certain threshold, thresh, of the signal, sign. The method returns the
% peak value, Top, and position, Topt. Start and slutt represents the
% starting times of events above the threshold and slutt the endings.

rsign = (sign   mean(sign))./std(sign);



over = 0;
k = 0;
start = zeros(length(rsign),1);
slutt = zeros(length(rsign),1);
Top = zeros(length(rsign),1);
Topt = zeros(length(rsign),1);
for i = 1:length(rsign)
    if over == 0 && rsign(i) > thresh
        k = k + 1;
        start(k) = i;
        over = 1;
    elseif over == 1 && rsign(i) < thresh
        slutt(k) = i;
        [Top(k), ttemp] = max(rsign(start(k):slutt(k)));
        temp = start(k):slutt(k);
        Topt(k) = temp(ttemp);
        over = 0;
    end
end
start(start == 0) = [];
slutt(slutt == 0) = [];
Top(Top == 0) = [];
Topt(Topt == 0) = [];



function [Vc, Vnorm] = CondVar(tops)
% The function takes in conditional waveforms above threshold and retrunrs
% conditional variance calculated by two methods. Vc is the regular
% conditional variance, while the Vnorm normalizes each conditional
% waveform before calculating the conditional variance.

[m,n] = size(tops);
ny = zeros(m,n);
ny2 = zeros(m,n);
Vc = zeros(m,1);
Vnorm = zeros(m,1);
for j =  1:n
```

```
    ny(:,j) = tops(:,j)   mean(tops,2);
    ny2(:,j) = tops(:,j)./max(tops(:,j))   mean(tops,2)./max(mean(tops,2));
end
    A = mean(ny.^2,2);
    B = mean(tops.^2,2);
    A2 = mean(ny2.^2,2);
    B2 = mean(tops.^2,2)./max(mean(tops.^2,2));
    Vc = A./B;
    Vnorm = A2./B2;


function [RS,n] = rescaled_range(sgnl)

% This function calculates the rescaled range of a signal, sgnl. The
% function calculations the rescaled range for intervals on a power of two
% scale. Each interval length is averaged over all possible intervals of
% the same length in the signal, without overlap. The function returns the
% rescaled range and the length of the intervall ranges.


N = floor(log2(length(sgnl)));
n = 2.^(1:1:N)';
RS = zeros(N,1);

for nn=1:N
    M = 2^N/n(nn);
    RSm = zeros(M,1);
    for mm=1:M
        m1  = (mm 1)*n(nn)+1;
        m2  = mm*n(nn);
        temp = sgnl(m1:m2);
        temp = temp   mean(temp);
        cuml = zeros(n(nn),1);
        cuml(1) = temp(1);
        for kk=2:n(nn)
            cuml(kk) = cuml(kk 1) + temp(kk);
        end
        R = max(cuml)   min(cuml);
        S = std(temp);
        RSm(mm) = R/S;
    end
    Rsm(RSm == Inf) = [];
    RS(nn) = nanmean(RSm);
end


function [S,n] = Structure_functions(sgnl,q)

% This function calculates the q dimensional structure functions of a
% signal sgnl. The function returns the q dimensional structure function S
% and the time scales of caluclation, n.

K1 = length(sgnl);
```

```
temp = sgnl;
cuml = zeros(K1,1);
cuml(1) = temp(1);
for nn=2:N
    cuml(nn) = cuml(nn 1) + temp(nn);
end
N = floor(log2(K1));
n = ceil(2.^(1:0.5:N))';
K = length(n);
S = zeros(K,q);

for qq=1:q
    for kk=1:K
        for nn=1:(N n(kk))
            S(kk,qq) = S(kk,qq) + (abs(cuml(nn+n(kk))  cuml(nn)))^qq;
        end
        S(kk,qq) = S(kk,qq)/(N n(kk));
    end
    S(:,qq) = S(:,qq)/S(1,qq);
end



function [sgnl,time] = Shot_noise_gen(g,l,N)
% This function returns a shot noise signal with intermittency parameter g,
% l is the relation between rise and decay time, and N is the number of
% bursts. The function returns the signal and its time steps.


t = 1:N;
dt = 1e 2;
K = N./(g.*dt);
tend = N/g;
time = dt:dt:tend;
Am = 1;
A = exprnd(Am,N,1);
tevent = rand(N,1)*tend;
tevent = sort(tevent);
kevent = round(tevent./dt);
trevent = kevent.*dt;
twait = zeros(N 1,1);
for nn=1:N 1
    twait(nn) = trevent(nn+1) trevent(nn);
end

sgnl = zeros(K,1);
S = zeros(K,1);
for i = 1:N
    S(1:kevent(i)) = A(i).*exp(( trevent(i) + dt:dt:0)./l);
    a = dt:dt:round((tend trevent(i))./dt).*dt;
    S(kevent(i) + 1:end) = A(i).*exp( (a)./(1 l));
    sgnl = sgnl + S;
end
```

```
function [W,a]=Wavelet(sgnl)
% This function calculates the wavelet coefficients with the use of the
% matlab function cwtft. The function returns the wavelet coefficients at
% time scales, a.

N=length(sgnl);
sig = struct('val',sgnl,'period',1);
cwtstruct=cwtft(sig,'wavelet','mexh');
a=cwtstruct.scales.*10.^6;
Wcfs=cwtstruct.cfs;
W=Wcfs';
```

```
function [Rand_sign] = Data_randomization(sgnl,dn)
% This function randomize the signal sgnl by dividing the signal into boxes
% of length dn, and then put the boxes in a random order, Rand_sign.
K = length(sgnl);
num = K./dn;
pos = dn.*randperm(num)   dn + 1;
temp = ones(K,1);

k = 0;
for i = 1:dn:K   dn + 1
    k = k +1;
    temp(i:i + dn 1 )  = sgnl(pos(k):pos(k) + dn   1);
end
Rand_sign = temp;
```

```
function [pmf,ccdf,x] = Dist_maker(sign,Nbin)
% This function calculates the PMF and the CCDF of a signal by collecting
% the data in a histogram in Nbin number of bins with values, x.

[pmf,x] = hist(sign,Nbin);

pmf = pmf./sum(pmf);

cdf = zeros(1,Nbin);
cdf(1) = pmf(1);
for i=2:Nbin
    cdf(i) = cdf(i 1 ) + pmf(i);
end
ccdf = 1.0   cdf;
```

Bibliography

[1] Agostini, M. et al., *Study of statistical properties of edge turbulence in the National Spherical Torus Experiment with the gas puff imaging diagnostic*, Physics of Plasmas, **14**, 102305, 2007.

[2] Anis, A.A, Lloyd, E.H, *The expected value of the adjusted rescaled Hurst range of independent normal summands*, Biometrika, **63**, 111-116, 1976.

[3] Anis, G.Y, et al., *On the scaling of avaloids and turbulence with the average density approaching the density limit*, Physics of Plasmas, **12**, 082503, 2005.

[4] Antoni, V. et al., *Transport Processes in Reversed-Field-Pinch Plasmas: Inconsistency with the Self-Organized-Criticality Paradigm*, Physical Review Letters, **87**, 045001-(1-4) 2001.

[5] Bak, P., *How nature works: The science of Self-Organized Criticality*, Oxford University Press, 1997.

[6] Bergsaker, A.S., *Anomalous transport in a toroidal plasma*, Master Thesis, UiO, 2012.

[7] Bian, N. et al., *Blobs and front propagation in the scrape-off layer of magnetic confinement devices*, Physics of Plasmas, **10**, 671-676, 2003.

[8] Boedo, J.A. et al., *Transport by intermittency in the boundary of the DIII-D tokamak*, Chapman & Hall/CRC, Physics of Plasmas, **10**, 1670-1678, 2003.

[9] Boedo, J.A., *Edge turbulence and SOL transport in tokamaks*, Journal of Nuclear Materials, **390-391**, 29-37, 2009.

[10] Carbone, V. et al., *Intermittency and self-similarity in plasma edge fluctuations* Physics of Plasmas, **7**, 445-447, 2000.

[11] Carreras, B.A. et al., *Structure and properties of the electrostatic fluctuations in the far scrape-off layer region of Alcator C-Mod* Physics of Plasmas, **8**, 3702-3707, 2001.

[12] Carreras, B.A. et al., *Long-Range Time Correlations in Plasma Edge Turbulence* Physical Review Letters, **80**, 4438-4441, 1998.

[13] Carreras, B.A. et al., *Self-similarity of the plasma edge fluctuations* Physics of Plasmas, **5**, 3632-3642, 1998.

[14] Carreras, B.A. et al., *Experimental evidence of long-range correlations and self-similarity in plasma fluctuations* Physics of Plasmas, **6**, 1885-1892, 1999.

[15] Chen, F.F., *Introduction to Plasma Physics and Controlled Fusion* Spinger, 2nd edition, 2006.

[16] Cziegler, I., *Turbulence and Transport Phenomena in Edge and Scrape-off-Layer Plasmas* PhD thesis, Massachusetts Institute of Technology, 2011.

[17] D'Ippolito, D.A., Myra, J.R., Zweben,S.J., *Convective transport by intermittent blob-filaments: Comparison of theory and experiment* Physics of Plasmas, **18**, 060501, 2011.

[18] D'Ippolito et al., *Blob Transport in the Tokamak Scrape-off-Layer* Contributions to Plasma Physics, **44**, 205-216, 2004.

[19] D'Ippolito et al., *Cross-field blob transport in tokamak scrape-off-layer plasmas* Physics of Plasmas, **9**, 222-233, 2002.

[20] Dstrozzi, Source: *https : //upload.wikimedia.org/wikipedia/commons/d/d0/ Fusion_rxnrate.svg* Reaction rate figure, Wikipedia.

[21] Edwards, C.H, Penney, D.E, *Elementary Differential Equations* Pearson, 6th edition, 2007.

[22] Durrani, S., Matlab code, source: *http : //www.mathworks.com /matlabcentral/fileexchange/*301*kochm*, (dsalman@wol.net.pk).

[23] Farge, M., *Wavelet transforms and their applications to turbulence* Annual Review of Fluid Mechanics, **24**, 395-457, 1992.

[24] Farge, M., Schneider, K. and Devynck, P., *Extraction of coherent bursts from turbulent edge plasma in magnetic fusion devices using orthogonal wavelets* Physics of plasmas, **13**, 042304, 2006.

[25] Freidberg, J., *Plasma physics and fusion energy* Cambridge university press, 1st edition, 2007.

[26] Garcia, O.E. et al., *Turbulence and intermittent transport at the boundary of magnetized plasmas* Physics of plasmas, **12**, 062309, 2005.

[27] Garcia, O.E. et al., *Turbulent transport in the TCV SOL* Journal of Nuclear Materials, **363-365**, 575-580, 2007.

[28] Garcia, O.E., *Stochastic Modeling of Intermittent Scrape-Off Layer Plasma Fluctuations* Physical Review Letters, **108**, 265001, 2012.

[29] Garcia, O.E. et al., *Burst statistics in Alcator C-Mod SOL turbulence* 2012.

[30] Garcia, O.E. et al., *Radial interchange motions of plasma filaments* Physics of plasmas, **13**, 082309, 2006.

[31] Garcia, O.E. et al., *Mechanism and scaling for convection of isolated structures in non uniformly magnetized plasmas* Physics of plasmas **12**, 090701, 2005.

[32] Garcia, O.E., *Blob Transport in the Plasma Edge: a Review* Plasma and Fusion Research: Review Articles, **4**, 019, 2009.

[33] Garcia, O.E., *Collective motions in non-uniformly magnetized plasmas* European Journal of Physics, **24**, 331-339, 2003.

[34] Garcia, O.E., et al., *Intermittent fluctuations in the Alcator C-Mod scrape-off layer* Physics of Plasmas, **20**, 055901, 2013.

[35] Garcia, O.E., et al., *Interchange turbulence in the TCV scrape-off layer* Plasma Physics and Controlled Fusion, **48**, L1-L10, 2006.

[36] Garcia, O.E., et al., *Collisionality dependent transport in TCV SOL plasmas* Plasma Physics and Controlled Fusion, **49**, B47-B57, 2007.

[37] Garcia, O.E., *Plasma Fluid Models* Plasma Notes, UiT.

[38] Gilmore, et al., *Investigation of rescaled range analysis, the Hurst exponent, and long-time correlations in plasma turbulence* Physics of Plasmas, **9**, 1312-1317, 2002.

[39] Graves, J.P et al., *Self-similar density turbulence in the TCV tokamak scrape-off layer* Plasma Physics and Controlled Fusion, **47**, L1-L9, 2005.

[40] Greenwald, M., *Density limits in toroidal plasmas* Plasma Physics and Controlled Fusion, **44**, R27-R80, 2002.

[41] Grossmann, A., Morlet, J., *Decomposition of hardy functions into square integrable wavelets of constant shape* SIAM Journal on Mathematical Analysis, **15**, 723-736, 1984.

[42] Grulke, O. et al., *Radially propagating fluctuation structures in the scrape-off layer on Alcator C-Mod* Physics of Plasmas, **13**, 012306, 2006.

[43] Hazeltine, R.D., Meiss, J.D., *Shear-Alfvén dynamics of toroidally confined plasmas* Physics Reports, **121**, 1-164, 1985.

[44] Iter, Source: $http://iter.rma.ac.be/en/img/MagneticConfinement.jpg$ Picture magnetic confinement.

[45] Joanes, D.n., Gill, C.A., *Comparing measures of sample skewness and kurtosis* The Statistician, **47**, 183-189, 1998.

[46] Kay, S.M., *Modern Spectral Estimation* Prentice Hall, Englewood Cliffs, New Jersey 07632, 1988.

[47] Krasheninnikov, S.I. et al., *Recent theoretical progress in understanding coherent structures in edge and SOL turbulence* Journal of Plasma Physics, **74**, 679-717, 2008.

[48] Krasheninnikov, S.I., *On scrape off layer plasma transport* Physics Letters A, **283**, 368-370, 2001.

[49] Kube, R., *Numerical studies of radial filament motion in toroidally confined plasmas* Master's thesis in physics, University of Tromsø, 2010.

[50] Kube, R., Garcia, O.E. *Velocity scaling for filament motion in scrape-off layer plasmas* Physics of Plasmas, **18**, 102314, 2011.

[51] Kube, R., Garcia, O.E. *Effect of dynamical friction on interchange motion of plasma filaments* Physics of Plasmas, **19**, 042305, 2012.

[52] LaBombard, B. et al., *Particle transport in the scrape-off layer and its relationship to discharge density limit in Alcator C-Mod* Physics of Plasmas, **8**, 2107-2117, 2001.

[53] LaBombard, B. et al., *Transport-driven Scrape-Off-Layer flows and the boundary conditions imposed at the magnetic separatrix in a tokamak plasma* Nuclear fusion, **44**, 1047-1066, 2004.

[54] LaBombard, B. et al., *Scaling of the power exhaus channel in Alcator C-Mod* Physics of Plasmas, **18**, 056104, 2011.

[55] Lipschultz, B. et al., *Investigation of the origin of neutrals in the main chamber of Alcator C-Mod* Plasma Physics and Controlled Fusion, **44**, 733-748, 2002.

[56] Mahdizadeh, N. et al., *Investigation of intermittency in simulated and experimental turbulence data by wavelet analysis* Physics of Plasmas, **11**, 3932-3938, 2004.

[57] Malamud, B.D., Turcotte, D.L., *Self-affine time series: measures of weak and strong persistence* Journal of Statistical Planning and Inference, **80**, 173-196, 1999.

[58] Mandelbrot, B.B., Van Ness, J.W., *Fractional Brownian motions, fractional noises and applications* SIAM Review, **10**, 422-437, 1968.

[59] Mandelbrot, B.B., Wallis, J.R., *Computer Experiments with Fractional Gaussian Noises part 1-3* Water Resources Research, **5**, 228-241, 260-267, 1969.

[60] Maqueda, R.j. et al., *Gas puff imaging of edge turbulence* Review of Scientific Instruments, **74**, 2020-2026, 2003.

[61] Maqueda, R.j. et al., *Intermittency in the scrape-off layer of the National Spherical Torus Experiment during H-mode confinement* Journal of Nuclear Materials, **415**, S459-S462, 2011.

[62] Melzani, M., *Blob statistics in the scrape-off layer of tokamaks* Department of Physics, École Normale Supérieure de Lyon, 2011.

[63] Meyer, O., *Drift wave turbulence and zonal flows* Master thesis, UiT, 2012.

[64] Naulin, V. et al., *Statistical properties of transport in plasma turbulence* Physics Letters A, **321**, 355-365, 2004.

[65] Naulin, V., *Turbulent transport and the plasma edge* Journal of Nuclear Materials, **363-365**, 24-31, 2007.

[66] Pecseli, H.L., *Fluctuations in Physical Systems* Cambridge University Press, Port Chester, NY, USA, 2000.

[67] Pecseli, H.L., *Low frequency waves and turbulence in magnetized plasmas* Lecture notes, UiO 2013.

[68] Percival, D.B., Walden, A.T., *Spectral analysis for Physical Applications* Cambridge University Press, 1993.

[69] Peters, E.E, *Chaos and order in the capital markets* John Wiley & Sons, Inc, 2nd edition, 1996.

[70] Pitts, R.A., Buttery, R.J., Pinches, S.D., *Fusion: the way ahead* Physics World, **19**, 20-26, 2006.

[71] Qian. H., *Fractional Brownian Motion and Fractional Gaussian Noise* Springer-Verlag Berlin Heidelberg, **621**, 22-33, 2003.

[72] Rea, W. et al., *Estimators for Long Range Dependence: An Empirical Study* Electronic Journal of Statistics, **0**, 2009.

[73] Rhodes, T.L., *Experimental evidence for self-organized criticality in tokamak plasma turbulence* Physics Letters A, **253**, 181-186, 1999.

[74] Rodgers, J.L., Nicewander, W.A., *Thirteen ways to look at the correlation coefficient* The American Statistician, **42**, 59-66, 1988.

[75] Ross S.M., *Introduction to probability models* Academic press, 9th edition, 2007.

[76] Rudakov et al., *Far SOL transort and main wall plasma interaction in DIII-D* Nuclear Fusion, **45**, 1589-1599, 2005.

[77] Rypdal, M., Rypdal, K., *Is there long-range memory in solar activity on time scales shorter than the sunspot period?* Journal of Geophysical Research, **117**, A04103, 2012.

[78] Rypdal, M., *Lecture notes stochastic processes with scaling properties* UiT, 2010.

[79] Sànchez, E., et al., *Statistical characterization of fluctuation wave forms in the boundary region of fusion and nonfusion plasma* Physics of Plasmas, **7**, 1408-1416, 2000.

[80] Sànchez, R., Newman, D.E., Carreras, B.A., *Mixed SOC diffusive dynamics as a paradigm for transport in fusion devices* Nuclear Fusion, **41**, 247-256, 2001.

[81] Sattin, F., Baiesi,M., *Self-Organized-Criticality Model Consistent with Statistical Properties of Edge Turbulence in a Fusion Plasma* Physical Review Letters, **96**, 105005, 2006.

[82] Sattin, F., Vianello, N., Valisa, M., *On the probability distribution function of particle density at the edge of fusion devices.* Physics of Plasmas, **11**, 5032-5037, 2004.

[83] Sattin, F. et al., *About the parabolic relation existing between the skewness and the kurtosis in time series of experimental data* Physica Scripta, **79**, 045006, 2009.

[84] Scipioni, A. et al., *Characterization of self-similarity properties of turbulence in magnetized plasmas* Physics of Plasmas, **15**, 112303, 2008.

[85] Smick, N. et al., *Transport and drift-driven plasma flow components in the Alcator C-Mod boundary plasma* Nuclear Fusion, **53**, 023001, 2013.

[86] Stangeby, P.C., *The Plasma Boundary of Magnetic Fusion Devices* IOP Publishing Ltd., 2000.

[87] Stark, H., Woods, J.W., *Probability and Random Processes with Applications to Signal Processing* Prentice Hall, New Jersey, 2002, 3rd edition.

[88] Staszewski, W.J., Worden, K., *Wavelet analysis of time-series: coherent structures, chaos and noise* International Journal of Bifurcation and Chaos, **9**, 455, 1999.

[89] Stoev, S., fftfgn, Source: $http://www.mathworks.com/matlabcentral/fileexchange/5702-fftfgn/content/fftfgn.m$ Matlab code, 2003.

[90] Terry, J.L. et al., *Observations of the turbulence in the scrape-off-layer of Alcator C-Mod and comparisons with simulation* Physics of Plasmas, **10**, 1739-1747, 2003.

[91] Umansky et al., *Comments on particle and energy balance in the edge plasma of Alcator C-Mod* Phys. Plasmas, **5**, 3373-3376, 1998.

[92] Wang, G. et al., *The Hurst exponent and long-time correlation*, Physics of Plasmas, **7**, 1181-1183, 2000.

[93] Wilson, H.R et al., *Ideal magnetohydrodynamics instability of the tokamak high-confinement-mode edge region*, Physics of Plasmas, **6**, 1925-1934, 1999.

[94] Xu, G.S. et al., *Intermittent convective transport carried by propagating electromagnetic filamentary structures in nonuniformly magnetized plasma*, Physics of plasmas, **17**, 022501, 2010.

[95] Yu, C.X. et al., *Structure function analysis of long-range correlations in plasma turbulence*, Physics of plasmas, **10**, 2772-2779, 2003.

[96] Øynes, F.J. et al. *Experimental study of low-frequency electrostatic fluctuations in a magnetized toroidal plasma*, Physical Review E, **57**, 2242-2255, 1998.

[97] Øynes, F.J. et al. *Fluctuations in a Magnetized Toroidal Plasma without Rotational Transform*, Physical Review Letters, **75**, 81-84, 1995.


UNIVERSITY OF TROMSØ